Functionalizing Silk Hydrogels with Nanoparticles and Fibres

Jirada Kaewchuchuen

Institute of Pharmacy and Biomedical Sciences

University of Strathclyde

A thesis submitted in fulfilment of the requirements for the degree of Doctor of Philosophy

November 2023

Declaration of Authenticity and Author's Rights

'This thesis is the result of the author's original research. It has been composed by the author and has not been previously submitted for examination which has led to the award of a degree.'

'The copyright of this thesis belongs to the author under the terms of the United Kingdom Copyright Acts as qualified by University of Strathclyde Regulation 3.50. Due acknowledgement must always be made of the use of any material contained in, or derived from, this thesis.'

Signed: 

(Jirada Kaewchuchuen)

Date: 11 December 2023

ACKNOWLEDGEMENTS

I would like to express my deepest gratitude to those who have contributed to the completion of this doctoral thesis, a journey that has been both challenging and rewarding. First, I am especially grateful to Dr. Luis Bimbo for choosing me to do the Ph.D. with him and supporting me during my first year of Ph.D. I would like to express my gratitude to my advisor, Dr. Philipp Seib, for his unwavering support, guidance, and discipline during my PhD project. Without his assistance and patience, this thesis would not have been possible. His constant encouragement and invaluable insights to pursue an academic career have been a great source of inspiration. Additionally, I would like to sincerely thank Dr. Christine Dufes for her guidance and support throughout the thesis writing process. Their invaluable feedback and encouragement have played a crucial role in shaping the direction of my research.

Apart from my supervisors, I would like to thank Dr. Thomas McGlone, Dr. Elke Prasad, and Dr. Deborah Bowering for providing me with excellent training in advanced machines in CMAC and enormous technical support. Moreover, I would like to thank Dr Paul Edwards and Dr. Maider Olasolo for providing me with the scanning electron microscope training, and Mr. Graeme MacKenzie for training in confocal and epifluorescence microscopy.

It is my pleasure to acknowledge all my former and current colleagues in the Seib lab, Dr. Suttinee Phuagkhaopong, Dr. John Totten, Dr. Gemma Egan, Saphia Matthew, Kimia Witte, Napaporn Roamcharern, Lana Hassan, Simon Tran, and Dr. Erum Hyder who always being a good friend and providing me with valuable motivation and intensive discussions. I also thank my lovely friends in SIPBS; Panida Punnabhum, Panicha Aruvornlop, Dr. Eleanor Jones, Dr. Musa Batsh and my Thai's friends in Glasgow and UK for their friendship, help and encouragement.

I would like to acknowledge the Chulabhorn Royal Academy for their scholarship and financial support, which enabled me to pursue this research. Their investment in my academic journey has been crucial to the successful completion of this thesis. Moreover, I also thank the Thai Royal Embassy for their kind support during my Ph.D.

I am grateful to my mother for her unwavering support and understanding throughout the ups and downs of this doctoral journey. Her love and encouragement have been my anchor and motivation. I also thank my partner who always supported me in every step of my Ph.D. I truly would have not been able to complete this thesis without his support. Lastly, I extend my deepest gratitude to all those unnamed individuals who, in various capacities, have contributed to the realisation of this thesis. This work would not have been possible without these individuals' collective support; for that, I am truly grateful.

SCIENTIFIC CONTRIBUTIONS

Peer-reviewed publications:

(i) Matthew, S. A. L., Egan, G., Witte, K., **Kaewchuchuen, J**., Phuagkhaopong, S., Totten, J. D., & Seib, F. P. (2022). Smart Silk Origami as Eco-sensors for Environmental Pollution. ACS Applied Bio Materials, 5(8), 3658-3666.

My contributions included silk fibroin and silk film preparation, and secondary structure of silk analysis.

(ii) Matthew, S. A. L., Rezwan, R., **Kaewchuchuen, J.,** Perrie, Y., & Seib, F. P. (2022). Mixing and flow-induced nanoprecipitation for morphology control of silk fibroin self-assembly. RSC Advances, 12(12), 7357-7373.

My contributions included silk nanoparticle morphology observation using a scanning electron microscope.

Paper in preparation/review:

(i) **Kaewchuchuen J.,** Roamcharern N., Phuagkhaopong S., Bimbo M. L., Seib F. P. 'Microfiber-functionalised silk hydrogels'. Submitted *(Chapter 4 of this thesis)*

(i) **Kaewchuchuen J.,** Matthew A. L. S., Phuagkhaopong S., Bimbo M. L., Seib F. P. 'Functionalizing Silk Hydrogels with Hetero- and Homotypic Nanoparticles'. (submitted, see Chapter 3)

Conference contributions:

(i) **Kaewchuchuen J.,** Bimbo M. L., Seib F. P. Tissue Engineering Prostate Cancer Cells in 3D using Silica Nanoparticle functionalised Silk Hydrogels. SIPBS Research Day 2021, University of Strathclyde, Glasgow, UK. January 12, 2021. **Poster presentation.**

(ii) **Kaewchuchuen J.,** Matthew A. L. S., Phuagkhaopong S., Bimbo M. L., Seib F. P. Engineering Nanoparticle functionalised Silk Hydrogels for Prostate Cancer Modelling. 13th APS International PharmSci 2022, September 7-9, 2022. **Poster presentation.**

(iii) **Kaewchuchuen J.,** Matthew A. L. S., Phuagkhaopong S., Bimbo M. L., Seib F. P. Nanoparticle functionalized silk hydrogels for cancer cell culture. The 3rd International workshop on Insect Bio-Inspired Technologies, November 17-18, 2022. **Poster presentation.**

COVID STATEMENT

In October 2019, my Ph.D. journey commenced under Dr. Luis Bimbo, exploring silica nanoparticle research for tissue engineering. Dr Philipp Seib was my second supervisor. The initial six months of my PhD were dedicated to coursework, followed by lab immersion in cell culture after three months. However, the pandemic disrupted my journey. The University and the Strathclyde Institute of Pharmacy and Biomedical Sciences (SIPBS) were locked down on Monday 23rd March 2020 until a phased- return in July 2020. On return, various corona virus measures were in place (social distancing, reduced number of people permitted in labs, reduced working hours etc.). I therefore spent most of time conducting literature reviews and writing my 9-month report during my first year of my PhD.

In the summer 2020, Dr. Bimbo took up a new faculty position at the Department of Pharmaceutical Technology, University of Coimbra, Portugal. In July 2020, Dr. Seib became my primary supervisor. His focus on silk research steered my thesis from silica nanoparticles to silk in the second year. Nevertheless, I continued analyzing silica nanoparticles but now also silk nanoparticles; eventually I developed silk hydrogels doped with these nanoparticles.

This pivot meant diving into new literature and potential delays, challenging my pace. Yet, overcoming these obstacles, I regained momentum and found my own pace. Despite the initial setbacks, the journey led to valuable lessons and personal growth.

This statement was written by Jirada Kaewchuchuen and was verified by Dr Philipp Seib.

13th December 2023

ABSTRACT

This research explores the development of composite silk hydrogels by incorporating different types of silk nanoparticles and microfibres, including *Antheraea mylitta* (Tasar) silk. The aim was to generate hydrogel composites to ultimately modulate the mechanical properties of *Bombyx mori* (*B. mori*) silk hydrogels and enhance cell attachment. *B. mori* silk lacks the arginine-glycine-aspartic acid (RGD) sequence that is used for cell adhesion. Therefore, introducing RGD-containing Tasar silk within *B. mori* hydrogels is particularly interesting. This thesis investigated the mechanical properties of silk hydrogels containing various nanoparticles including silica nanoparticles (Chapter 2 and Chapter 3), *B. mori* and Tasar silk nanoparticles (Chapter 3) as well as silk microfibres . These hydrogel composites were subjected to cell adhesion studies, using DU-145 cells and induced pluripotent stem cell-derived MSCs (iPSCs-MSCs). The research found that silk hydrogels loaded with 5% w/v silica nanoparticles exhibited higher stiffness than those with lower concentrations (Chapter 2). In Chapter 3, the results showed that silk hydrogels functionalised with nanoparticles had similar stiffness but with variations in stress relaxation while maintaining consistent cell attachment. Silk hydrogels reinforced with *B. m*ori and Tasar silk fibres enhanced short-term cell proliferation and attachment, with Tasar silk microfibres being particularly effective. However, cell attachment on silk hydrogels was still less than on tissue culture plastic. Overall, this thesis generated composite silk hydrogels using a spectrum of nanoparticles and silk fibres that in turn modulated the mechanical properties and especially those hydrogels reinforced with silk microfibres, promote short-term cell growth and adhesion.

TABLE OF CONTENTS

TABLE OF CONTENTS (cont.)

LIST OF FIGURES

LIST OF FIGURES (cont.)

LIST OF FIGURES (cont.)

LIST OF TABLES

LIST OF ABBREVIATIONS

B. mori	*Bombyx mori*
RGD	Arginine-glycine-aspartic acid sequences
iPSC	Induced pluripotent stem cell
MSCs	mesenchymal stem cells
A. mylitta	*Antheraea mylitta*
kDa	Kilo Dalton
β-sheets	Beta-sheets
3D	Three-dimensional
w/v	Weight per volume
DMSO	Dimethyl sulfoxide
VEGF	Vascular endothelial growth factor
ADT	Androgen deprivation therapy
CRPC	Castration-resistant prostate cancer
DLS	Dynamic light scattering
FTIR	Fourier-transform infrared spectroscopy
SEM	Scanning electron microscopy
MTT	3-(4,5-dimetylthiazol-2-yl)-2,5-diphenyl-2H-tetrazolium bromide assay
ECM	Extracellular matrix
NH_4OH	Ammonium hydroxide
TEOS	Tetraethyl orthosilicate
CTAC	Cetyltrimethylammonium chloride
TEA	Triethanolamine
NH_4NO_3	Ammonium nitrate
CTAB	Cetyltrimethylammonium bromide
BET	Brunauer–Emmett–Teller
BJH	Barrett-Joyner-Halenda
LiBr	Lithium bromide
PBS	Phosphate buffered saline

LIST OF ABBREVIATIONS (cont.)

RPMI	Roswell park memorial institute 1640 medium
EDTA	Ethylenediamine tetraacetic acid
CO_2	Carbon dioxide
PDI	Polydispersity
Na_2CO_3	Sodium carbonate
NaOH	Sodium hydroxide
PEG	Polyethylene glycol
DI water	Deionised water
HCl	Hydrochloric acid
NaN_3	Sodium azide
NaCl	Sodium chloride
DMEM	Dulbecco's Modified Eagle Medium

Chapter 1

Introduction

Chapter summary:

This chapter provides a general introduction to silk, including its structure and properties. This chapter also describes hydrogels, and their application especially, in tissue engineering. The impact of biomaterials including nanoparticles and microfibres on mechanical properties and cell adhesion are detailed too. This chapter also describes the general methodology used by others and used in this thesis to generate silk hydrogels, nanoparticles, and microfibres. The overall hypothesis of the thesis is introduced, along with accompanying aims and objectives.

Synopsis

Tissue engineering is a multidisciplinary field dedicated to restoring functional human tissues (Lee et al., 2014, Hubbell, 1995). While the human body possesses some inherent self-healing capabilities, the success of tissue repair varies depending on the type of tissue and the disease or severity of injury (Lanza et al., 2020). A traditional approach in tissue engineering involves using a combination of biomaterials, cells, and biological substances to orchestrate tissue generation and integration in the host environment (Lee et al., 2014, Hubbell, 1995). An important aspect of tissue engineering is the development of biomaterials that can enhance regenerative processes by efficiently transporting cells and therapeutic substances (Lee et al., 2014, Hubbell, 1995). These biomaterials also serve as structural support, providing the necessary mechanical properties for tissues. Ideally, these biomaterials should degrade at a rate that aligns with the growth of new tissue (Lee et al., 2014, Hubbell, 1995).

Silk fibroin has emerged as an interesting material to address these limitations. Silk offers the potential for customised materials with bespoke properties through physical and chemical modification (Holland et al., 2019, Lujerdean et

al., 2022). Silk has been adapted to create biomaterials for tissue engineering, including hydrogels (Holland et al., 2019, Lujerdean et al., 2022). These silk-based biomaterials possess a combination of desirable traits, including biocompatibility, biodegradability, mechanical flexibility, and ease of processing, making them attractive for designing hydrogels to support tissue regeneration (Holland et al., 2019, Lujerdean et al., 2022).

Silk hydrogels are typically biocompatible and well-tolerated by living tissues, with the added advantage of a very low immune response (Holland et al., 2019, Lujerdean et al., 2022, Lyu et al., 2023). These characteristics makes silk suitable for both implantation and interaction with cells. Furthermore, the mechanical properties of silk hydrogel can be tailored to suit the requirements of various tissues. Despite extensive research on silk hydrogels, there is still a limited exploration of composite silk hydrogels containing different silk nanoparticles and their effects on material mechanics and the biology (Holland et al., 2019, Lujerdean et al., 2022, Lyu et al., 2023). Working with *B. mori* silk hydrogels is challenging due to the absence of arginine-glycine-aspartic acid (RGD) sequences necessary for integrin-mediated cell adhesion. Hence, silks derived from non-mulberry *A. mylitta* (Tasar) silkworms, which contain the RGD sequence, hold promise (Holland et al., 2019, Mandal and Kundu, 2008). Therefore, the research aim was to create hydrogels functionalised with *B. mori* and Tasar silks to investigate cell responses and compare them to hydrogels prepared using silica nanoparticles as a reference.

Chapter 2 details the synthesis and characterisation of silica nanoparticles. Porous and non-porous silica particles were synthesised using different techniques. This chapter also details the production of physically cross-linked 3% w/v silk hydrogels and creating silk hydrogel particle composites by embedding low (0.1% w/v) and high (5% w/v) concentration of porous and non-porous nanoparticles within silk hydrogels. The impact of silica nanoparticles on the mechanical properties of silk hydrogels was determined.

Chapter 3 covers the manufacture of nonporous Stober silica, *B. mori* and Tasar silk nanoparticles, and their addition at low (0.05% w/v) and high (0.5% w/v) concentrations to *B. mori* silk undergoing solution-gel transition. The impact of nanoparticles on silk hydrogel mechanics was assessed using rheology. *In vitro* studies involved two dimensional DU-145 cell culture on the silk hydrogel composits, measuring cell viability, and attachment.

The final chapter (Chapter 4) investigated the influence of silk microfibres on silk hydrogel mechanics and cell attachment. *B. mori* and Tasar silk microfibres were synthesised and added to silk hydrogel at varying concentrations (2% and 10% w/v). Induced pluripotent stem cells derived from mesenchymal stem cells (iPSC-MSCs) are cultured on these hydrogels, and cell viability, attachment and actin filament were assessed.

In summary, this thesis explores the potential of silk-based biomaterials, specifically silk hydrogel, for ultimate tissue engineering applications. The thesis addresses the limitations of existing biomaterials and investigates the impact of silk nanoparticles and microfibres on material mechanics and cell behaviour.

Background to thesis

1.1 Silk

1.1.1 Composition and structure of silk

Silk is a renowned textile celebrated for its notable attributes, encompassing robust tensile strength, remarkable elasticity, lustrous sheen, and enduring longevity. Silk exhibits pliability and possesses a moisture capacity regain (Bandyopadhyay et al., 2019). Silk is classified into two types including mulberry and non-mulberry (Figure 1.1 and Table 1.1). Out of these, four types are commercially exploited*: Bombyx mori* (mulberry), Tasar (non-mulberry), Eri (non-mulberry), and Muga (non-mulberry)(Bandyopadhyay et al., 2019). Silk is made up of a spectrum of amino acids and has an

amphoteric nature (Bandyopadhyay et al., 2019). The silk protein is normally synthesised within specialised epithelial cells, then secreted into the lumen of the silk gland, where the silk protein is stored until being spun into a fibre (Zhang et al., 2009). The properties, structure, and composition of silk vary based on their specific function and source.

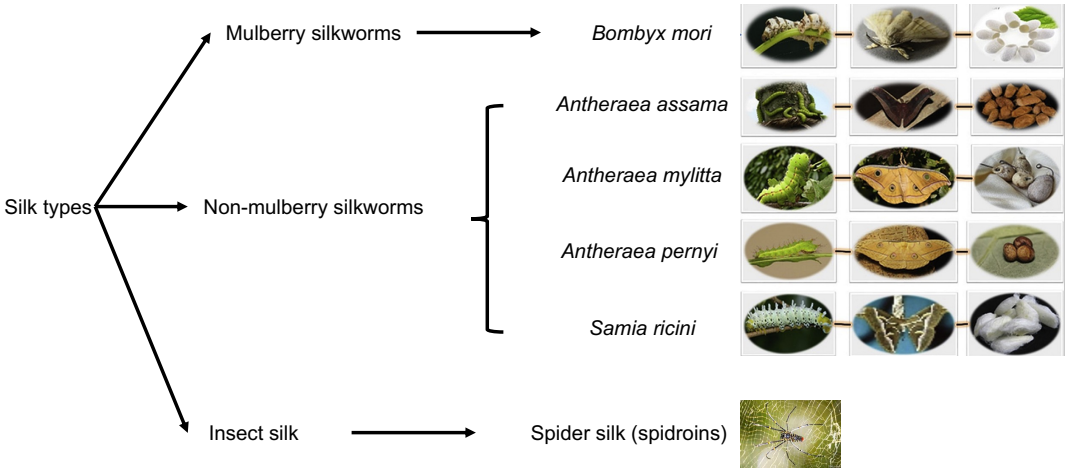

Figure 1.1 Schematic representation of silk types including mulberry, non-mulberry, and insect. Figure adapted from (Fazal and Latief, 2018)

Table 1.1 Type of silk including mulberry, non-mulberry, and insect, characteristics of silk and food plant.

Type of silk	**Characteristics of silk**	**Food plant**
1. Mulberry silkworms		
Bombyx mori	-The cocoons are typically white or off-white and have a consistent, oval, or peanut shape. - Silk is made up of two major proteins namely silk fibroin and sericin, which account for ~75%	Leaves of mulberry (Morus alba)

	and ~25% of the cocoon weight, respectively.	
2. Non-mulberry silkworms		
Antheraea assama	-Cocoons are a bright brown colour and possess a unique natural shine -The biophysical properties of Muga silk include golden luster, tenacity, and high absorbance of ultraviolet radiation.	Terminalia arjuna, Machilus bomycina, Ricinus communis, Euphorbia pulcherrima
Antheraea mylitta	-Cocoons are usually larger and more irregularly shaped. -Fibres have a coarser texture and a natural tan or brown colour.	Terminalia tomentosa, T. arjuna and Shorea robusta
Antheraea pernyi	-Cocoons are natural golden or beige color. It has a moderate sheen and luster. - Silk fibres exhibit high toughness originating from their α-helix/random coil conformation structures and their micro-fibre morphology.	Quercus, Carpinus, and Betula
Samia ricini	-Cocoons are generally small and have a yellowish or reddish-brown colour. -Cocoon is composed of multiple layers (5-6 layers) with an eclosion hole located at one end.	Castor (Ricinus communis), Tapioca (Manihot esculenta), Barara (Jatropha curcas), and

	- Cocoon contains various air gaps between the layers.	Papaya (Carica papaya)
3. Insect		
Spider	- Spiders synthesize spidroins, a class of proteins ranging from 250 to 350 kDA, that create silk with exceptional toughness due to their unique combination of robustness and elasticity. -Spidroins are made up of a core that repeats and contains large amounts of alanine, glycine, and proline residues. This core is surrounded by two distinct terminal regions - the amino (N) and carboxy (C) termini.	Floral nectar, extrafloral nectar, stigmatic exudate, plant sap, honeydew, seeds

Non-mulberry silk cocoons are produced by a variety of silkworm species that feed on different types of leaves, including *Antheraea mylitta* (Tropical Tasar), *Antheraea assama* (Muga), and *Samia/Philosamia ricini* (Eri) (Silva et al., 2016) (Figure 1.1 and Table 1.1). Tasar silk is produced by various species of wild silk moths, including *Antheraea mylitta* and *Antheraea pernyi* (Singh et al., 2021) (Figure 1.1 and Table 1.1). Tasar silk cocoons are usually larger and more irregularly shaped than those of mulberry silk. The fibres of tasar silk cocoons have a coarser texture and a natural tan or brown colour (Anand et al., 2021). The homodimer silk fibroin, with an approximate molecular weight of 395 kDa has been elucidated in the context of tasar silk varieties (Kundu et al., 2012). Examples were *A. mylitta* silk has been used for biomedical applications including corneal films (Hazra et al., 2016) or two-dimensional matrices. For these studies *A. assama* and *A. mylitta* liquid silks were extracted

directly form the silk gland and were mixed with cocoon silk fibroin from *B. mori* (Kar et al., 2013).

Samia Cynthia (Eri) silk is produced by the Eri silkworm, which is native to India and other parts of Asia (Zhou and Wang, 2020). Eri silk cocoons are generally small and have a yellowish or reddish-brown colour (Prabhakar, 2014, Zhou and Wang, 2020). Eri silk cocoon is composed of multiple layers (5-6 layers) with an eclosion hole located at one end (Zhou and Wang, 2020). In addition, the Eri silk cocoon contains various air gaps between the layers. These air gaps play a crucial role in the multi-stage moisture transmission process, resulting in the provision of a moisture buffer effect (Zhou and Wang, 2020).

Eri silk fibroin has been used as a biomaterial including supporting cartilage (Silva et al., 2016) and osteoblast-like cells (Pal et al., 2013). Nonetheless, the underexplored potential of utilizing Eri cocoons, and other non-mulberry silks, as a fibroin source is primarily attributed to the absence of established solubilisation methods involving conventional solvents (Silva et al., 2016). Muga silk cocoons are a bright brown colour and possess a unique natural shine (Freddi et al., 1994). The biophysical properties of Muga silk include golden luster, tenacity, and high absorbance of ultraviolet radiation (Saxena and Goswami, 2010, Kar et al., 2013). Muga silk cocoons have been used in various formats for biomedical applications. For example, Muga silk films were produced by isolating the liquid silk directly from the silk gland. Three Muga silk films were used for supporting MG-63 human osteoblast-like cells (Kar et al., 2013). Muga silk mats have been reported to serving as a biomatrix for the immobilisation of cholesterol oxidase (Saxena and Goswami, 2010). Muga silk fibroin is typically isolated directly in its liquid state from the silk gland due to missing methodologies for re-dissolving spun silk from Muga silk cocoons (Kar et al., 2013).

Besides insect silks (fibroins), spider silk is an important material within the biomaterial community (Figure 1.1 and Table 1.1). Spider silk (spidroins) is a

unique material with outstanding strength and elasticity (Chung et al., 2012, Bittencourt et al., 2022). Spider silks have gained recognition as promising candidates for various biomedical and biotechnological applications, owing to their unique ability to perform specific biochemical, mechanical, and structural functions (Chung et al., 2012, Bittencourt et al., 2022). Spiders synthesize spidroins, a class of proteins ranging from 250 to 350 kDA, that create silk with exceptional toughness due to their unique combination of robustness and elasticity (Chung et al., 2012, Bittencourt et al., 2022, Gu et al., 2020). These spidroins are made up of a core that repeats and contains large amounts of alanine, glycine, and proline residues. This core is surrounded by two distinct terminal regions - the amino (N) and carboxy (C) termini. These two domains are highly conserved throughout evolution and also do not contain any repetitive sequences (Bittencourt et al., 2022, Gu et al., 2020). Spiders produce distinct silk varieties from specialized abdominal glands, each tailored for specific roles throughout its lifecycle (Bittencourt et al., 2022). Unlike silkworms that can be easily farmed (i.e. sericulture), spiders are territorial and cannibalistic prohibiting their farming and large-scale silk production. Instead, heterologous expression systems typically using *E. coli* are used to generate spider-silk inspired proteins (i.e. “mini-spidroins”). These mini-spidroins have been used for biomedical applications including stem cell therapies (Zhang et al., 2021c), extracellular matrix mimetics (Lynch et al., 2021), or drug delivery systems (Numata and Kaplan, 2010).

Mulberry silk is the most well-known and widely used type of silk. The cocoons of the domesticated silkworm *B. mori* are typically white or off-white and have a consistent, oval or peanut shape (Babu, 2019). *B. mori* silk cocoons are popular in scientific research due to their biocompatibility, biodegradability (Holland et al., 2019), unique material properties (Rockwood et al., 2011), genetic modifiability (Teramoto et al., 2018), sustainability (Hăbeanu et al., 2023), and versatility (Wang et al., 2021).

1.1.2 *Bombyx mori* silk cocoons

Bombyx mori (*B. mori*) silk is made up of two major proteins namely silk fibroin and sericin, which account for ~75% and ~25% of the cocoon weight, respectively. The virgin silk fibre also consists of 1.5 % fat and wax and 0.5% mineral salts. (Kunz et al., 2016). Sericin is a glue-like hydrophilic globular protein that surrounds the silk fibroin fibre. Sericin has antibacterial activity and can absorb and remove water. However, sericin is typically removed through a degumming process because sericin in combination with silk is known to induce an inflammatory response. After degumming the water-soluble sericin is removed resulting in a pure silk fibroin (Barajas- Gamboa et al., 2016). Silk fibroin consists of a heavy chain of approximately 350 kDa and a light chain of approximately 25 kDa, which is linked by a disulphide bond (Figure 1.1A). The silk fibroin also contains the P25 glycoprotein with a molecular mass of 27 kDa. The hydrophobic domains of the silk fibroin heavy chains contain Gly-X which X can be alanine, serine, threonine, and valine repeat and can form antiparallel β-sheets (Nguyen et al., 2019). The light chain is hydrophilic and unstructured while the P25 protein is believed to play a significant role in maintaining the integrity of the assembled silk complex (Nguyen et al., 2019). The silk fibroin heavy chain folds into a beta-sheet, providing stability for silk and tensile strength via hydrogen bonds between adjacent sheets (Holland et al., 2019, Tomeh et al., 2019). The repeated alignment of these sheets along the length of the silk fibre enhances its durability. The silk heavy chain has a block-copolymer arrangement with alternating 11 amorphous and 12 crystalline regions (Figure 1.1B) (Tomeh et al., 2019). The crystalline areas, which are primarily composed of beta-pleated sheets, provide the silk fibre strength, while the amorphous regions contribute to its flexibility and softness (Figure 1.1B) (Tomeh et al., 2019). Silk consists of two arrangements: silk I (soluble, amorphous) and silk II (insoluble, crystalline). Most of the silk I structure is composed of random coils and α-helix, while β-sheets make up most of the silk II structure. The silk II structure can be induced by low pH, high temperature and antisolvents. Importantly, the silk II structure contributes to the mechanical properties of silk (Tomeh et al., 2019).

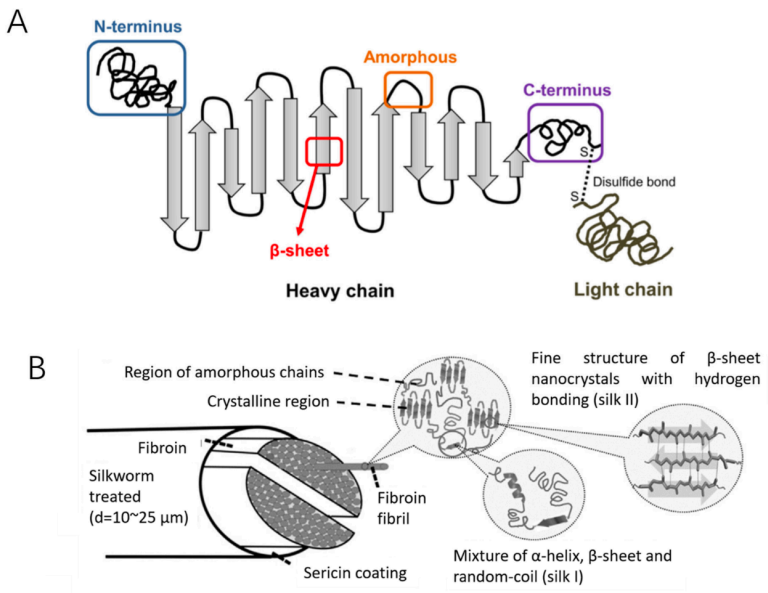

Figure 1.2 Schematic representation of silk structure. (A) The heavy chain composition includes an N-terminus, β-sheets, Amorphous and C-terminus) and a light chain linked via disulphide bonds. (B) Silkworm thread, fibril structure and silk fibroin polypeptide chains. A – B adapted from (Tomeh et al., 2019).

1.1.3 *Antheraea Mylitta* (Tasar) silk cocoons

Silk cocoons produced by *Antheraea mylitta* consist mainly of silk proteins, similar to other types of lepidoptera silk. However, the unique composition of fibroins can differ, resulting in varying properties of Tasar silk in comparison to *B. mori* silk (Darshan et al., 2017). Fibroin is the primary structural protein in *A. mylitta* silk, responsible for providing strength and durability to the fibre (Darshan et al., 2017). The amino acid composition and protein structure of Tasar Silk fibroin differ from that of *B. mori*. When compared to the amino acid composition of *B. mori* silk fibroin, *A. mylitta* silk fibroin contains a higher amount of alanine residues (Darshan et al., 2017, Holland et al., 2019). Furthermore, *A. mylitta* silk contains aspartic and arginine amino acids, and 7 Arg-Gly-Asp (RGD) sequences of per silk fibroin molecule (Figure 1.2 A and B) (Darshan et al., 2017, Holland et al., 2019, Datta et al., 2001). This specific sequence is known to facilitate cell attachment (Darshan et al., 2017, Holland

et al., 2019). Therefore *A. mylitta* is an interesting biomaterial for tissue engineering (Darshan et al., 2017). *A. mylitta* silk also has key hallmarks that are important for tissue engineering including minimal immune response (Acharya et al., 2008b, Sen et al., 2021), good adherence of L929 murine fibroblast adhesion (Acharya et al., 2008b), and growth of cells on or in silk matrices (Acharya et al., 2008b). Therefore, Tasar silk is an interesting biopolymer for tissue engineering.

Antheraea mylitta Fibroin – Start:

```
        10         20         30         40         50         60
MRVIAFVILCCALQYATAKNIHHDEYVDSHGQLVERFTTRKHYERNAATRPHLSGNERLV

        70         80         90        100        110        120
ETIVLEEDPYGHEDIYEEDVVIKRVPGASSSAAAASSASAGSGQTITVERQASHGAGGAA

       130        140        150        160        170        180
GAAAGAAASSSVRGGGGFYETHDSYSSYGSDSAAAAAAAAASGAGGRGHGGYGSDSAAAA

       190        200        210        220        230        240
AAAAAAAAAAASGAGGRGHGGYGSDSAAAAAAAAAAAAAAGSGAGGRGDGGYGWGDGGYG

       250        260        270        280        290        300
SDSGAAAAAAAAAAAAASGAGGRGDGGYGRGDGGYGSDSAAAAAAAAAAAAGSGAGGQAT

       310        320        330        340        350        360
VVMDGAMAAMVLTRAQQQLAAAAAAASASGAGGSGGSYEWDYGSYGSDSAAAAAAAAAA

       370        380        390        400        410        420
AAGSGAGGVGGGYGRGDGGYGSDSAAAAAAAAAAAAGSGAGGRGDGGYGWGDGGYGSDSG

       430        440        450        460        470        480
AAAAAAAAAAAAASGAGGRGDGGYGWGDGGYGSDPGAAAAAAAAAAAAASGARGRGDGGY

       490        500
GSGSSAAAAAAAAAAASAARRAGHDRA
```

Antheraea mylitta Fibroin – END

Figure 1.3 Partial amino acid sequence of *Antheraea mylitta* silk fibroin (Datta et al., 2001).

1.1.4 Research related to RGD (Arginine-Glycine-Aspartic Acid) binding proteins.

Tissue engineering aims to create biocompatible 3D tissue structures for tissue replacement. Peptide self-assembly emerges as an effective strategy in constructing tissue structures and surface functionalities, with the arginine-glycine-aspartic acid (RGD) family of peptides serving as a prominent ligand for extracellular integrin receptors (Kumar et al., 2023). The structural and sequential attributes of RGD peptides significantly impact their efficacy (Kumar et al., 2023). Notably, the immobilization of RGD peptides into macro-porous alginate scaffolds promotes cardiac tissue engineering, facilitating the

formation of functional cardiac muscle tissue (Sondermeijer et al., 2017, Shachar et al., 2011). In cardiac tissue engineering, RGD peptides contribute to a biocompatible environment that enhances cell adhesion, organization, and the development of functional cardiac muscle tissue (Sondermeijer et al., 2017, Shachar et al., 2011). Furthermore, RGD-GO films exhibit the potential for modulating tissue growth and morphology, particularly in engineering and regenerating skeletal tissues (Li et al., 2016).

Additionally, RGD peptide-modified nano-drug delivery systems show promise in tumor therapy by augmenting the targeting capability of nanocarriers for drug delivery (Yin et al., 2023). These peptides and their derivatives serve as ligands for integrin receptors, enhancing the direct targeting ability of nanocarriers and improving the therapeutic effect of antitumor drugs (Yin et al., 2023). The interaction between RGD peptides and integrin avb3 proves crucial in inhibiting tumor cell regeneration and migration, inducing apoptosis, and impeding tumor angiogenesis (Danhier et al., 2012). While these systems exhibit the potential to minimize side effects and enhance antitumor efficiency (Yin et al., 2023).

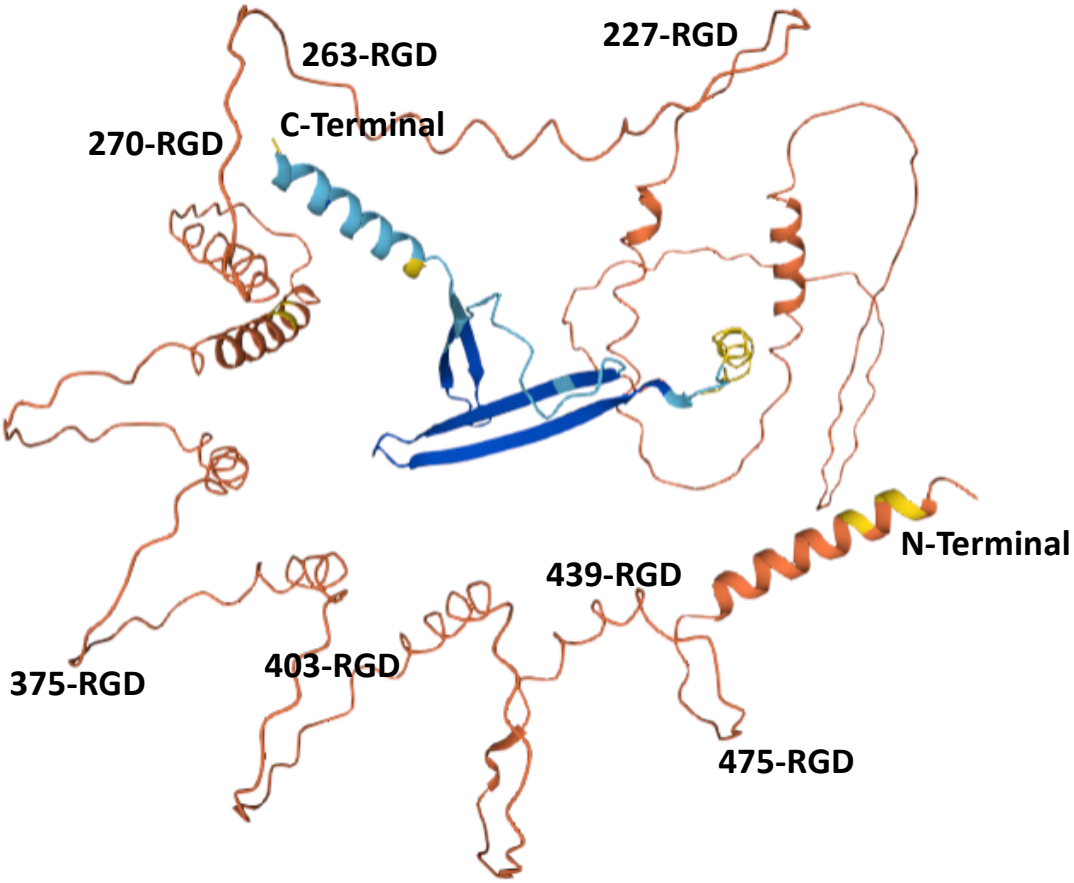

Figure 1.4 *Antheraea mylitta* fibroin protein sequence structure (Datta et al., 2001).

1.1.5 Properties of silk

1.1.5.1 Biocompatibility

Fibroin has been used in medicine for centuries, mainly as a suture material (Holland et al., 2019). Silk sutures are used to this day, especially for specialist wound closure where excellent fibre handling is critical (e.g. eye surgery). Studies have demonstrated their high biocompatibility and immunological compatibility when compared to other natural and synthetic suture materials (Holland et al., 2019, Guidetti et al., 2022). Previous studies comparing the effectiveness of different biomaterials used in medical applications have consistently demonstrated that *B. mori* silk fibroin is at least as effective, and

often more effective, than other synthetic materials and natural biopolymers like collagen (Thurber et al., 2015). Demonstrating initial biocompatibility is the critical first step in transitioning silk-based technologies from laboratory research to practical clinical use (Holland et al., 2019).

B. mori silk fibroin is non-toxic (Tang et al., 2009), typically non-immunogenic (Santin et al., 1999), and biodegradable (Sakabe et al., 1989), with minimal adverse effects from degradation products (Yang et al., 2007). Silk has the potential to trigger type 1 allergic response (Madden et al., 2020, Guidetti et al., 2022). These reactions have been attributed to sericin contamination (i.e. incomplete sericin removal). However, there are very few reported cases of allergic reactions towards silk fibroin per se, suggesting that the material has a low allergenic potential (Makatsori et al., 2014, Guidetti et al., 2022). Silk fibroin is also used to create hypoallergenic clothing that can help alleviate symptoms associated with conditions such as atopic dermatitis (Makatsori et al., 2014). In clinical trials, silk has been explored as a surgical suture application, using degummed *B. mori* silk fibres processed into knitted surgical meshes or rope (Holland et al., 2019). Many studies report the use of silk in pre-clinical studies.

In the field of biomedical research, fibroin has been extensively studied and is well-tolerated in various formats, implantation sites, and timeframes (Holland et al., 2019, Guidetti et al., 2022, Numata and Kaplan, 2010). For example, silk-based electrospun artificial blood vessels were implanted under the skin of rats, causing a mild inflammatory response and no substantial immune reaction (Catto et al., 2015). In addition, fibroin hydrogels are well-tolerated in the brain (Fernández-García et al., 2016, Phuagkhaopong et al., 2021, Gorenkova et al., 2019). Successful long-term tests of fibroin demonstrate its potential for various biomedical applications.

1.1.5.2 Biodegradability

Various factors affect the rate and extent of degradation of natural polymers (Cao and Wang, 2009). These elements encompass the structural and morphological features of the polymers, their formats (e.g. fibres, films, sponges etc.), along with their processing conditions (Cao and Wang, 2009, Umuhoza et al., 2020, Arai et al., 2004). Furthermore, the specific biological milieu at the implantation site and diverse mechanical and chemical stresses also contributes and influence biomaterial degradation (Cao and Wang, 2009, Lau et al., 2017). During biodegradation, various additional influential factors come into play, including protease enzymes (Sun et al., 2021, Umuhoza et al., 2020) and exposure to gamma radiation (Machnowski et al., 2013). These factors collectively exert a significant impact on the behaviour of silk during the biodegradation process, further underscoring the multifaceted nature of its interaction with biological systems.

B. mori silk, being naturally biodegradable, presents significant advantages (Holland et al., 2019). For example, silk offers a promising avenue for the development of biodegradable materials for medical devices and packaging, contributing to the reduction of environmental waste (Holland et al., 2019, Cao and Wang, 2009). Silk fibroins obtained from *B. mori* silk cocoons are promising because of their important characteristics, such as tensile strength, adjustable biodegradability, hemostatic properties, lack of cytotoxicity, low antigenicity and low inflammatory effects (Holland et al., 2019). These qualities render silk materials appealing for biomedical applications (Holland et al., 2019, Cao and Wang, 2009). Silk fibroins are enzymatically degradable that are broken down by proteolytic enzymes (Cao and Wang, 2009, Pişkin, 1995). The degradation kinetics of biomaterials are crucial in their use for medical purposes, particularly *in vivo* (Cao and Wang, 2009). The degradation rate regulation is critical for functional tissue design, ensuring scaffold degradation aligns with tissue growth (Cao and Wang, 2009, Bitar and Zakhem, 2014).

1.1.6 Silk format and applications

Silk textiles are used clinically to treat dermatological conditions especially atopic dermatitis (Fontanini et al., 2013) (Ricci et al., 2004). The silk minimised mechanical irritation and modified surface chemistry creates antibacterial properties ultimately reducing *Staphylococcus aureus* colonisation of the skin (Inoue et al., 1997). However, other material formats have been explored ranging from nanoparticles to 3D porous silk scaffolds (e.g. bone replacement, tissue regeneration (Jiang et al., 2009)). In this thesis the focus were silk hydrogels. An emerging research avenue is to use silk hydrogels to mimic the tumour microenvironment *in vitro*. For example, a previous study evaluated silk fibroin and chitosan scaffolds to stimulate the microenvironment of human tumours in 3D using human non-small lung cancer A549 cells. A549 cells were embedded within the silk fibroin and chitosan scaffolds and showed a great capacity for tumour sphere formation. This in turn recapitulated biological and morphological characteristics of *in vivo* tumours (Li et al., 2018).

B. mori silk fibroin can also be processed into a liquid form and used for 3D printing of scaffolds (Wang et al., 2017). These scaffolds can serve as frameworks for tissue regeneration, guiding the growth of cells and promoting healing in damaged tissues (Wang et al., 2017). Silk fibroin from *B. mori* silk can also act as a barrier or coating in various medical devices such as wound dressings (Patil et al., 2020), and biosensors (Huang et al., 2018). Additionally, silk fibroin can be processed into nanoparticles or microspheres to serve as a vehicle for drug delivery (Seib, 2018, Huang et al., 2017, Wongpinyochit et al., 2016, Zhao et al., 2015). These nanoparticles can encapsulate therapeutic agents and release them at a controlled pace, enhancing drug efficacy and minimizing side effects.

One of the major challenges in tissue engineering and regenerative medicine is the diffusion phenomenon. Essentially, non-vascularised tissues have a limited range for essential elements such as oxygen, nutrients, and metabolic by-products to diffuse, beyond which cellular viability is compromised.

Previous research has shown that silk fibroin is a promising material for creating vascular grafts in preclinical animal models (Kiritani et al., 2020, Enomoto et al., 2010, Tanaka et al., 2018). Due to the high biocompatibility and biodegradability properties of silk, silk has also showen potential to serve as nerve guides (Fornasari et al., 2020, Yan et al., 2022). For example, silk-in-silk nerve conduit made from silk fibroin and spider dragline silk showed comparable regenerative performance to autografts in treating peripheral nerve injuries in animal modesl (Semmler et al., 2023). The result showed that the silk-in-silk nerve conduit made from silk fibroin and spider dragline silk showed a significantly faster functional regeneration compared to empty conduits (Semmler et al., 2023).

Silk fibroin hydrogels have gained extensive utilisation in the field of tissue engineering (Lyu et al., 2023) across a spectrum of applications, encompassing the regeneration of cartilage (Chao et al., 2010), bone repair (Shi et al., 2017), and cornea repair (Barroso et al., 2022). These *B. mori* hydrogels have demonstrated efficacy in promoting cell activity and mitigating factors contributing to tissue damage. In the realm of cartilage tissue engineering, silk hydrogels prove advantageous by facilitating the encapsulation of therapeutic agents for the treatment of chondritis and incorporating biomaterials to bolster the regeneration of chondrocytes (Chao et al., 2010).

1.2 Silk processing for biomaterials

1.2.1 Hydrogels

Several methods exist for hydrogel formation exploiting physical and/or chemical crosslinking (Ahmed, 2015). Many materials used in the synthesis of hydrogels are synthetic polymers from petrochemicals such as poly-acrilamide, polymethacrylic acid or polyethylene oxide. However, natural polymers are used too (e.g. cellulose, starch, chitosan, silk (Ahmed, 2015)). Hydrogels synthesised from natural polymers have the advantage of typically being biodegradable and environmentally friendly. (Ahmed, 2015). Hydrogels

are applied across many applications and the medical applications are particularly relevant for this thesis (e.g. contact lenses, a wound sheet, drug delivery, tissue models etc). In the context of cancer three-dimensional models using hydrogels are particularly useful (Vasile et al., 2020).

In tissues, cells typically interact with a three-dimensional extracellular matrix (Chaudhuri, 2017). Extracellular matrix has physical and biochemical properties which play a crucial role in cell behaviour regulation. To improve our understanding of the impact of extracellular matrix on cell behaviour, hydrogels have been developed to mimic extracellular matrix structures and mechanics (Chaudhuri, 2017). One factor to be considered is the tissue mechanics of the extracellular matrix and its impact on cell biology. For these hydrogel-based culture substrates, hydrogel was demonstrated to influence cell migration, differentiation and proliferation that were substrate-specific (Tibbitt and Anseth, 2009).

1.2.1.1 Polymeric hydrogels

Hydrogels are hydrophilic polymers that have a crosslinked structure (Lu et al., 2018). Most hydrogels are synthesised from polymers with an acid group in their molecular chain that can be ionised (Ahmed, 2015). Therefore, when the hydrogel is immersed in water, the hydrogen atoms in the polymer chain react with water. This causes a positive charge (H_3O^+) and a negative charge in the polymer chain (Gun'ko et al., 2017). The negative charge of the polymer chains creates a repulsion between the chains and forces the related chains apart. Hydrogen atoms in the aqueous phase form hydrogen bonds with a negatively charged polymer chains (Gun'ko et al., 2017). This mechanism ‘traps’ water molecules within the hydrogel. However, the hydrogel is insoluble due to its lattice structure. (Gun'ko et al., 2017). The capacity of a hydrogel to absorb water depends on many factors, including the amount of hydrophilic group, osmotic pressure, and pores between polymer chains of the hydrogel (Ranganathan et al., 2018). The larger the gaps or porosity in the structure the more water can ingress into the hydrogel.

1.2.1.2 Silk hydrogels

An interesting biopolymer is silk. Silk-based hydrogels have emerged as valuable substrates with diverse applications including biomedicine (Zheng and Zuo, 2021), for example cell culture (Abbott et al., 2016, Osama et al., 2018, Phuagkhaopong et al., 2021), tissue engineering (Osama et al., 2018, Chao et al., 2010), and drug delivery (Haghighattalab et al., 2022, Seib, 2018). Self-assembled silk fibroin has shown suitable mechanical properties, adjustable degradation rates, straightforward manufacturing processes and favourable response from host tissues after implantation *in vivo*, rendering them highly appealing for various biomedical purposes (Lyu et al., 2023, Kapoor and Kundu, 2016, Holland et al., 2019).

To formulate these silk hydrogels, silk proteins are often combined with either natural or synthetic polymers (Holland et al., 2019, Zheng and Zuo, 2021, Seib, 2018). These hydrogel products can be broadly categorised into two main groups based on their cross-linking mechanisms: physical and chemical hydrogels (Holland et al., 2019, Zheng and Zuo, 2021, Seib, 2018). In physical cross-linking, silk fibroin molecules assemble through non-covalent bonds, giving rise to hydrogels via physical interactions such as hydrogen bonding (Figure 1.5), hydrophobic interactions, electrostatic interactions, ionic interactions, and chain entanglement (Holland et al., 2019, Zheng and Zuo, 2021). Common techniques for achieving physical cross-linking, in short timescales, exploits ultrasonication, shearing, the application of electric fields, temperature modulation, pH adjustment, and the use of organic solvents and surfactants (Holland et al., 2019, Zheng and Zuo, 2021, Seib, 2018).

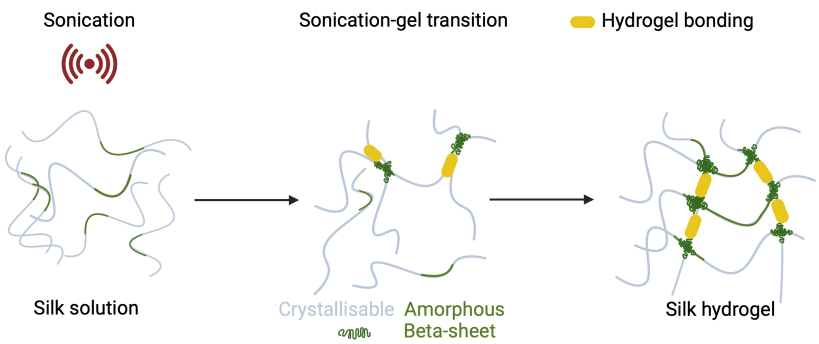

Figure 1.5 Physical cross-linked silk hydrogel using ultrasonication technique.

In contrast, chemical cross-linking involves the formation of covalent bonds between silk fibroin molecular chains, leading to the establishment of stable cross-linking points and the development of a spatial network structure (Zheng and Zuo, 2021). Hydrogels formed via chemical cross-linking typically exhibit superior physical stability and mechanical strength compared to those created through physical cross-linking. Common techniques for preparing chemically cross-linked hydrogels include photopolymerisation, the use of chemical cross-linking agents (e.g. creating di-tyrosine bonds), and enzyme-induced cross-linking (Zheng and Zuo, 2021, Seib, 2018).

Silk hydrogels can encapsulate drugs or therapeutic agents, enabling controlled release over time (Seib, 2018). For example, self-assembled silk hydrogels were developed for breast cancer therapy and pre-clinical testing (Seib, 2018). The study reported that locally injected silk hydrogels loaded with doxorubicin showed excellent antitumor response in mice and reduced metastatic spread *in vivo* (Seib, 2018). Another study assessed the use of self-assembled silk hydrogels as a carrier for encapsulating two bioactive agents aimed at enhancing the maxillary sinus floor in rabbits. The findings showed that silk hydrogels have the potential to serve as an injectable medium for the controlled delivery of multiple growth factors, offering a minimally invasive method to facilitate the regeneration of irregular bone voids (Zhang et al., 2011).

In the specific context of this thesis, the ultrasonic method was employed for the assembly of silk hydrogels. This method leverages ultrasound to accelerate the intermolecular interactions within silk fibroin, inducing structural changes that lead to the formation of physically crosslinked hydrogels (Wang et al., 2008, Zheng and Zuo, 2021). Osama et al., a former member of the Seib Lab, demonstrated the sonication-induced 1-5 % w/v of silk hydrogel using 30 % amplitude for 3 to 6 cycles (1 cycle consisted of 30 seconds on and 30 seconds off) could be used as a mesenchymal stem cell (MSC) delivery matrix (Osama et al., 2018). The result showed that 3% w/v silk hydrogels provided optimal support for MSC viability and distribution (Osama et al., 2018). In subsequent studies this technique was also used *in vivo*. Here, the 4% w/v of silk fibroin solution was sonicated for 15-45 seconds at 15 % amplitude to the solution-gel transition in situ. Hydrogel formation was demonstrated to support the de novo formation and migration of neuronal precursor cells within the stroke cavity (Gorenkova et al., 2019). This study showed that self-assembling hydrogels filled the stroke cavity with excellent space conformity and had no adverse morbidity or mortality (Gorenkova et al., 2019). In addition, Phuagkhaopong et al. demonstrated the impact of 4% w/v of silk hydrogel on MSC biology in two dimensions (Phuagkhaopong et al., 2021).

1.2.2 Nanoparticles

Nanoparticles have been widely used for managing the release of drugs and transporting a wide range of therapeutic substances, including proteins, peptides, and small molecules, to specific cells and tissues. Nanoparticles, typically fall within the size range of 1 nanometer to 1,000 nanometers, and are extensively investigated as promising vehicles for drug delivery with several of these products licenced for use in humans (Đorđević et al., 2022). However, also new materials are being investigated within this field, including silks. Both *B. mori* and *A. mylitta* silkworms produce silk that can be processed into nanoparticles for various applications, including drug delivery and tissue engineering.

1.2.2.1 Silk nanoparticles

1.2.2.2 *B. mori* silk Nanoparticles

Lately, fibroin has found increasing utility in nanoparticle formulation due to its favourable characteristics for nanoparticle development (Baruah et al., 2020, Zhao et al., 2015, Wongpinyochit et al., 2016, Seib, 2018). These characteristics encompass high water solubility, biodegradability, biocompatibility, ease of fabrication, suitability for freeze-drying, high efficiency in drug entrapment, substantial drug loading capacity, the ability to control particle sizes and release profiles, and the capacity for surface modification (Baruah et al., 2020, Zhao et al., 2015, Wongpinyochit et al., 2016, Seib, 2018).

Similar to pure fibroin, silk nanoparticles have also demonstrated safety and biocompatibility in a wide range of applications, both in controlled laboratory settings (*in vitro*) and within living organisms (*in vivo*) (Baruah et al., 2020, Zhao et al., 2015, Wongpinyochit et al., 2016, Seib, 2018). The earliest formulation of silk nanoparticles was achieved through the desolvation method (coacervation or nanoprecipitation) (Zhang et al., 2007, Wongpinyochit et al., 2016). Subsequently, various methods have been developed including the ball milling (Rajkhowa et al., 2008), bead milling (Kazemimostaghim et al., 2013), salting out (Mathur and Gupta, 2010), and supercritical fluid (Chen et al., 2018a). Each method possesses its unique advantages and drawbacks, yielding nanoparticles of differing sizes. Therefore, the selection of the method is crucial when formulating nanoparticles. In this study, the Matthew semi-batch desolvation method was used for silk nanoparticle synthesis (Matthew et al., 2020). The protocol was conducted using drop-by-drop nanoprecipitation (Matthew et al., 2020). Silk nanoparticles manufacture with the Matthew semi-batch format were consistent regarding particle attributes, standardised, and enabled higher-throughput manufacture (Matthew et al., 2020).

B. mori silk nanoparticles have been used as a drug delivery system, often for the delivery of chemotherapy drugs. Chen et al. reported that indocyanine

encapsulated silk fibroin nanoparticles resulted in high photothermal therapy efficiency and potential as a delivery system for sustained cancer therapy (Chen et al., 2018a). Pham et al. introduced and characterised three novel α-mangostin loaded crosslinked silk fibroin nanoparticles for the cancer treatment (Pham et al., 2019).

1.2.2.3 *A. mylitta* (Tasar) silk Nanoparticles

The silk fibroin obtained from the Indian tropical Tasar silkworm *A. mylitta* has been used for the fabrication of nanoparticles (Subia et al., 2014, Kundu et al., 2010). Tasar silk nanoparticles contain abundant aspartic and arginine amino acids, which can form Arg-Gly-Asp (RGD) sequences. These sequences play a crucial role in enabling the attachment of drugs and other molecules (Kundu et al., 2010, Subia et al., 2014). Enhancing these nanoparticles with coatings or the attachment of targeting molecules helps to effectively increase their specificity and cell targeting (Kundu et al., 2010, Subia et al., 2014). Tasar silk fibroin naturally contains RGD sequences, which interact with integrin molecules on the cell surface, promoting enhanced cellular attachment (Kundu et al., 2010, Subia et al., 2014, Holland et al., 2019). The incorporation of RGD into this fibroin can improve cellular attachment (and hence targeting). First-generation Tasar silk nanoparticles used liquid silk extracted directly from the silk gland. This liquid silk was desolvated, employing dimethyl sulfoxide (DMSO) as the desolvating agent (Kundu et al., 2010, Subia et al., 2014). Kundu and colleagues observed that the release of VEGF from these nanoparticles *in vitro* experiments exhibited a notably sustained pattern over a period of three weeks, indicating the potential utility of these nanoparticles as a vehicle for delivering growth factors (Kundu et al., 2010). In this thesis, Tasar silk fibroin was prepared using Tasar cocoons rather than extracting the silk from the silk gland of live silkworms (Dash et al., 2007). Tasar silk nanoparticles were assembled using a NanoAssemblr microfluidic system.

1.3 Silica nanoparticles

Over the past 10 years, mesoporous silica nanoparticles have been receiving increasing attention for biomedical applications (Trewyn et al., 2007). With the optimised mesoporous structure and high surface area, silica is widely used in drug delivery systems (Tang et al., 2012). Mesoporous silica helps drugs transported rapidly and specifically to the target organ. As a nanocarrier, mesoporous silica nanoparticles have been widely explored (e.g. g bone, tissue engineering, inflammation, diabetes, and cancer) (Tang et al., 2012). The mesoporous silica synthesis is based on the formation of a liquid crystalline mesophase of an amphiphilic molecule that serves as a template for the polymerisation of orthosilicic acid (Trewyn et al., 2007). The synthesis can be performed either in the acidic or basic state, and the source of the silica can be fuming silica, sodium silicate or tetra-alkyl oxide silane (Trewyn et al., 2007). The unique structure of mesoporous silica helps with efficient drug loading and controlled release. The mesoporous properties include pore size, porosity amount of drug loading, and surface properties (Jafari et al., 2019). Control of particle size, shape, pore size and pore geometry are important for biomedical applications (Narayan et al., 2018). Particle size and morphology can be designed to spherical, rod- to wormlike structures by adjusting the molar ratio of silica substrate and surfactant, pH control using base catalysts, addition of a co-solvent or swelling agent, and the introduction of the organo-alkoxysilane substrate during the reaction of co-condensation (Narayan et al., 2018).

Silica-based nanoparticles have been used for various biomedical application including bioanalytical formats (Wang et al., 2008), bioimaging (Selvan, 2010), and controlled drug release and delivery (Yang et al., 2012) because it has a unique optical property, low density, high surface area, high adsorption, and low toxicity (Bitar et al., 2012).

Silica nanoparticles also have been used with hydrogels to increase their mechanical properties. For example, a previous study used cellulose silica nanocomposite aerogel to create strong hydrogels that were flexible, had a

large surface area, and low thermal conductivity (Cai et al., 2012). Yang synthesised hydrogels by exploiting in situ silica nanoparticle surface polymerisation using poly (acrylic acid) chains. The results showed that high silica nanoparticles cross-linking of the polymer improved the hydrogel stability (Yang et al., 2012).

1.4 Silk microfibres

B. mori silk fibres have found diverse clinical applications, such as in the production of knitted surgical meshes, silk sutures, and silk-based garments for the treatment of dermatological conditions (Holland et al., 2019). An engineered *B. mori* silk fibre framework, tailored to meet the mechanical demands of a natural human anterior cruciate ligament (ACL), demonstrated encouraging outcomes by facilitating the adherence, proliferation, and specialisation of adult human bone marrow stromal cells (Altman et al., 2002). These findings suggest its prospective utility as a biomaterial for the purpose of tissue engineering ACLs (Altman et al., 2002).

The preparation of silk microfibres from 60-minute degummed *B. mori* and *A. mylitta* (Tasar) silk fibres followed established protocols (Mandal et al., 2012). The process of alkaline hydrolysis can break down proteins (Mandal et al., 2012). Mandal and colleagues reported that the length of the silk microfibres obtained through this process was inversely related to the duration of hydrolysis (Mandal et al., 2012). The use of sodium hydroxide as an alkali initiates the hydrolysis of amide bonds, resulting in the formation of carboxylic acids and amines or ammonia, which can be detected by smell during the reaction (Mandal et al., 2012). Silk fibres have been utilised to enhance the mechanical properties of scaffolds due to their excellent mechanical characteristics, biocompatibility, and ease of manufacturing (Tonsomboon et al., 2017, Kim, 2021). Silk fibres are known to effectively reinforce and substantially improve the mechanical attributes of scaffolds (Mandal et al., 2012, Thu-Hien et al., 2018) and a few applications for hydrogels (Yodmuang et al., 2015, Liu et al., 2019, Kim, 2021).

1.5 Nanoparticles and microfibres composite silk hydrogels

Nanoparticle hydrogel composites have been used to modify construct characteristics including mechanics, optics, and responsiveness. Polymers used include collagen (Nam et al., 2016), alginate (Zhao et al., 2010), polyethylene glycol (McKinnon et al., 2014), silk (Sood et al., 2019) and silicon (Jaeger et al., 2013). Hydrogel particles can be magnetised by the incorporation of magnetic nanoparticles, thereby facilitating separation and recycling (Dannert et al., 2019). These composite systems have been proposed for drug delivery applications or included in hydrogels for studying their swelling properties. There are many types of nanoparticles hydrogel composite described in the literature but in this thesis would focus on silica (serving as a control) silk (breaking new ground) nanoparticles hydrogel composite. Previous work investigated the adhesion property of colloidal mesoporous silica nanoparticles embedded with poly-dimethylacrylamide hydrogels (Kim et al., 2017). The result showed that mesoporous silica nanoparticles enabled stronger adhesion between two hydrogels than the non-porous silica nanoparticles (Kim et al., 2017).

The integration of silk fibres into hydrogel matrices has emerged as a strategy for bolstering the mechanical strength of the hydrogel (Yodmuang et al., 2015, Liu et al., 2019, Kim, 2021). Silk microfibres have demonstrated their potential for fortifying hydrogel constructs (Yodmuang et al., 2015, Liu et al., 2019, Xiao et al., 2018, Kim, 2021). These microfibres not only offer mechanical support but also have a positive impact on the cellular behaviour (Yodmuang et al., 2015, Liu et al., 2019, Xiao et al., 2018, Kim, 2021). For example, the incorporation of 2% (w/v) *B. mori* fibers, each 500 μm in length, into silk hydrogels resulted in an almost twofold increase in the mechanical strength of the hydrogel. This augmentation offers mature chondrocytes a structural and mechanical microenvironment conducive to robust cartilage matrix deposition (Yodmuang et al., 2015) .

In this thesis both prostate cancer and stem cells were used to test the hydrogel culture substrates. To appreciate the work of this thesis within the

context of these cells, it is important to have a background regarding these cells.

1.6 DU-145 (prostate cancer) cell line model

Cancer is one of the leading causes of mortality in humans (Zhang et al., 2023). In the United Kingdom prostate cancer is the second most common cancer in males after lung cancer and the mortality trend is increasing (Bray et al., 2018). Several preclinical models for prostate cancer have been established to elucidate the intricate mechanisms responsible for the development of treatment resistance in prostate cancer (Namekawa et al., 2019). Three prostate cancer cell lines created in the 1970s and 1980s, specifically LNCaP (Namekawa et al., 2019), DU-145 (Mickey et al., 1977), and PC-3 (Kaighn et al., 1979), remain widely employed in most published research studies. Notably, the DU145 cell line originated from a metastatic brain lesion of human prostate cancer, and like PC3 cells, DU145 cells are refractory to hormonal treatment and do not express prostate-specific antigen (PSA) (Stone et al., 1978). The DU-145 cell line possesses characteristics of adenocarcinoma and is particularly valuable for prostate cancer investigations because it can give rise to bone metastases *in vivo* models (Tae and Chang, 2023). The DU-145 cell line maintains its adenocarcinoma attributes, offering the advantage of producing experimental results that better predict clinical outcomes in human subjects (Tae and Chang, 2023). Nonetheless, the DU-145 cell line is insensitive to androgens. It has the limitation of forming osteolytic lesions, which restricts their applicability in research pertaining to hormone-sensitive prostate cancer and osteoblastic bone lesions (Tae and Chang, 2023). Overall, DU-145 cells remain a useful tool to study prostate cancer. This opens opportunities to improve our cancer biology understanding and, ultimately, options to treat this disease. Therefore, using DU-145 cells to trial novel culture substrates is relevant and important.

1.7 Induced pluripotent stem cell derived mesenchymal stem cell (iPSC-Derived MSCs) model.

Mesenchymal stem cells (MSCs) are a group of adherent cells that can be sourced from various locations, including bone marrow, adipose tissue, or placental tissue. They can differentiate into different types of tissues, namely bone, cartilage, and adipose tissues (Lee et al., 2023). However, MSCs obtained directly from primary tissues have limited proliferative capacity and tend to undergo replicative senescence during *in vitro* expansion, which restricts their broader applications in clinical cell therapy trials (Bruder et al., 1997). Additionally, the functional diversity within MSC populations has posed challenges for standardisation in clinical settings (Costa et al., 2021), and discrepancies arising during *in vitro* culture further complicate maintaining a consistent source (Wagner et al., 2008, Larson et al., 2010). Furthermore, the quality of MSCs can vary significantly among donors, making it challenging to achieve uniform biological activity on a large scale or to standardise outcomes in both clinical and preclinical studies (Wagner et al., 2009, Xin et al., 2010, Viswanathan et al., 2014).

To address these challenges, recent research has shifted its focus towards generating mesenchymal stem-like cells from pluripotent stem cells, including embryonic stem cells, and induced pluripotent stem cells (iPSCs) (Zhang et al., 2021a). iPSC derived MSCs, have been successfully created and exhibit phenotypic and functional characteristics akin to traditional MSCs (Frobel et al., 2014, Moslem et al., 2015). Therefore, iPSC-MSCs are seen as an alternative and more standardised source of MSCs, characterised by a higher potential for *ex vivo* expansion (Frobel et al., 2014, Moslem et al., 2015). Consequently, iPSC-MSCs have been employed in a wide array of cell therapy trials, encompassing applications such as bone defect repair (Sheyn et al., 2016), the delivery of prodrug-converting enzymes for cancer therapy (Ullah et al., 2017), periodontal regeneration (Hynes et al., 2013), nerve injury repair (Chen et al., 2019), and other personalised regenerative cell therapies (Lin et

al., 2016). Therefore, these iPSC-MSCs are highly relevant for tissue engineering. Therefore, the use of iPSC-MSCs in this thesis is timely.

1.8 Hypothesis and specific aims

The overall hypothesis of this thesis is that incorporating nanoparticles and microfibres to reinforce silk hydrogels allows tuning of bulk mechanics and cell adhesion thereby controlling the cell-material interface. My working hypothesis for this thesis is that the inclusion of nanoparticles and microfibres into physically crosslinked *B. mori* silk hydrogels would alter the hydrogel mechanics and modulate cell-cell attachment.

To test this hypothesis, I synthesised and characterised silica nanoparticles (Chapter 2), silk nanoparticles (Chapter 3), silk microfibres (Chapter 4) and embedded these within self-assembling silk hydrogels. *In vitro* experiments were then conducted using DU-145 cells (prostate cancer cell line) (Chapter 3) and induced pluripotent stem cell-derived MSCs (iPSCs-MSCs) (Chapter 4), which were seeded onto silk hydrogel composites containing nanoparticles and microfibres, respectively.

The specific aims of this thesis were:

(i) To create hydrogels functionalised with porous and non-porous silica nanoparticles and determine the mechanical properties of these silk hydrogel composites (Chapter 2).

Therefore, the objectives were:

(1) To synthesise and characterise non-porous and porous silica nanoparticles in the size range between 100-150 nm.

(2) To determine the mechanical properties of silk hydrogel in the presence of 0.1% and 5% w/v non-porous and porous silica nanoparticles.

(ii) To investigate the impact of self-assembly silk hydrogels functionlised with nanoparticles on DU-145 cell adhesion (Chapter 3).

Therefore, the objectives were:

(1) To synthesise and characterise *B. mori* and *A. mylitta* (Tasar) silk nanoparticles in the size range between 100-150 nm.

(2) To determine the mechanical properties of silk hydrogel in the presence of 0.05% and 0.5% w/v of *B. mori*, *A. mylitta* (Tasar) silk and nonporous silica nanoparticles.

(3) To determine the cell viability and cell attachment of DU-145 on silk hydrogels with and without nanoparticles

(iii) To investigate the short-term impact of viscoelastic silk hydrogels functionlised with silk microfibres on iPSCs-MSC adhesion (Chapter 4).

Therefore, the objectives were:

(1) To synthesise and characterise *B. mori* and *A. mylitta* (Tasar) silk microfibres in the size range between 250-500 μm.

(2) To determine the mechanical properties of silk hydrogel in the presence of 2% and 10% w/v of *B. mori* and *A. mylitta* (Tasar) silk microfibres

(3) To determine the cell viability, cell attachment and cytoskeleton structure of iPSCs-MSC on these silk hydrogel substrates

The result and discussion sections of Chapter 2 and Chapter 4 were constructed separately, while Chapter 3 combined them due to the stylistic requirements of the journal.

Chapter 2

Manufacture of silica nanoparticles

Chapter summary:

This chapter was focused on the synthesis and characterisation of porous and non-porous silica nanoparticles. All particles were characterised using dynamic light scattering (DLS), nitrogen adsorption, Fourier-transform infrared spectroscopy (FTIR), and scanning electron microscopy (SEM). Stober and commercial SBA-15 silica nanoparticles were added to silk hydrogels to determine the mechanical properties using rheology with concentrations of 0.10% and 5% w/v. Then, DU-145 prostate cancer cells were seeded on these silk hydrogel composites, and the cell viability was measured using the 3-(4,5-dimetylthiazol-2-yl)-2,5-diphenyl-2H-tetrazolium bromide (MTT) assay. In this chapter, the amount of Stober silica nanoparticles that were added to silk hydrogels was tested with DU-145 cells. In Chapter 3, the amount of Stober silica nanoparticle was further refined using 0.05 and 0.50% w/v.

2.1 Abstract

Hydrogels provide a three-dimensional matrix that is promising for tissue culture, for example *in vitro* dedifferentiation and organoid culture. However, many *in vitro* systems lack both long-term stability and relevant mechanical properties and thus provide a sub-optimal cell niche. One interesting strategy to modulate hydrogel performance is to embed particles within hydrogels. This study aimed to include silica nanoparticles into *B. mori* silk-based hydrogels to permit tailoring of the mechanical properties and enhance cell function, ultimately regulating cell biology. These silica particles were in the 100 to 400 nm size range and had a polydispersity index ranging from 0.02 to 0.49. All particles were characterised using dynamic light scattering, nitrogen adsorption and scanning electron microscopy (SEM). Next, selected particles were incorporated into the silk hydrogel. The non-porous and commercial silica nanoparticles (SBA-15) were embedded both at 0.10 and 5 % w/v

concentration. This was possible because sonication energy was used to trigger the solution-gel transition of 3% w/v *B. mori* liquid. During the solution-gel transition, particles were added to the system. All findings indicated that the initial modulus (stiffness) of silk hydrogels was increased with increasing concentration of both SBA-15 (2.11 vs. 1.48 kPa) and non-porous silica (2.14 vs. 2.05 kPa) nanoparticles. The half stress-relaxation time of silk hydrogels was also increased with increasing concentration of silica nanoparticles. These findings prove how silica nanoparticles impact the mechanical properties of silk hydrogels.

2.2 Introduction

Tissue engineering has emerged at the intersection of biology, materials science, and engineering, with the ambitious goal of developing functional and viable replacements for damaged or diseased tissues and organs (Caddeo et al., 2017). This multidisciplinary approach seeks to overcome the limitations of traditional medical interventions by harnessing the power of biomaterials to guide and support the regeneration of complex biological systems (Caddeo et al., 2017).

Biomaterials play a pivotal role in many purposes, especially mimicking the extracellular matrix (ECM), the intricate network of proteins and other molecules that surround cells in native tissues (Boso et al., 2020, Xing et al., 2020). They can create an environment that facilitates cell adhesion, proliferation, differentiation, and ultimately, the formation of functional tissue constructs (Xing et al., 2020). In recent years, the combination of biomaterials and nanotechnology has led to innovative advancements in tissue engineering and regenerative medicine. Silk hydrogels have emerged as a versatile platform due to their unique biocompatibility, tuneable mechanical properties, and controllable degradation kinetics (Lyu et al., 2023). These attributes make silk hydrogels an attractive candidate for various biomedical applications, ranging from wound healing to drug delivery (Holland et al., 2019, Egan et al., 2022, Zheng and Zuo, 2021).

Silk, a naturally occurring protein produced by silkworms and spiders, has been utilised for centuries for its strength, durability, and luxurious texture (Holland et al., 2019). In recent years, the unique characteristics of silk have been harnessed to create biomaterials that hold promise for tissue engineering applications (Lyu et al., 2023). Silk biomaterials possess a rare combination of biocompatibility, biodegradability, mechanical versatility, and processability, making them a compelling choice for designing hydrogel that can effectively support tissue regeneration (Abbott et al., 2016, Holland et al., 2019, Liu et al., 2022).

Silk hydrogel is biocompatible and well-tolerated by living tissues (Onder et al., 2022). This hydrogel does not elicit strong immune responses (Onder et al., 2022), making it suitable for implantation and cell interaction (Liu et al., 2022, Lyu et al., 2023). Silk hydrogel possesses tuneable mechanical properties. These hydrogels can be engineered to match the mechanical properties of different tissues, providing the necessary support during tissue regeneration (Phuagkhaopong et al., 2021, Bertsch et al., 2023, Su et al., 2023). Silk hydrogel has been researched extensively and is effective in engineering a variety of tissues in different cell types (Phuagkhaopong et al., 2021, Abbott et al., 2016, Pierantoni et al., 2021).

Silica nanoparticles are generally considered to be biocompatible, and extensive research has been done to understand their safety profile (Mamaeva et al., 2013, Selvarajan et al., 2020, Lérida-Viso et al., 2023). Silica nanoparticles can enhance the mechanical strength, stability, and structural integrity of hydrogels (Cheng et al., 2021, Kharlampieva et al., 2010, Mieszawska et al., 2010). These improved material properties in turn are vital for creating silk hydrogel in tissue engineering and regenerative medicine applications (Kharlampieva et al., 2010, Mieszawska et al., 2010, Cheng et al., 2021). Silica nanoparticles can be functionalised to modify their surface properties, such as charge, hydrophobicity, and bioactivity. This allows for tailoring the interactions between the material and cells, influencing cell attachment, proliferation, and differentiation. Investigating cell attachment to a composite of silk hydrogel and silica nanoparticles can provide valuable

information on the cytotoxicity and biocompatibility of the material (Kharlampieva et al., 2010, Mieszawska et al., 2010, Cheng et al., 2021).

To further enhance the functionality and therapeutic potential of silk hydrogels, the incorporation of nanoparticles has gained significant attention. The use of silk hydrogels and silica nanoparticles, whether non-porous or porous, presents exciting opportunities for creating biomaterials with superior mechanical, biological, and chemical attributes (Cheng et al., 2021). This innovative combination leverages the complementary benefits of silk-based hydrogels and the distinct characteristics of silica nanoparticles, resulting in the production of advanced materials with enhanced structural strength and versatile functionalities (Cheng et al., 2021).

In this chapter, the first set of experiments explored the use of functionalised silk hydrogels in conjunction with non-porous and porous silica nanoparticles to study prostate cancer. For this experiment, the DU145 prostate cancer cell line was used. Studying the interactions between cancer cells and biomaterials, such as silk hydrogel with nanoparticles, can offer valuable information about cancer cell behaviour. By examining how DU-145 cells attach to this composite material, we can gain insight into the cellular and molecular processes at work. In future, this research could potentially reveal important signalling pathways, adhesion molecules, and other factors that contribute to cell-material interactions.

The objectives of this work are divided into three parts including: (1) synthesis of porous and non-porous silica particles using different techniques, (2) physically cross-linked silk hydrogels synthesis, and (3) silk hydrogel particle composites. First, porosity-tuned silica particles and silk nanoparticles were synthesised. Next, the low (0.10% w/v) and high concentration (5% w/v) porous and non-porous nanoparticles were embedded within 3% w/v of silk hydrogels to alter the mechanical properties of silk hydrogels while Tasar silk nanoparticles would be included to tune cell adhesion in chapter 3 of this thesis.

2.3 Materials and Methods

2.3.1 Synthesis of silica nanoparticles

2.3.1.1 Stober silica nanoparticles

Non-porous silica particles between 100-150 nm in size were synthesised using the conventional Stober protocol (Khanna et al., 2018a). The Stober silica protocol was modified into four different conditions.

Condition 1

In brief, 3.00 mL of 28% ammonium hydroxide (NH_4OH) was added to 50 mL of 95% ethanol and stirred for 5 min, followed by the addition of 1.50 mL of tetraethyl orthosilicate (TEOS). The reaction was stirred at 18 °C for 18 h. The silica product was collected by centrifugation at 48,384 × g at 20 °C for 15 min (Avanti™ J-E High-Performance Centrifuge, Beckman Coulter®, California, United States). The solid white product was washed three times with 30 mL of 95% w/v of ethanol and dried overnight in an oven at 80 °C.

Variations to this protocol included a reduction in reaction time from 12 h to 6, 3, and 2 h.

Condition 2

The Stober method uses ethanol for TEOS hydrolysis. To reduce the size of silica nanoparticles, condition 1 was used but the volume of ethanol was decreased to 25 mL.

Condition 3

TEOS is a source of silica. To reduce the size of silica nanoparticles, condition 1 was modified by decreasing the TEOS volume from 1.50 mL to 1 mL.

Condition 4

Ammonium hydroxide acts as a basic catalyst of Stober silica reaction. The amount of NH_4OH is directly proportional to the size of silica nanoparticles

(Greasley et al, 2016). Therefore, the NH_4OH volume was reduced from 3.00 mL to 1.50 mL using 2-, 6-, and 12 h reaction times.

2.3.1.2 Mesoporous silica synthesis

2.3.1.2.1 The biphase silica synthesis

The synthesis of biphase silica particles with tuneable dimension and pore size was described previously (Shen et al., 2014). In brief, to obtain three-dimensional dendritic mesoporous silica nanoparticles with generational and centre-radical mesoporous channels, a one-pot biphasic stratification approach by continuous growth using the cationic surfactant cetyltrimethylammonium chloride (CTAC) as a template, TEOS as a silica source, triethanolamine (TEA) as a catalyst and organic solvent 1-octadecene as an emulsion agent, was employed. A typical synthesis of the 3D-dendritic mesoporous silica nanoparticles with three generations was performed as follows:

First, 24 mL of (25% w/w) CTAC solution and 0.18 g of TEA were added to 36 mL of water and stirred gently at 60 °C for 1 h in a 100-mL round bottom flask, then 20 mL of (20% v/v) TEOS in 1-octadecene was carefully added to the water-CTAC-TEA solution and kept at 60 °C in a water bath while stirring. The stirring rate was set to be ~ 150 rpm. The reaction was then kept at a 60 °C constant temperature with continuous stirring for 12 h to obtain the first-generation products. Next, the upper phase, 1-octadecene solution, was completely removed and replaced with 20 mL of 20% v/v TEOS solution in decahydronaphthalene to keep the same reaction conditions for another 12 h for the growth of the second generation. For the third generation, the upper oil layer was changed to a TEOS-cyclohexane solution, while the reaction conditions were kept under the same conditions for 12 h. The products were collected by centrifugation at 48,384 $\times$ g at 20 °C for 15 min and washed three times with 30 mL of 95% w/v of ethanol to remove the residual reactants. Then, the collected products were extracted with 30 mL of 0.60% w/w ammonium nitrate (NH_4NO_3) ethanol solution at 60 °C for 6 h twice to remove the template. This product was then lyophilised to obtain the final

powder, which was stored at room temperature for the subsequent experiments. The heterogeneous oil-water stratification reaction system contains the TEOS solution as a silica source in a hydrophobic organic solvent as the upper oil phase, while the lower oyster white phase is the solution of the products, which contains CTAC as a template and TEA as a catalyst.

To obtain porous silica particles with tuneable dimensions between 50 - 100 nm and pore size between 4 - 5 nm, wormhole silica was synthesised based on Möller's protocol (Möller et al., 2007). MCM-41 type mesoporous silica was synthesised based on Costa's protocol (Costa et al., 2020).

Wormhole silica

To create wormhole silica nanoparticles, a mixture of 10.50 mL of ethanol and 64 mL of distilled water was prepared. Next, 10.40 mL of 25% w/w CTAC was added as a template. The molar ratio of TEOS to TEA was found to be an important factor in determining the average particle size (Möller and Bein, 2017). In this study, 4.13 mL of TEA was added, followed by stirring at 25 °C for 1 h. The solution was then heated to 60 °C and 1.45 mL of TEOS was added, followed by stirring for 2.50 h. The silica product was collected by centrifugation at 48,384 × g at 20 °C for 15 min. The solid white product was washed three times with 30 mL of 95% w/v of ethanol and dried overnight at 80 °C in the oven. The silica template was removed by calcination at 550°C for 6 h.

MCM-41 silica

In brief, 3.50 mL of 2 M NaOH solution was mixed with 480 mL of distilled water. Then, 1 g of CTAB) was added to the solution. The solution was stirred at 25°C overnight, followed by the addition of 5 mL TEOS. The reaction was heated at 80 °C for 2 h. The silica product was collected by centrifugation at 48,384 × g at 20 °C for 15 min. The solid white product was washed three times with 30 mL of distilled water and ethanol respectively and dried

overnight at 80 °C in the oven. The silica template was removed by calcination at 550°C for 6 h.

SBA-15 silica

Silica mesoporous SBA-15 was purchased from Sigma Aldrich (Sigma-Aldrich, Merck Life Science UK Limited, Dorset, UK). The manufacturer's reported size of SBA-15 is less than 150 nm with a pore size of 10 nm and a hexagonal pore morphology.

2.3.2 Particle size and zeta potential measurements by Dynamic Light Scattering (DLS)

2.3.2.1 Particle size measurement

The particle diameter of the synthesised mesoporous silica nanoparticles was determined by dynamic light scattering (DLS) measurements as detailed previously (Das et al., 2014). Briefly, freeze-dried silica nanoparticles were suspended in distilled water at 1 mg/mL, vortexed for 10 min, and sonicated for 30 s using a digitally controlled probe sonicator (Sonoplus® HD 2070, Bandelin, Berlin, Germany) fitted with a 23 cm long sonication tip (0.30 cm diameter tip and tapered over 8 cm). After sonication, the size of nanoparticles was measured using a Zetasizer Nano ZS® (Malvern Instruments, UK). The refractive index of water was 1.33 and the viscosity of distilled water was 0.89 Pa·s. The temperature during this process was set at 25 °C and the data analysis was performed in automatic mode using the instrument software. All measurements were performed in triplicate with each of the triplicates measured 5 times to obtain an average particle size measurement.

2.3.2.2 Zeta potential measurement

Zeta potential was measured with electrophoretic light scattering using Malvern Zetasizer Nano ZS®. Distilled water was used as a medium. All measurements were repeated three times, and average values were reported.

2.3.2.3 Particle sedimentation

The sedimentation behaviour of the Stober silica particles was monitored with condition 4 of non-porous silica nanoparticles in distilled water using the method described previously (Maitz et al., 2017). Briefly, 10 mg/ml nanoparticles were freshly prepared by vertexing and sonication at a 10% amplitude prior to transferring 1.50 ml samples to UV cuvettes. Absorbance due to nanoparticle-mediated light scattering was measured at different time points (0, 30, 60, and 90 min) after silica resuspension using a Zetasizer Nano ZS®. The refractive index of water was 1.33 and the viscosity of distilled water was 0.89 Pa·s. The temperature during this process was set at 25 °C. All measurements were performed in triplicate with each of the triplicates measured 5 times to obtain an average particles size measurement.

2.3.3 Determination of the chemical structure of silica nanoparticles using FTIR

The different functional groups on the surface of SiO_2 nanoparticles were based on (Feifel and Lisdat, 2011). Briefly, FTIR analysis was performed in a TENSOR II FTIR spectrometer (Bruker Optik GmbH, Ettlingen, Germany). Silica nanoparticles were exposed to 32 scans for background and 32 scans for the samples at 8 cm^{-1} resolutions over the wavenumber range 400 – 4000 cm^{-1}. The silica nanoparticles were measured twice.

2.3.4 Nanoparticle morphology using scanning electron microscopy (SEM)

Silica nanoparticles were deposited on the high-purity conductive double-sided adhesive carbon tape and pasted on an aluminium pin stub. Silica nanoparticles (porous and non-porous) were sputter-coated with 15 nm gold using an ACE200 low-vacuum sputter-coated (Leica Microsystems, Wetzlar, Germany). Then, the specimen pins were inserted in the SEM analysis chamber for imaging. The silica nanoparticles were measured using the Quanta FEG-ESEM® (FEI Company, Hillsboro, OR, USA; now part of Thermo

Fisher Scientific Inc., Waltham, MA, USA) with a 5-kV voltage at three magnifications (5000x, 20,000x, and 40,000x).

2.3.5 Pore volume and surface area of silica nanoparticles using nitrogen adsorption.

The surface area and pore size of porous silica nanoparticles were adjusted based on previous studies (Möller and Bein, 2017). In brief, SBA-15 and MCM-41 were characterised by nitrogen adsorption at 77 K using Quantachrome Autosorb IQ2® analyzer (Quantachrome Instruments, Boynton Beach, Florida, USA). Before adsorption measurement, 200 mg of SBA-14 and MCM-41 were degassed under vacuum at 200 °C for 18 h. Next, samples were outgassed at room temperature. The sample characteristics were calculated and analysed by ASiQwin software. The surface area of particles was analysed using the Brunauer–Emmett–Teller (BET) method while the pore volume was analysed using Barrett-Joyner-Halenda (BJH) method (Möller and Bein, 2017).

2.3.6 Manufacture of silk hydrogels

2.3.6.1 Preparation of silk fibroin solution from *B. mori* cocoons

The silk fibroin solution was prepared as detailed previously (Wongpinyochit et al., 2016). Briefly, *B. mori* cocoons were cut into 5 mm x 5 mm pieces and degummed using 2 L of 0.02 M sodium carbonate solution at 100 °C for 60 min. The degummed silk fibres were cooled to room temperature, rinsed three times with 1L of deionised water and dried in a fume hood overnight. The dried silk was dissolved in fresh 9.6 M LiBr solution using 1g of degummed silk fibre to 4 mL of LiBr at 60 °C for 3 h. This solution was dialysed against 1 L of deionised water using a dialysis cassette (molecular weight cut-off 3,500 Da) and the water was changed at 1, 3 and 6 h on the first day, on the next morning and evening, and again on the following morning. The silk solution was collected and centrifuged twice for 20 min at 5°C and 9.5000 × g. Next, the silk solution concentration was assessed by

drying followed by gravimetric analysis. The resulting silk solution was typically 4.50 % w/v and was stored at 4 °C until use.

2.3.6.2 Preparation of self-assembling silk hydrogels

The preparation of self-assembling silk hydrogels was described previously (Osama et al., 2018). Briefly, 4 mL of 3% w/v silk solution was prepared and transferred to 15 mL Falcon tubes. The sample was then sonicated using a digitally controlled probe sonicator (Sonoplus HD 2070®, Bandelin, Berlin, Germany) fitted with a 23 cm long sonication tip (0.3 cm diameter tip and tapered over 8 cm) at 30% amplitude for typically 4 sonication cycles on ice (one cycle consisted of 30 s on and 30 s off) to initiate the solution–gel transition**.** Silk hydrogels containing nanoparticles were generated by adding and mixing 0.10 or 0.50% w/v of silica, *B. mori* or Tasar silk nanoparticles to samples prior to the completion of the solution–gel transition.

2.3.7 Mechanical properties of silk hydrogels with and without non-porous silica nanoparticles analysis using rheology measurement.

In brief, samples were prepared in molds forming an 11 mm diameter with an average thickness of 9 mm. The 1 ml of 3%w/v silk hydrogels with 0.10 and 5 % w/v of silica particles (porous and non-porous) or without silica nanoparticles were prepared and equilibrated in 50 mL PBS overnight. The hydrogels were then subjected to rheology characterisation (Haake Mars (Liquid) Rheometer and Nicolet iS10 IR, Thermo Electron (Karisruhe), GmbH, Germany) using a 20 mm diameter plate set to 25 °C and appropriate gap size. The storage modulus (G') was measured using a time sweep over a strain of 0.01-100% at a frequency of 1 Hz. The stress-relaxation rate (G") was measured at a 15% strain to mimic the human extracellular matrix (Chaudhuri et al., 2016). The stress relaxation was recorded every 10 s to a total 500 s.

Doping Method 1

The 3% w/w silk solution was sonicated as detailed above to induce the solution-gel transition. Next, the silica powder was added to the silk sample undergoing solution-gel transition. Then, the sample was mixed and transferred to the molds.

Doping Method 2

Here, the silk stock solution doped with Stober silica and SBA-15 particles was prepared first (Figure 4.1.). The sample was then subjected to sonication to induce the solution-gel transition.

Stober SiNPs

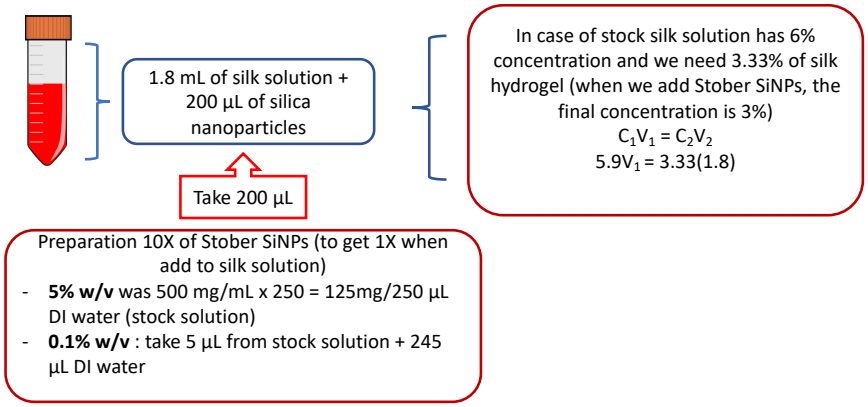

SBA-15

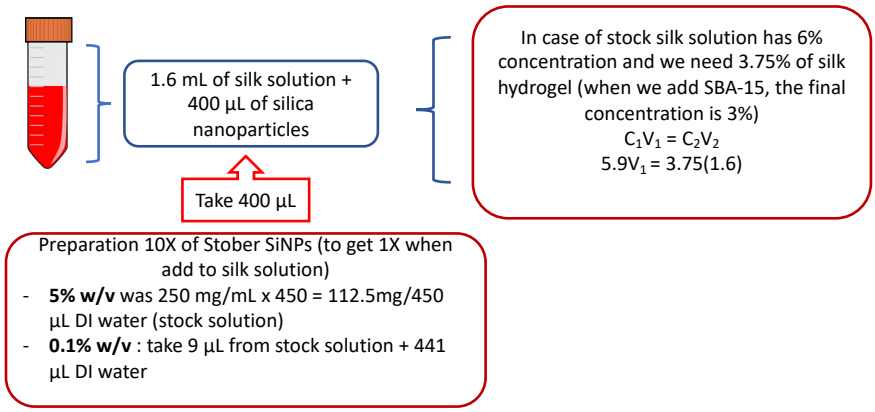

Figure 2.1 Doping method of silk hydrogels incorporated with Stober silica and SBA-15.

2.3.8 Secondary structure of 3% w/v silk hydrogels analysis using FTIR.

The self-assembling silk hydrogel secondary structure was assessed as detailed elsewhere (Matthew et al., 2020). Briefly, 3% w/v silk hydrogels were frozen overnight at -80 °C and lyophilised (Epsilon 2-4 LSCplus®, Christ, Germany). The secondary structure of the dried silk hydrogel was analysed with a TENSOR II FTIR® spectrometer (Bruker Optik GmbH, Ettlingen, Germany) using 128 scans at 4 cm^{-1} resolutions over the wavenumber range

400 – 4000 cm^{-1}. The secondary structures were assigned as the detailed previous (Matthew et al., 2020). Baseline and peak fit were corrected by OriginPro 2021 software as detailed previously. The amide I region (1595–1705) was identified and deconvoluted, as follows: 1605−1615 cm^{-1} as side chain/aggregated strands, 1616−1637 cm^{-1} and 1697−1703 cm^{-1} as β-sheet structure, 1638−1655 cm^{-1} as random coil structure, 1656−1662 cm^{-1} as α-helical bands and 1663−1696 cm^{-1} as β-turns. The air-dried film was used for a negative control and 70% ethanol-treated silk film was used for a positive control.

Statistical analyses

Data were plotted and analysed as detailed previously (Totten et al., 2017). Briefly, sample pairs were analysed by one-way ANOVA with Dunnett's multiple comparison test (Prism 9.2.0; GraphPad Software Inc., San Diego, CA, USA). Asterisks were used to denote statistical significance, as follows: *P < 0.05, **P < 0.01, ***P < 0.001. All data were presented as mean values ± standard deviation (SD). The number of independent experiments (n) is noted in each figure legend.

2.3 Results

2.4.1 Silica nanoparticles characterisation

2.4.1.1 Non-porous silica nanoparticles

In Condition 1, the silica nanoparticles had an average size of 105 nm ± 1.47 nm with a polydispersity (PDI) value of 0.13 ± 0.01 (as illustrated in Figure 2.2). The average zeta potential value was -31.20 mV ± 0.46 mV. When the volume of ethanol was decreased in Condition 2, the size of the silica nanoparticles increased significantly (403 nm ± 5.55 nm) with a PDI value of 0.04 ± 0.03. The average zeta potential value was -41.83 mV ± 0.25 mV. Under Condition 3, the silica nanoparticles were still significantly larger (146.9 nm ± 13.05 nm) than in Condition 1, with a PDI value of 0.46 ± 0.17. The average zeta potential value was -36.83 mV ± 1.16 mV.

However, the target size of silica nanoparticles was 150 nm. Therefore, Condition 1 was further optimised by reducing the reaction time from 12 h to 6, 3 and 2 h (Figure 2.3). After a 12 h reaction time, silica nanoparticles had an average size of 230.50 nm, a PDI of 0.06 and a zeta potential of -34.44 mV. A 6 h reaction time the average size was 216.80 nm with a PDI value of 0.02 and zeta potential of -29.37 mV. At the 3 and 2 h reaction times, the particle size was 214.03 nm and 199.90 nm, respectively with PDI values between 0.02 and 0.03 and zeta potential of -29.37 mV and -31.57 mV, respectively.

From these experiments, all nanoparticles were still larger than the desired 150 nm. Therefore, a new condition was designed where the volume of NH_4OH was reduced from 3.00 mL to 1.5 mL and 2, and 6 h of reaction time was used (Figure 2.4). The Stober silica nanoparticles after the 2 h reaction time had an average size of 176.30 ± 37.37 nm, a PDI of 0.49 ± 0.28 and a zeta potential of -33.34 ± 8.32 mV. After increasing the reaction time to 6 h, the particle size decreased to 122 ± 22.68 nm with a PDI of 0.31 ± 0.17 and a zeta potential of -37.79 ± 2.98 mV. The sedimentation behaviour of silica nanoparticles showed that the size and PDI value were not significantly different from time 0 (Figure 2.5).

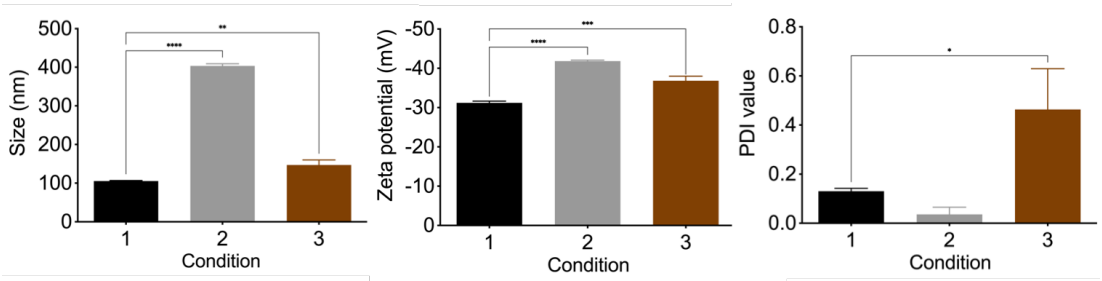

Figure 2.2 Impact of reaction conditions on silica particle characteristics**.** Stober silica nanoparticles properties, Condition 1 (same method as previously studied (Khanna et al., 2018a), Condition 2 (decrease the volume of ethanol), and Condition 3 (decrease of NH_4OH volume). Data are presented as mean ± SD, n=3 independent experiments.

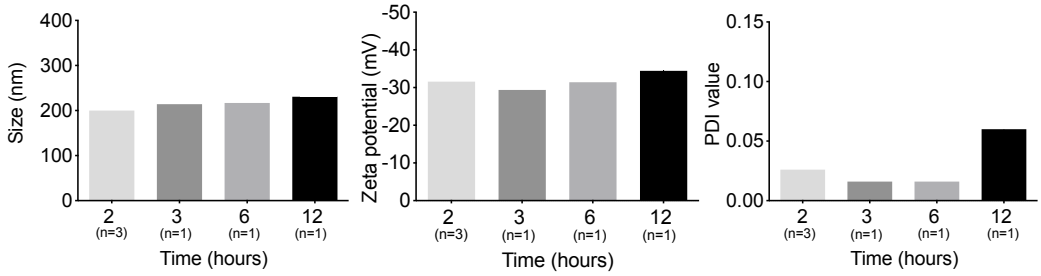

Figure 2.3 Impact of time on Stober silica particle characteristics. Based on condition 1 variations in reaction times range from 2 h to 12 h. The 12-hour reaction time was detailed previously (Khanna et al., 2018a). Data are presented as mean ± SD. n numbers are shown on the abscissa axes.

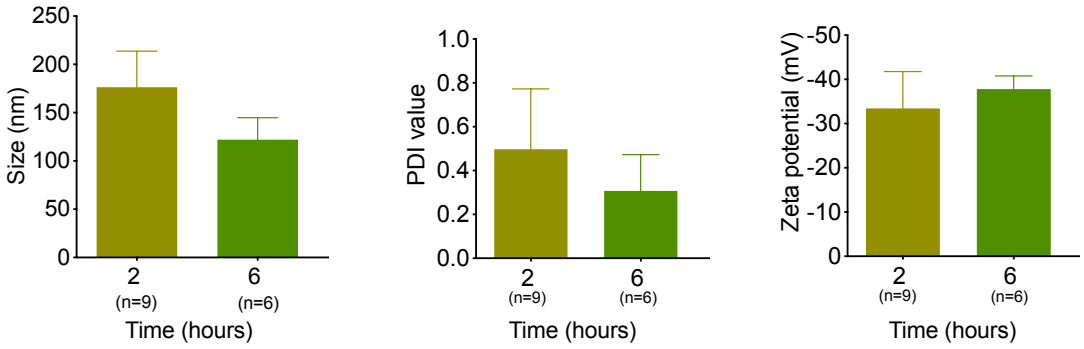

Figure 2.4 Impact of NH_4OH reduction on non-porous silica nanoparticle properties (Condition 4). Particle characteristics at the 2-, and 6 h reaction time including particle size, PDI, and zeta potential value. Data are presented as mean ± SD.

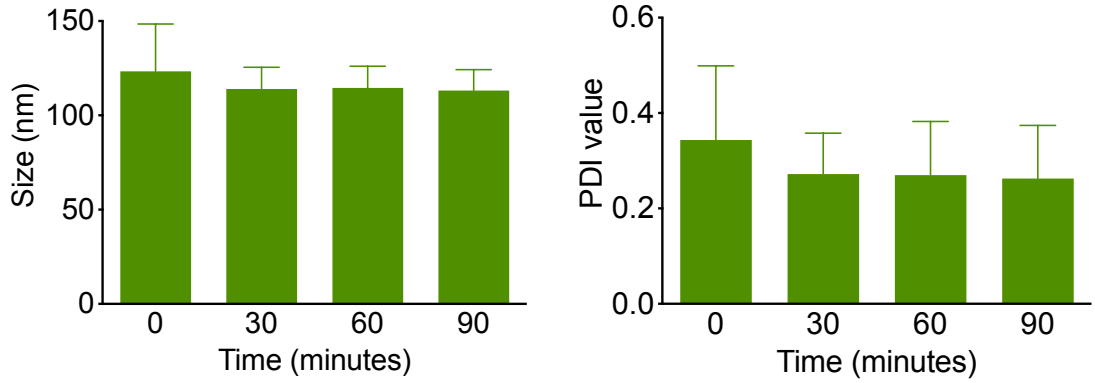

Figure 2.5 Sedimentation behaviour of Stober silica with decreased volume of NH_4OH after a 6 h reaction time (n=6). Data are presented as mean ± SD.

2.4.1.2 Synthesis of porous silica nanoparticles

The result showed that the wormhole silica nanoparticles had the smallest size while MCM-41 silica nanoparticles had the biggest size. The wormhole silica nanoparticles had an average size of 202.40 ± 69.84 nm with 0.44 ± 0.06 of PDI value (Figure 2.6). The zeta potential value was -17.84 ± 1.08 mV (Figure 2.6). Next, Biphase silica nanoparticles had an average size of 324.90 ± 4.62 nm with a PDI value of 0.10 ± 0.05 (Figure 2.6). The zeta potential was -17.50 ± 1.82 mV (Figure 2.6). The MCM-41 had the largest size which was 906 ± 236.50 nm with a PDI of 0.46 ± 0.16 (Figure 2.6). The zeta potential was -14.25 ± 17.44 mV. For the commercial mesoporous silica nanoparticles (SBA-15) the size was 3521 nm with a PDI value of 1 (Figure 2.6). The zeta potential value was -18.23 mV (Figure 2.6).

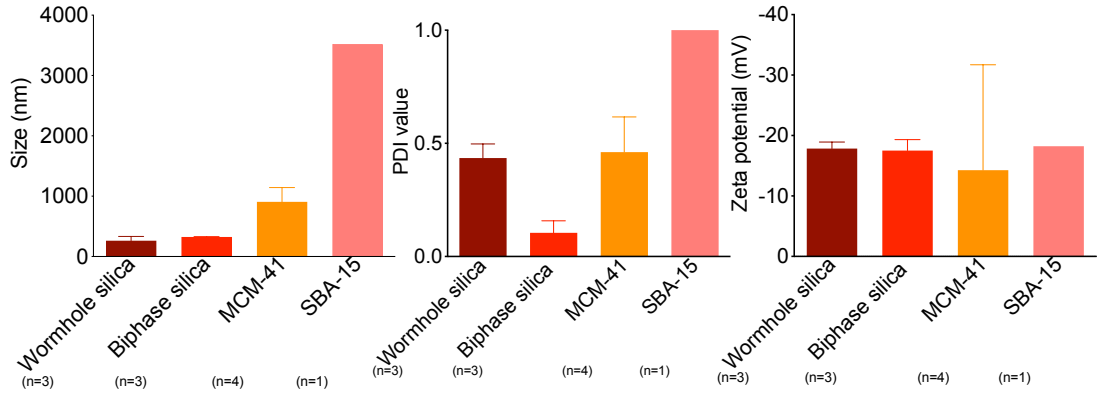

Figure 2.6 Porous silica nanoparticle format. Wormhole, biphase, MCM-41, and SBA-15 format. Data are presented as mean ± SD.

2.4.2 Chemical structure of silica nanoparticles

The FTIR results from nonporous silica nanoparticles including Stober silica nanoparticles produced using condition1 (Figure 2.7). Stober silica nanoparticles Condition 1 with a decreased volume of NH_4OH (Figure 2.8) and porous nanoparticles showed the characteristics absorption peak between 1065.64 – 1015.71 cm^{-1} (Figure 2.9). This peak was assigned to Si-O-Si asymmetric stretching vibration. However, the intensity of the peak for

wormhole and MCM-41 silica was substantially lower than biphase and Stober silica due to the smaller presence of oxygen in the sample. The peaks at 948.66 – 925.83 cm^{-1} were indicated to Si-OH asymmetric stretching vibration.

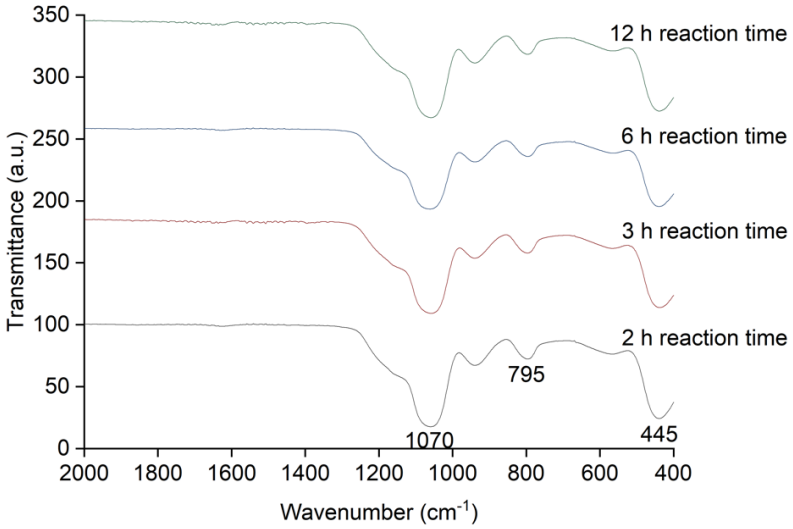

Figure 2.7 Fourier transformed infrared (FTIR) spectra and peak assignment of Stober silica nanoparticles produced using Condition 1 with a 12 h, 6 h, 3 h and 2 h reaction time.

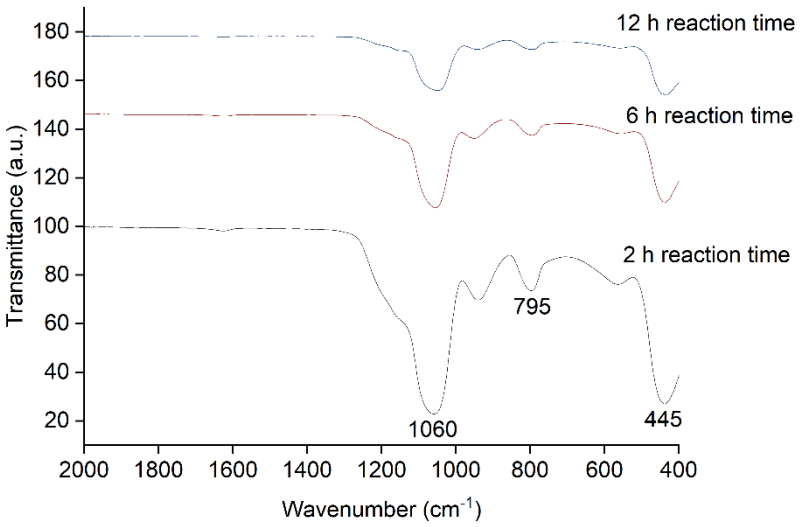

Figure 2.8 Fourier transformed infrared (FTIR) spectra and peak assignment of Stober silica produced using Condition 4 after 12 h reaction time, 6 h and 2 h reaction time.

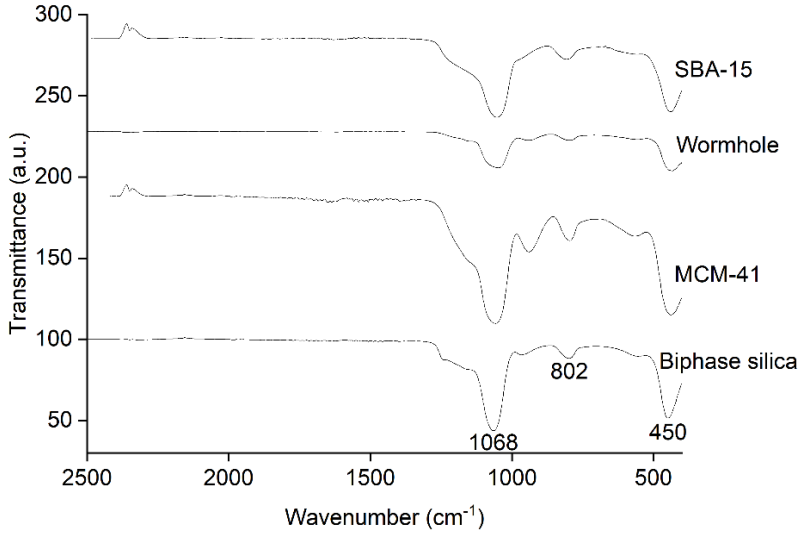

Figure 2.9 Fourier transformed infrared (FTIR) spectra and peak assignment of porous silica nanoparticles including SBA-15, wormhole, MCM-41, and Biphase silica nanoparticles.

2.4.3 The silica nanoparticle morphology

SEM images of non-porous and porous silica nanoparticles showed that the Stober silica had a spherical shape (Figure 2.10). For the Stober silica method Condition 1 with reduced NH_4OH volume, the resulting particles had a smaller size (96 -120 nm) than those synthesised using the original method (particle size 248 – 302 nm). In contrast, the SBA-15 particles aggregated to form a rod-like shape. The MCM-41 particles aggregated to form an amorphous shape (Figure 2.11).

Nonporous silica nanoparticles

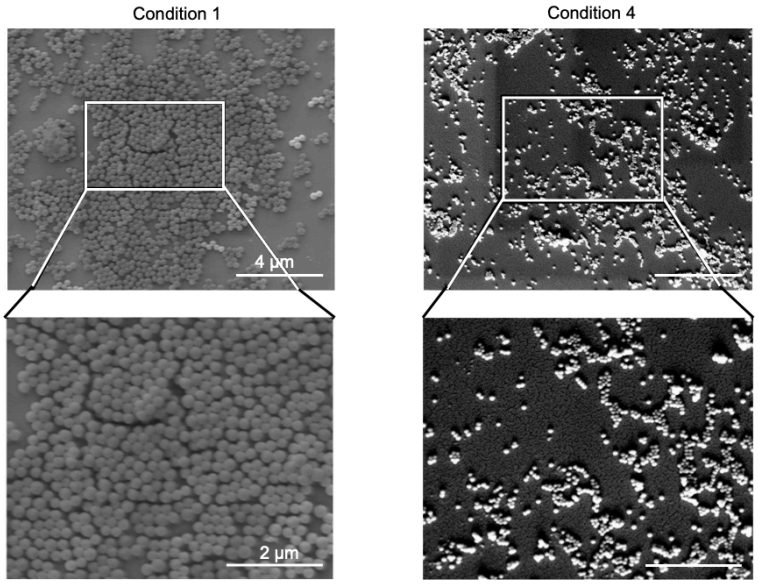

Figure 2.10 Scanning electron microscopic images (scale bar, 4 µm; zoom, 2 µm) of silica nanospheres using the Stober method.

Porous silica nanoparticles

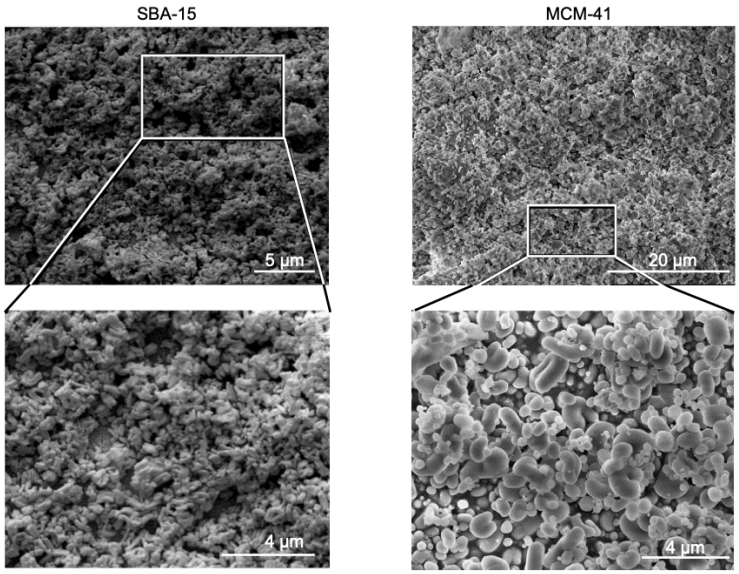

Figure 2.11 Scanning electron microscopic images of porous silica nanoparticles commercial porous silica nanoparticles (SBA-15) (scale bar, 5 µm; zoom, 4 µm) and MCM-41 (scale bar, 20 µm; zoom, 4 µm).

2.4.4 The pore volume and surface area of silica nanoparticles

The pore volume and surface area of particles were determined using nitrogen adsorption. The results showed the nitrogen adsorption-desorption isotherm of MCM-41 (Figure 2.12) and SBA-15 (Figure 2.12). From the Brunauer–Emmett–Teller (BET) and Barrett-Joyner-Halenda (BJH) measurement, the surface area of MCM-41 was determined to be 1.69 m^2/g with pore volume 0.00 cm^3/g while SBA-15 had a porosity of 0.49 m^2/g with pore volume 0.00 cm^3/g. The pore size of particles was calculated using the pore radius from the BJH method (Barrett et al., 1951). The SBA-15 and MCM-41 had pore radius (r) of 32.72 Å (3.27 nm) and 17.05 Å (1.70 nm), respectively. The Stober silica was classified as a type II isotherm (Figure 2.12). This indicated that Stober silica was non-porous. Stober silica presented a hysteresis loop which was classified to be an H1 type in the range between 0.90 to 1 relative pressure. The hysteresis loop was indicative of nanoparticle aggregation. From the BET and BJH measurements, the

surface area of Stober silica was determined to be 20.25 m^2/g with a pore volume of 0.35 cc/g.

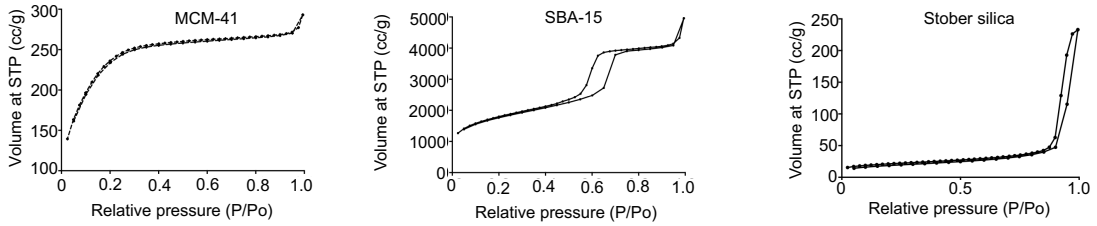

Figure 2.12 Nitrogen adsorption and desorption isotherms of porous silica and non-porous nanoparticles including MCM-41, SBA-15, and Stober silica.

2.4.5 The rheology of silk hydrogels in the presence and absence of non-porous silica nanoparticles

The stiffness of 3% w/v silk hydrogels was compared with those silk hydrogels that contained silica particles manufactured using Doping Methods 1 and 2. The stiffness of silk hydrogels containing silica particles derived using Doping Method 1 was 2.25 kPa. This value was higher than silk hydrogels containing either Doping Method 2 Stober silica (2.10 kPa) or SBA-15 1.88 kPa (Figures 2.13 and 2.14A). For Doping Method 1 (Table 2.1), when the concentration of Stober silica nanoparticle content was increased to 5%, the stiffness of the hydrogel was 2.82 kPa. This value was the highest measured, followed by hydrogels containing 0.10 % w/v Stober silica (2.31 kPa). The stiffness was the lowest for a 5% w/v SBA-15 concentration (2.10 kPa) while silk hydrogels with 0.10% w/v SBA-15 had a stiffness of 2.19 kPa (Figure 2.13). Doping Method 2 using SBA-15 showed that the stiffness of the hydrogel containing 5% w/w SBA-15 was 2.11 kPa and thus substantially greater than hydrogels containing 0.10 % w/v SBA-15 (1.48 kPa). Similar results were observed for Stober silica where 0.10% w/w and 5% w/w resulted in 2.05 kPa and 2.14 kPa stiffnesses, respectively (Figure 2.14A and Table 2.2).

The half stress-relaxation time histogram and table content (Figure 2.15 and Table 2.3) showed the same trend between silk hydrogels with SBA-15 and

Stober silica. The half stress-relaxation time of silk hydrogels with 5% w/v of SBA-15 (210.90 s) and Stober silica (244.90 s) was higher than either 0.10% w/v of SBA-15 (84.99 s) or Stober silica nanoparticles (228.10 s) (Figure 2.15).

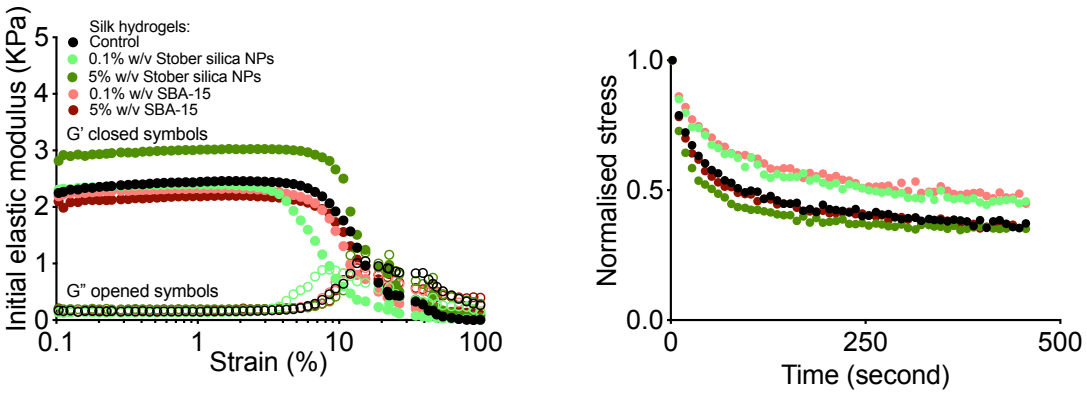

Figure 2.13 Impact of Doping Method 1 on silk hydrogel rheological properties. Rheological properties of viscoelastic 3% silk hydrogels with non-porous silica nanoparticles and SBA-15 (porous silica nanoparticles) at a concentration of 0.10% w/v and 5% w/v of nanoparticles. This figure shows strain sweep, storage modulus (G'), and loss modulus (G") curves (n=1 independent experiment).

Table 2.1 Impact of Doping Method 1 on silk hydrogel rheological properties of silk hydrogels with non-porous silica nanoparticles and SBA-15 (porous silica nanoparticles) at a concentration of 0.10% w/v and 5% w/v of nanoparticles including initial elastic modulus (stiffness) and half-stress relaxation time. Data are presented as mean ± SD, n = 1 independent experiments.

Samples	**Initial elastic modulus (kPa)**
Silk hydrogel (control)	2.25
Silk hydrogel + 0.1% w/v Stober silica nanoparticles	2.31
Silk hydrogel + 5% w/v Stober silica nanoparticles	2.82
Silk hydrogel + 0.1% w/v SBA-15 nanoparticles	2.19
Silk hydrogel + 5% w/v SBA-15 nanoparticles	2.10

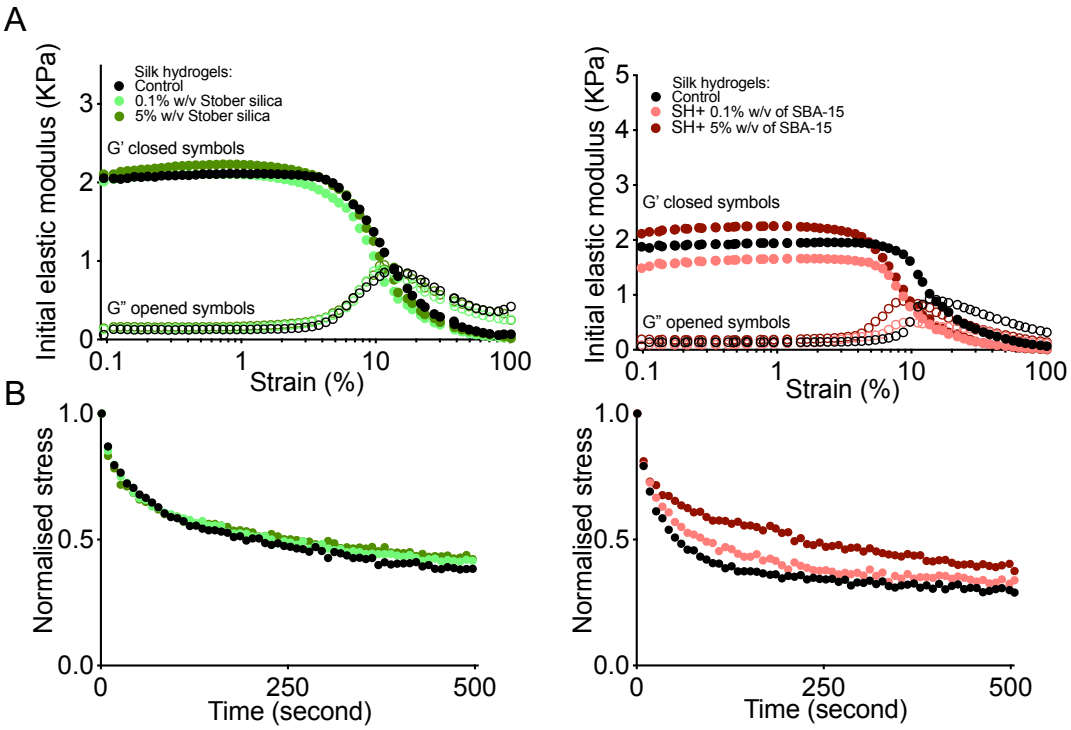

Figure 2.14 Impact of Doping Method 2 on silk hydrogel rheological properties. (A) stiffness and (B) stress relaxation time of viscoelastic 3% silk hydrogels with non-porous silica nanoparticles and SBA-15 prepared according to Doping Method 2 with different amounts of particles (n=1 independent experiments).

Table 2.2 Impact of Doping Method 2 on silk hydrogel rheological properties of silk hydrogels with non-porous silica nanoparticles and SBA-15 (porous silica nanoparticles) at a concentration of 0.10% w/v and 5% w/v of nanoparticles including initial elastic modulus (stiffness) and half-stress relaxation time. Data are presented as mean ± SD, n = 1 independent experiments.

Samples	**Initial elastic modulus (kPa)**
Silk hydrogel (control for Stober silica)	2.06
Silk hydrogel + 0.1% w/v Stober silica nanoparticles	2.01
Silk hydrogel + 5% w/v Stober silica nanoparticles	2.10
Silk hydrogel (control for SBA-15)	1.88
Silk hydrogel + 0.1% w/v SBA-15 nanoparticles	1.49
Silk hydrogel + 5% w/v SBA-15 nanoparticles	2.11

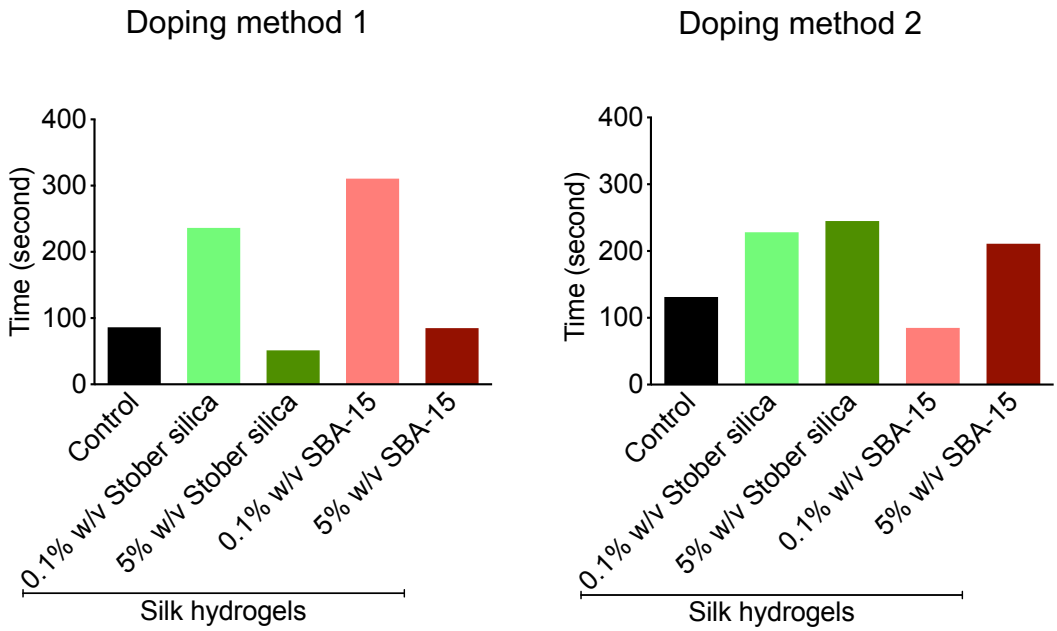

Figure 2.15 Impact of particles on viscoelastic properties of silk hydrogels manufactured using Doping Methods 1 and 2. Half-stress relaxation time of 3% silk hydrogels with and without silica nanoparticles (n=1 independent experiment).

Table 2.3 Impact of particles on viscoelastic properties of silk hydrogels manufactured using Doping Methods 1 and 2. Half-stress relaxation time of 3% silk hydrogels with and without silica nanoparticles (n=1 independent experiment).

Samples	**Half-stress relaxation time (second)**	
Method	**Doping 1**	**Doping 2**
Silk hydrogel (control for Stober silica)	2.25	Stober: 2.10 SBA-15: 1.88
Silk hydrogel + 0.1% w/v Stober silica nanoparticles	2.31	2.01
Silk hydrogel + 5% w/v Stober silica nanoparticles	2.82	2.10
Silk hydrogel + 0.1% w/v SBA-15 nanoparticles	2.19	1.49
Silk hydrogel + 5% w/v SBA-15 nanoparticles	2.10	2.11

2.4.6 The secondary structure of 3% w/v silk hydrogels

FTIR result showed an amide I absorption peak at 1600-1700 cm^{-1} for all silk samples (Figure 2.16). The 3% w/v silk hydrogels were compared to air-dried silk film (negative control) and silk films treated with 70% v/v ethanol/distilled water (positive control). Spectra of silk hydrogels and the comparable secondary structure graph showed that the silk films treated with 70% v/v ethanol/distilled water had the highest β-sheets content (32.11%). The β-sheets content of 3% w/v hydrogel was 31.92% which is higher than the β-sheets content of 3% w/v silk film (negative control) (22.86%). Additionally, the α-helix and random coil content (38.09%) of silk hydrogels was compared with negative (37.67%) and positive silk film (19.92%).

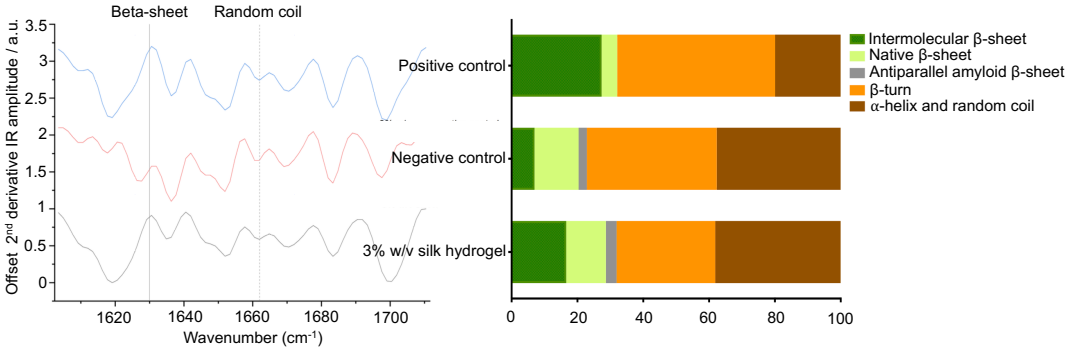

Figure 2.16 FTIR spectra and peak assignment of 3% silk hydrogels, air-dried film, and 70% ethanol-treated silk film, and comparable secondary structure.

2.5 DISCUSSION

Tissue engineering principles are not only relevant in health but also when designing *in vitro* disease models (Tandon et al., 2020). One key requirement is to create a cell microenvironment that supports tissue development; biomaterials are critical enablers. One emerging material is silk. Silk fibroin is well placed to develop disease models due to silk's mechanical properties, biocompatibility, water, and oxygen permeability (Qi et al., 2017). Importantly, silk hydrogels do not shrink *in vitro* over time (a common problem when working with collagen). Self-assembled silk hydrogels are particularly interesting because they show viscoelastic material properties (Phuagkhaopong et al., 2021) resembling native extracellular matrix and their mechanics can be tuned by increasing the silk content. For example, Liu et al. fabricated silk hydrogels reinforced with fibroin nanofibres to enhance their mechanical properties. This reinforcement strategy enhanced the stiffness of the silk fibroin hydrogel (from 0.60 to 16 kPa) (Liu et al., 2019). One limitation when working with *B. mori* silk fibroin is the lack of the arginine-glycine-aspartic acid (RGD) sequence necessary for integrin-mediated cell adhesion (Holland et al., 2019). Therefore, *B. mori* silk hydrogels could be viewed as a 'blank slate' that requires modification to maximise their potential. While *B. mori* silk lacks the RGD sequence Tasar silk contains the RGD sequence (see Chapter 3)

Wen et al. reported that nanoparticles within the 2 to 200 nm size range altered cell signalling and biology (Jiang et al., 2008). Therefore, the aim was to synthesize porous and non-porous silica nanoparticles of 100-150 nm. The non-porous silica nanoparticles were synthesised using the Stober method (Khanna et al., 2018a) but separated into three conditions. These Stober silica nanoparticles were characterised according to their size and zeta potential using dynamic light scattering (DLS). Stober silica particles synthesised with Condition 2 (reduce the volume of ethanol) were the largest, with a similar yield as those manufactured using Condition 3 (reduce tetraethyl orthosilicate volume) or 1 (Figure 2.2). Decreasing the volume of ethanol increased silica nanoparticle size; an observation consistent with earlier work (Qiao et al., 2009). The target particle size of the synthesis was 150 nm. However, Stober condition 1 produced 105 ± 1.47 nm sized particles (Figure 2.2). Therefore, the Stober condition1 was modified by decreasing reaction time (from 12 h down to 2 h) (Figure 2.3). However, the resulting silica particles were in the 200 nm size range. Others (Greasley et al., 2016) report that the NH_4OH concentration influenced particle size, with increased ammonium hydroxide concentration increasing particle size. Therefore, the volume of NH_4OH was reduced from 3.00 mL to 1.50 mL in three different reaction times (Figure 2.4). The results showed that the particle size was near 150 nm after a 6 h reaction time. One challenge encountered was that the particle size changed over time due to particle sedimentation. Nevertheless, the findings indicated that the size and PDI of Stober silica nanoparticles, synthesised under condition 4 with a 6-hour reaction time, remained unchanged throughout a 90-minute period (Figure 2.5).

Mesoporous silica nanoparticles were synthesised using three methods: biphase, wormhole, and MCM-41 silica nanoparticles synthesis. These particles were compared to commercial silica nanoparticles (SBA-15) (Figure 2.6). The size of biphase silica nanoparticles was 324.9 ± 4.62 nm (Figure 2.6) which was consistent with previous work and showed that the thickness of each generation could be tuned from ~5 to 180 nm (Shen et al., 2014). The wormhole particles were produced with a size of 202.40 ± 69.84 nm (Figure

2.6); this was substantially larger than the previously reported 60 to 70 nm particles (Möller et al., 2007). Similarly, the MCM-41 silica nanoparticles were larger (906 ± 236.50 nm) (Figure 2.6) than previously reported (100 ± 30 nm) (Costa et al., 2020). The particle size of commercial mesoporous silica nanoparticles (SBA-15) was 3521 nm, which was the highest among the others (Figure 2.6). One possibility for this large particle size could be particle agglomeration.

Fourier-transform infrared spectroscopy (FTIR) was used to determine different functional groups present at the SiO_2 particle surface. Both porous and non-porous silica nanoparticles showed a typical absorption peak of Si-O-Si (1065.64 – 1015.71 cm^{-1}) and Si-OH asymmetric stretching vibration (948.66 – 925.83 cm^{-1}) (Figures 2.7,2.8, and 2.9). These results are consistent with previous reports (Launer and Arkles, 2013, Feifel and Lisdat, 2011). The morphology of Stober silica and SBA-15 were determined by scanning electron microscopy. Stober silica from condition 1 and condition 1 with a decrease in NH_4OH volume were spherical (Figure 2.10) and had an average size of 215 nm and 134 nm, respectively (Figure 2.10). These results were consistent with previous reports (Vittoni et al., 2019, Koo et al., 2012). However, SBA-15 particles had still formed a rod-like shape (Figure 2.11) which is consistent with previous work (Esperanza Adrover et al., 2020). The MCM-41 had an amorphous shape which is not consistent with (Costa et al., 2020).

The pore volume and surface area of particles were determined too using nitrogen adsorption. Previous reports show that MCM-41 silica nanoparticles were classified as type-IV isotherm (Nastase et al., 2014) demonstrating a fully reversible process over the relative pressure range of 0-0.45 P/Po but hysteresis at pressures higher than 0.45 due to mesopore filling by capillary condensation. However, here MCM-41 was classified as a type II isotherm (Figure 2.12) because the material was non-porous. The isotherm showed monolayer adsorption. The commercial SBA-15 was classified as a type IV isotherm (Figure 2.12) which indicated that the SBA-15 was mesoporous because the isotherm showed a narrow hysteresis loop in the capillary

condensation process, which is consistent with earlier work (Ma et al., 2015). For non-porous silica nanoparticles, the Stober silica was classified as a type II isotherm and was non-porous (Figure 2.12). I note that the isotherm graph showed a thin hysteresis loop which was classified to be an H1 type indicative of nanoparticle aggregation. The literature has reported a similar result (Vittoni et al., 2019).

Next, the impact of particles on hydrogel was analysed using rheology. The initial hypothesis for this measurement was that increasing particle concentration would result in a higher initial modulus (stiffness). Previous studies have indicated that adding silica to silk reinforcement increases bulk stiffness (Cheng et al., 2021). The viscoelastic behaviour of silk hydrogels in the presence of particles has not been previously reported. This report discovered that increasing particle concentration increased both initial modulus and stress relaxation time. (Figures 2.14 and 2.15). The secondary structure of 3% w/v silk hydrogel was determined by FTIR. The result showed extensive β-sheets in self-assembled silk hydrogel were consistent with the wider literature (Seib, 2018).

Silk hydrogel composite nanoparticles are to be used for cell culture to modulate cell attachment albeit none of these studies have been carried out to date. To initiate this work baseline cell growth on tissue culture-treated polystyrene was assessed demonstrating cell density-dependent growth (Figure 2.17).

2.6 Conclusion

Both silk hydrogel and silica nanoparticles were prepared (porous and non-porous). Silica nanoparticles were successfully synthesised and characterised using DLS, SEM, and nitrogen adsorption. For example, non-porous silica particles were 100 - 400 nm while porous silica nanoparticles were 200 - 900 nm. Next, pure *B. mori* silk hydrogels were formed by triggering silk self-assembly. These hydrogels had a high β-sheet content, an average elastic modulus of 2 kPa, and an average half-stress relaxation time of 150 s. Next,

the self-assembling silk hydrogel embedded SBA-15 (porous) and non-porous silica nanoparticles. For the silk hydrogel mechanical properties, silk hydrogel loaded with 500 mg/mL of silica nanoparticles promoted a higher stiffness of 2.11 kPa than a lower concentration of 0.10% w/v 1.48 kPa. In this chapter, the amount of Stober silica nanoparticles added was 0.1 and 5% w/v. However, in Chapter 3 the amount of Stober silica nanoparticle was further refined using 0.05 and 0.50% w/v.

Chapter 3

Functionalizing Silk Hydrogels with Hetero- and Homotypic Nanoparticles

Chapter summary:

This chapter examined the impact of low (0.05% w/v) and high (0.5% w/v) non-porous silica, *B. mori* and Tasar silk nanoparticles on the mechanical properties of silk hydrogel. Next, DU-145 (prostate cancer cell line) were cultured on silk hydrogel composite on to investigate the impact to cell adhesion.

This chapter has been submitted for publication. I designed, collected, analysed and interpreted the data and generated the manuscript draft. Suttinee Phuagkhaopong generated Tasar silk nanoparticle protocol. Saphia Matthew supported the FTIR analyses.

3.1 Abstract

Despite many reports detailing silk hydrogels, the development of composite silk hydrogels with homotypic and heterotypic silk nanoparticles and their impact on material mechanics and biology have remained largely unexplored. I hypothesised that the inclusion of nanoparticles into silk-based hydrogels would enable the formation of homotropic and heterotropic material assemblies. The aim was to explore how well these systems would allow tuning of mechanics and cell adhesion to ultimately control the cell–material interface. I utilised nonporous silica nanoparticles as a standard reference and compared them to nanoparticles derived from *B. mori* silk and *A. mylitta* (Tasar) silk (approximately 100–150 nm in size). Initially, physically cross-linked *B. mori* silk hydrogels were prepared containing silica, *B. mori* silk nanoparticles, or Tasar silk nanoparticles at concentrations of either 0.05% or 0.5% (w/v). The initial modulus (stiffness) of these nanoparticles–functionalised silk hydrogels was similar. Stress relaxation was substantially faster for nanoparticle-modified silk hydrogels than for unmodified control hydrogels, although this process could be modulated. Increasing the

concentrations of *B. mori* silk and silica nanoparticles slowed stress relaxation, while the opposite trend was observed for hydrogels modified with Tasar nanoparticles. Cell attachment was similar for all hydrogels, but proliferation during the initial 24 h was significantly improved with the nanoparticle-modified hydrogels. Overall, this study demonstrates the manufacture and utilisation of homotropic and heterotropic silk hydrogels.

3.2 Introduction

The tissue engineering toolbox traditionally serves to 'repair or replace' (Langer and Vacanti, 1993), but it can also be deployed more widely—in disease modelling, for example (Abbott et al., 2016, Tandon et al., 2020). A key factor in tissue engineering is the cell microenvironment, as this ultimately contributes to the function (Gattazzo et al., 2014). This microenvironment potentially includes many different cell types and biomaterials that serve as tissue scaffolds (Sanchez-Rubio et al., 2023). These scaffolds not only provide structural support but can also regulate function, including cell–cell communication, tissue homeostasis and immune cell responses (reviewed in (Li et al., 2017, Sanchez-Rubio et al., 2023)). Therefore, biomaterials are critical enablers of a broad spectrum of tissue engineering applications in both health and disease.

A fundamental requirement for a biomaterial is that it supports the desired function, such as cellular organisation. To date, many different biomaterials have been explored (Kirillova et al., 2021), including synthetic polymers (e.g. polylactide (Deoray and Kandasubramanian, 2018) and polyethylene glycol (Xiao et al., 2022)) and natural polymers (e.g. chitosan (Rezaei et al., 2021), collagen (Dong and Lv, 2016) and alginate (Lee and Mooney, 2012)). However, all of these polymers have drawbacks, including rapid degradation, shrinkage (e.g. collagen), low mechanical strength (e.g. collagen, alginate), complicated processing (e.g. polyethylene glycol or alginate), biocompatibility concerns (e.g. leaching of chemical crosslinkers) and perturbation of the microenvironment (e.g. polylactide degradation causes acidification). Silk

fibroin is emerging as an interesting material that shows promise for overcoming these particular limitations (Seib, 2018). Chemical modification of silk further opens up new properties to create bespoke materials with novel functions (Matthew and Seib, 2023).

Silk is a natural fibrous protein spun by spiders and insects (e.g. Lepidoptera). Silk self-assembles into a hierarchal solid fibre during the spinning process by responding to processing parameters, including shear (Seib, 2021). The most studied silk for current biomedical applications is derived from the domesticated silkworm *B. mori* because its silk is clinically approved for use in humans and is readily available in large quantities due to silk farming (i.e. sericulture), thereby ensuring a robust silk supply chain (Holland et al., 2019). Silk's desirable trademarks include its remarkable mechanical properties, biocompatibility, biodegradability, hemocompatibility and water and oxygen permeability (Bucciarelli and Motta, 2022, Holland et al., 2019). Using all-aqueous processing, the silk fibre can be unspun using reverse engineering principles to yield a liquid regenerated silk feedstock (reviewed in (Rockwood et al., 2011)). This liquid silk can then be processed into a wide range of material formats, including films, monolithic blocks, fibres, particles, scaffolds and hydrogels (Qi et al., 2017), again using all-aqueous processing without any need for chemical crosslinkers or harsh solvents.

The *B. mori* silk fibroin consists of a heavy chain of approximately 391 kDa and a light chain of approximately 26 kDa, which are linked by a single disulphide bond at the C-terminus (Zhou et al., 2001). The C- and N-termini of the *B. mori* silk heavy chain consist entirely of nonrepeating amino acid sequences and are believed to aid in the storage and self-assembly process. However, the mechanical properties of silk fibroin arise from the amino acid sequences of the silk-heavy chain that assemble into beta sheets. The copolymer-like arrangement of the silk-heavy chain contains two main motifs, namely, repetitive hydrophilic amino acid sequences and hydrophobic stretches, which result in a copolymer-like arrangement containing 11

hydrophilic and 12 hydrophobic blocks (Asakura et al., 2015). The hydrophobic region is dominated by glycine-X repeats, where X is alanine, serine, or tyrosine. *B. mori* silk fibroin lacks the tripeptide sequence arginine, glycine and glutamic acid (RGD) that is typically exploited by cells to mediate cell–substrate attachment via integrin engagement. Instead, the N terminal of the silk-heavy chain contains a fibroblast growth-promoting peptide (Yamada et al., 2004).

Lepidoptera silks share several structural features, including light and heavy chains, with conservation of the positions and spacing of cysteine residues that covalently crosslink the light and heavy chains. These silks also have an amphiphilic structure. Nevertheless, sequence specificity exists between different silkworm silks; for example, the Indian non-mulberry Tasar silkworm (*A. mylitta*) contains RGD sequences that are absent in *B. mori* silk, while the silk from *Antheraea assama* (golden silk) has substantial polyalanine stretches that are associated with better mechanics and thermal stability than is observed with *B. mori* silk (Malay et al., 2016). Therefore, possibilities exist for the creation of new materials with desired properties by blending different liquid silk types. For example, blending *A. assama* with *B. mori* liquid silks triggered the solution–gel transition within 40 min of mixing. These hydrogels were physically crosslinked via their beta sheets and showed promising *in vivo* wound-healing properties (Holland et al., 2019).

This thesis exploits silk self-assembly using sonication as a solution–gel transition trigger (Seib, 2018). This assembly strategy has been widely used in the past because the process is simple and eliminates the need for solvents or chemical crosslinkers. Examples where these silk hydrogels have been used include soft (Abbott et al., 2016) and hard (Zhang et al., 2021b) tissue engineering (e.g. tissue fillers, bone engineering). For example, silk hydrogels modified with several nanoparticle types, such as triphasic ceramic (Mg_2SIO_4, Si_3Sr_5, and MgO) (Roohaniesfahani et al., 2019), silica (Cheng et al., 2021), iron, silver and gold nanoparticles (Belda Marin et al., 2021, Ribeiro et al.,

2017), have shown promise for a spectrum of applications, including magnetic field actuation (Qian et al., 2020), antibacterial functions (Ribeiro et al., 2017) and bone tissue engineering (Cheng et al., 2021, Roohaniesfahani et al., 2019). Physically crosslinked silk hydrogels reinforced with native-like *B. mori* fibres (Yodmuang et al., 2015) and chemically crosslinked silk hydrogels doped with amorphous silk fibroin nanofibres (Liu et al., 2019) have also been reported, demonstrating the possibility of tuning the silk secondary structure and fibre format. Unmodified (Seib et al., 2013) and nanoparticle-modified silk hydrogels (Numata et al., 2012) have also been explored for drug delivery. For example, Keiji Numata and co-workers developed the first-generation *B. mori* drug release system that incorporated silk nanoparticles within physically crosslinked silk hydrogels (Numata et al., 2012), while others have advanced this concept further and used these systems to release multiple drugs *in vivo* (Wu et al., 2018). An emerging research avenue is to use silk hydrogels as an *in vitro* tissue model that includes the tumour microenvironment (Ribeiro et al., 2018).

Previous studies have used silk fibroin hydrogels to assess their baseline performance as a tumour microenvironment, including the capacity to support cell migration (Carvalho et al., 2018, Khoo et al., 2019). The ultimate goal of these studies is to recapitulate specific biological processes and behaviours that are dictated by the material design (Blatchley and Anseth, 2023). Important factors to consider when designing these living tissue systems are the elastic and viscoelastic moduli of the extracellular mimetic matrix (Chaudhuri et al., 2020). For example, during solid tumour progression, the mechanical properties of the extracellular matrix change (thereby assisting disease diagnosis of solid tumours, for example). In the context of solid tumours, the substrate stiffness is accompanied by changes in flow characteristics (i.e. stress relaxation). Therefore, when developing extracellular matrix models, hydrogel performance is often assessed against cell function (e.g. cell migration, differentiation, proliferation etc.). Physically crosslinked silk hydrogels can mimic the three-dimensional structure of native

extracellular matrix (Seib, 2018). For example, self-assembled silk hydrogels with a solid silk content of 4% w/v show viscoelasticity, which in turn impacts cell biology (Phuagkhaopong et al., 2021).

Despite many reports detailing silk hydrogels, the development of composite silk hydrogels containing homotypic and heterotypic silk nanoparticles and their impact on material mechanics and biology, has remained largely unexplored. A caveat when working with *B. mori* hydrogels is the lack of arginine-glycine-aspartic acid (RGD) sequences in this silk, as these sequences are necessary for integrin-mediated cell adhesion (Holland et al., 2019). For this reason, silks from non-mulberry Tasar silkworms (e.g., *A. mylitta*) are more promising because they contain the RGD sequence. However, how well these silks allow tuning of the mechanics and cell adhesion that ultimately control the cell-material interface is unknown. Therefore, the aim of this Chapter was to create hydrogels functionalised with nanoparticles derived from blends of *B. mori* and Tasar silk to probe cell responses and to compare them to hydrogels prepared using silica nanoparticles as a reference. This Chapter reports the manufacture of nonporous Stober silica, *B. mori* and Tasar silk nanoparticles and their addition at low (0.05% w/v) and high (0.5% w/v) concentrations to 3% w/v *B. mori* silk undergoing solution-gel transition. The resulting nanoparticle-functionalised silk hydrogels had similar stiffnesses but exhibited substantial differences in stress relaxation when compared to unmodified control hydrogels. Cell attachment was similar for all the tested hydrogels.

3.3 Materials and Methods

3.3.1 Silk extraction

The silk fibroin solution was prepared as previously reported in Chapter 2.

A. mylitta silkworm cocoons were prepared based on previous work by others (Kundu et al., 2014). Briefly, dried cocoons were cut into 5 × 5 mm pieces and 5 g samples were degummed with 2 L of 0.025 M Na_2CO_3 for 60 min, followed

by 60 min in 2 L of 0.0125 mM Na_2CO_3. The silk fibres were then washed three times with 1 L of distilled water for 20 min and then dried in a fume hood overnight. The dried silk fibroin was dissolved in 1 N NaOH at a silk to NaOH ratio of 1 g to 25 mL. The samples were kept at 25℃ for up to 16 h under constant stirring at 250 rpm. Insoluble material was removed by centrifugation for 20 min at 9500 × g. The supernatant was transferred to a dialysis cassette (molecular weight cut-off 3,500 Da; Thermo Fisher Scientific Inc., Waltham, MA, USA) and dialysed against distilled water, with four water changes over the 24 h dialysis period. The dialysed silk fibroin solution was collected and centrifuged twice at 9500 × g for 20 min to remove any remaining aggregates. Samples were freeze dried and reconstituted to 4 % (w/v) and stored at 4℃ until use. The Tasar silk fibroin concentration was calculated using the bicinchoninic acid assay protein assay and bovine serum albumin as a protein standard (Pierce™ BCA Protein Assay Kit, Thermo Fischer Scientific).

3.3.2 Particle synthesis & characterisation

3.3.2.1 Particles synthesis

The non-porous silica nanoparticles Condition 4 were prepared as previously reported in Chapter 2.

B. mori silk nanoparticles were manufactured as described previously (Matthew et al., 2020). Briefly, silk nanoparticles were generated using semi-automated nanoprecipitation by controlling the silk and solvent flow with a syringe pump (Harvard Apparatus 22, Holliston, MA) (Figure 3.1). The system was equipped with a syringe and blunt needle (23G × 0.25″) and operated at room temperature. Isopropanol was contained in a short-neck round-bottom flask and the ratio of isopropanol to silk was set at 5:1 (v/v). A 3% (w/v) *B. mori* silk solution was added dropwise at a rate of 1 mL min^{-1}. The resulting suspension was transferred to polypropylene ultracentrifugation tubes, the volume was made up to 43 mL with distilled water and the tubes were centrifuged at 48,400 g for 2 h at 4 °C (Beckmann Coulter Avanti J-E equipped with a JA-20 rotor). The supernatant was discarded, and the pellet

was resuspended in 20 mL distilled water and sonicated twice for 30 s at 30% amplitude with a Sonoplus HD 2070 sonicator (ultrasonic homogeniser, Bandelin, Berlin, Germany) fitted with a 23 cm long sonication tip (0.3 cm diameter tip and tapered over 8 cm). Next, 23 mL of distilled water was added, and the sonicated material was centrifuged. This washing and resuspension of the pellet was repeated twice. The final pellet was collected and resuspended in 2−3 mL water. This final silk nanoparticle suspension was stored at 4 °C until use.

Tasar silk nanoparticles were synthesised using a NanoAssemblr microfluidic system (NanoAssemblrTM Benchtop Instrument version 1.5, Canada). Prefilled syringes containing 2% (w/v) silk solution and acetone were dispensed into a microfluidic cartridge and mixed at a 1:4 ratio (v/v) of silk solution to acetone at a total flow rate of 1 mL/min (Figure 3.1). The precipitated silk nanoparticles were collected and centrifuged at 48,400 × g for 2 h, the supernatant was aspirated, and the pellet was resuspended in distilled water, vortexed and subsequently sonicated twice for 30 s sonication cycles at a 30% amplitude. The washing steps were repeated at least twice more. The silk particles were then stored at 4 °C until use.

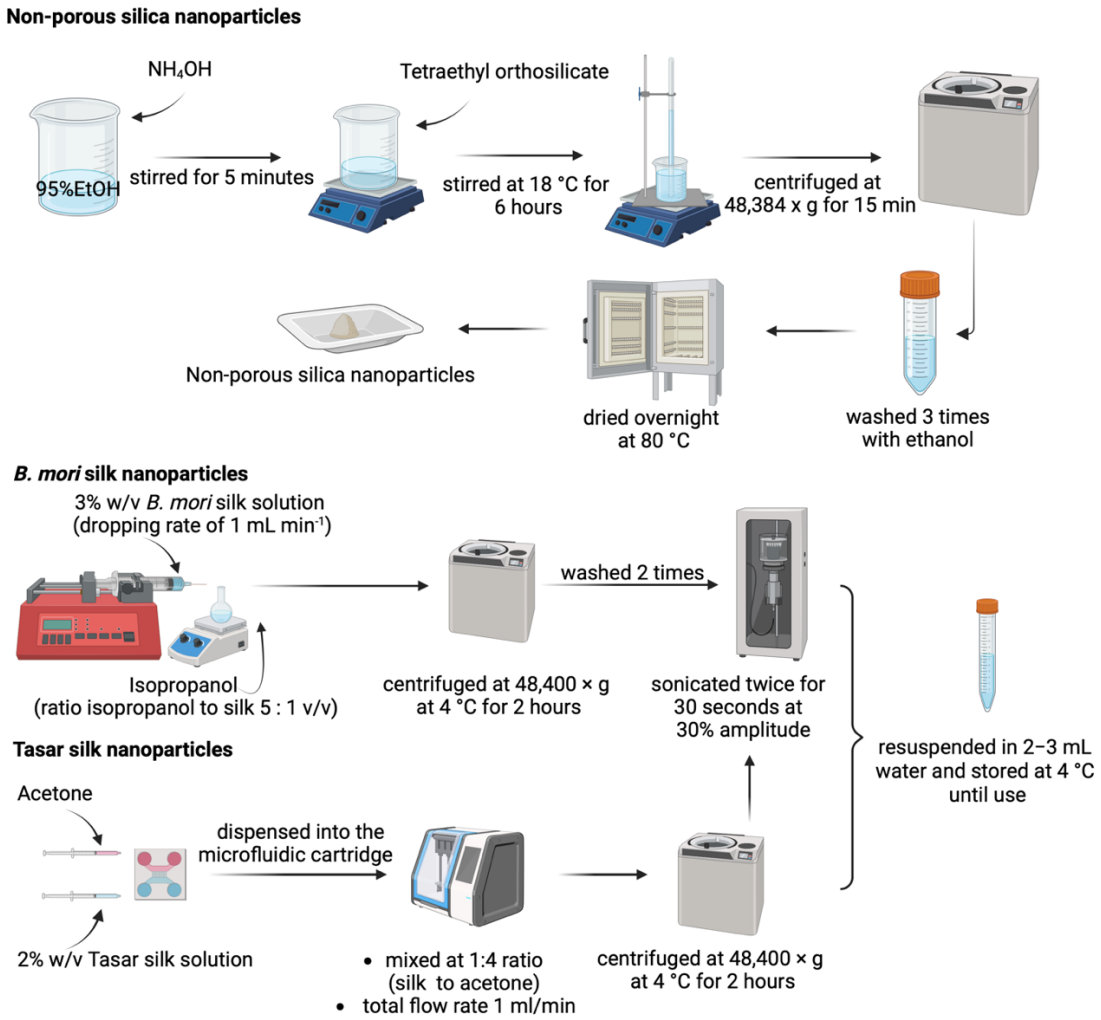

Figure 3.1 Flow diagram of nanoparticle manufacture. Silica, *B. mori* and Tasar silk nanoparticle synthesis.

3.3.2.2 Particle characterisation

3.3.2.2.1 Size and zeta potential

The particle diameters and surface charges of silica and silk nanoparticles were determined as detailed previously (Maitz et al., 2017). (M. F. Maitz et al., 2017; Wongpinyochit et al., 2016a Briefly, silica nanoparticles were suspended in distilled water at 1 mg/mL, vortexed for 10 min and sonicated for 30 s, while silk nanoparticles were vortexed for 20 s and sonicated twice at 30% amplitude for 30 s. The nanoparticle sizes were measured using a Zetasizer Nano ZS (Malvern Instruments, UK) at 25 °C. Particle sizes were determined using dynamic light scattering with a refractive index of 1.33 and 1.43 for distilled water and silica, respectively. The protein refractive index of

1.60 was used for silk nanoparticles. All measurements were performed in triplicate.

3.3.2.2.2 Pore volume and surface area of nanoparticles

The surface areas and pore sizes of the silica and silk nanoparticles were determined based on previous methodology (Jaroniec et al., 1999, Mitropoulos et al., 2019). Nanoparticles were characterised by nitrogen adsorption at 77 K using a Quantachrome Autosorb IQ2 analyser (Quantachrome Instruments, Boynton Beach, Florida, USA). First, 200 mg of silica nanoparticles were degassed under vacuum at 200 °C for 18 h and 100 mg of silk nanoparticles were degassed under vacuum at 100 °C for 10 h. (All samples were outgassed at room temperature.) The samples were analysed using the ASiQwin software Model 6 version 3.0-3.01. Particle surface areas were determined using the Brunauer-Emmett-Teller (BET) method and the pore volume was determined using the Barrett-Joyner-Halenda (BJH) method (Jaroniec et al., 1999).

3.3.2.2.3 Scanning electron microscopy (SEM) of nanoparticles

Nanoparticle suspensions were adjusted to a final concentration of 1 mg/mL, and 20 µL were pipetted onto a silicon wafer and lyophilised for 24 h at −10 °C and 0.14 mbar. The silica nanoparticles were sputter coated with 15 nm of gold using an ACE200 low-vacuum sputter-coated (Leica Microsystems, Wetzlar, Germany). Silicon wafers with nanoparticles were fixed to aluminium pin stubs with double-sided adhesive carbon tape. Specimens were imaged using the Quanta FEG-ESEM (FEI company, Hillsboro, OR, USA; now part of Thermo Fisher Scientific Inc., Waltham, MA, USA) with a 5 kV voltage at three magnifications (5,000×, 20,000×, and 40,000×). The images were processed using ImageJ for Windows 1.8.0.

3.3.3 Preparation of self-assembling silk hydrogels

The 3% w/v self-assembling silk hydrogels were prepared as previously reported in Chapter 2.

3.3.4 Silk secondary conformation analysis by Fourier-transform infrared spectroscopy (FTIR)

The secondary structures of *B. mori* and Tasar silk nanoparticles and silk hydrogels were measured as detailed previously (Matthew et al., 2020). Briefly, silk nanoparticles and silk hydrogels were frozen overnight at -80 °C and lyophilised. The secondary silk structure was measured with a TENSOR II FTIR spectrometer (Bruker Optik GmbH, Ettlingen, Germany). The samples were scanned 32 times for background and 128 times for the samples at 4 cm^{-1} resolution over the wavenumber range of 400–4000 cm^{-1}. The secondary structures were assigned as detailed previously. Baseline and peak fits were corrected using OriginPro 2021 software. The amide I region (1595–1705 cm^{-1}) was identified and deconvoluted as follows: 1605−1615 cm^{-1} as side chain/aggregated strands, 1616−1637 cm^{-1} and 1697−1703 cm^{-1} as beta-sheet structure, 1638−1655 cm^{-1} as random coil structure, 1656−1662 cm^{-1} as alpha-helical bands and 1663−1696 cm^{-1} as beta-turns. Air-dried films were used as negative controls, and a 70% ethanol-treated silk film was used as a positive control.

3.3.5 Rheology of silk hydrogel composites

Rheology measurements were performed as detailed in Chapter 2.

3.3.6 Cell culture

The human prostate cancer DU145 cell line was purchased from the American Type Culture Collection (Manassas, VA, USA). Briefly, the cells were routinely cultured in tissue culture–treated polystyrene flasks in Roswell Park Memorial Institute (RPMI) 1640 medium, supplemented with 10% v/v foetal bovine serum, 50U/mL penicillin and 50 µg/mL streptomycin. Unless otherwise indicated, the cells were seeded at 5,000 cells/cm^2. The cells were cultured at 37°C in 95% relative humidity and 5% CO_2 and passaged using trypsin and standard protocols. For cultures using silk hydrogels, the substrates were prepared in 96-well plates as described previously (Phuagkhaopong et al., 2021).

3.3.6.1 Quantification of cell attachment

3.3.6.1.1 cell viability

Cell viability was measured at days 1 to 9. The 25 µL of resazurin was added (440 µM stock in PBS, Thermo Fisher Scientific). The cells were transferred to an incubator (humidified atmosphere of 5% CO_2 at 37 °C) for 4 h to allow resazurin metabolism. Then, 100 µL of the supernatant was transferred into a black 96-well plate (Sigma Aldrich). The fluorescence was measured with a fluorescence plate reader (POLARstar Omega BMG LABTECH GmbH, Ortenburg, Germany) using a 560 nm excitation and 590 nm emission filters with a fix photo multiplying tube (800). Blank hydrogels from the same time points were used as controls to subtract background fluorescence and the DU-145 cells treated without silk hydrogel were used as a positive control.

3.3.6.1.1 cell attachment

DNA quantification was used to determine cell numbers, as detailed previously (Phuagkhaopong et al., 2021). Briefly, the Quant-iTTM PicoGreen kit was used to measure the number of DU145 cells that had attached to the control and silk hydrogel substrates at 2, 4 and 24 h post-seeding. At the indicated time point, the culture medium was removed and replaced with 200 µL of PBS. The cells were incubated for 3 h in a humidified atmosphere of 5% CO_2 at 37 °C and then homogenised and digested at 60 °C for 16 h in 200 µL papain buffer (5 mg/mL papain, 2 mM cysteine, 50 mM sodium phosphate and 2 mM ethylenediaminetetraacetic acid at pH 6.5 in nuclease-free water). The papain-digested samples were collected and centrifuged for 5 min at 13,000 $\times$ g to eliminate cellular debris. The supernatants were collected and dDNA was quantified with the Quant-iTTM PicoGreen kit, following the manufacturer's protocol. Blank hydrogels from the same time points were used as controls to account for background fluorescence.

The 3-(4,5-dimetylthiazol-2-yl)-2,5-diphenyl-2H-tetrazolium bromide (MTT) assay is widely used for cell viability, proliferation, and cell toxicity. The deconversion of MTT to formazan can be used to infer to the number of cells.

In this study, I used the MTT assay to measure the number of DU-145 cells that attached on silk hydrogels with nanoparticles at 2, 4 and 24 h after seeding. First, 100 µL of the DU-145 cells suspension was added to silk hydrogel substrates and the supernatant was removed at 2h, 4h, and 24 h after post seeding. This supernatant was transferred to plasma relative humidity and 5% CO2 for 24 h. Next, 20 µL of the MTT solution was added and incubated for 3 to 4 h. The medium was removed and replaced with the 110 µL of dimethysulfoxide (DMSO) to dissolve the formazan and 100 µL of the supernatant was transferred into 96 well measuring plate and the absorbance was measured at 570 nm.

Statistical analyses

Data were plotted and analysed as detailed previously (Totten et al., 2017). Briefly, sample pairs were analysed by one-way ANOVA with Tukey's multiple comparison post hoc test (Prism 9.2.0; GraphPad Software Inc., San Diego, CA, USA). Asterisks were used to denote statistical significance, as follows: *P < 0.05, **P < 0.01, ***P < 0.001. All data were presented as mean values ± standard deviation (SD). The number of independent experiments (n) is noted in each figure legend.

3.4 Results & Discussion

Tissue engineering principles are not only relevant in health applications, but they are also important when designing *in vitro* disease models (Tandon et al., 2020, Abbott et al., 2016). One key requirement is to create a cell microenvironment that supports tissue development; therefore, biomaterials are critical enablers. One emerging material is silk, as silk fibroin is well-placed to develop disease models due to its tuneable mechanical properties and biocompatibility. Importantly, silk hydrogels do not shrink *in vitro* over time (a common problem when working with collagen (Abbott et al., 2016). Self-assembled silk hydrogels are particularly interesting because they show viscoelastic material properties that resemble those of native extracellular matrix and their mechanics can be tuned by increasing the silk content

(Phuagkhaopong et al., 2021). For example, Liu et al. fabricated silk hydrogels reinforced with fibroin nanofibres to enhance the mechanical properties and found that this reinforcement strategy enhanced the stiffness of the silk fibroin hydrogel (from 0.6 to 160 kPa) (Liu et al., 2019) .

One limitation when working with *B. mori* silk fibroin is its lack of the RGD sequence necessary for integrin-mediated cell adhesion (Holland et al., 2019). For this reason, *B. mori* silk hydrogels can be viewed as 'blank slates' that require modification to maximise their potential. Tasar silk does contain the RGD sequence, but no examples currently exist in the literature of *B. mori* hydrogels functionalised with Tasar silk nanoparticles. Therefore, the present work closes a critical knowledge gap.

The use of Tasar silk nanoparticles to functionalise *B. mori* silk hydrogels is ideal because it permits spatial control of RGD functionalisation. In the present work, nonporous silica nanoparticles synthesised using the Stober method (Khanna et al., 2018b) were used as a reference. The *B. mori* silk nanoparticles were manufactured using the Matthew semi-batch set-up (Matthew et al., 2020) and Tasar silk nanoparticles were synthesised using a microfluidic-assisted antisolvent precipitation (Subia et al., 2014). All three nanoparticle types were characterised according to their size, polydispersity index and zeta potential using dynamic light scattering and zeta potential measurements, as the aim was to work with particles that were of similar size and surface charge. I therefore tuned the silica particle size by adjusting the NH_4OH concentration (In Chapter 2), because increasing ammonium hydroxide concentration is known to increase the nanoparticle size (Greasley et al., 2016). Ultimately, all three nanoparticle types had a size range of 120 to 150 nm and a zeta potential of -35 mV. Specifically, *B. mori* silk nanoparticles had an average size of 117 ± 5.31 nm, a polydispersity index of 0.14 ± 0.02 and a zeta potential of -38.6 ± 2.23 mV (Figure 3.2A), the *A. mylitta* (Tasar) silk nanoparticles had an average size of 146 ± 8.64 nm, a polydispersity index of 0.34 ± 0.04 and zeta potential of -32.8 ± 2.64mV, and the silica nanoparticles had an average size of 122 ± 22.68 nm, a polydispersity index of 0.31 ± 0.17 and a zeta potential of -37.8 ± 2.98 mV

(Figure 3.2A). These silk nanoparticle results are consistent with previous work using *B. mori* (Matthew et al., 2020, Seib et al., 2013, Matthew et al., 2022) and Tasar (Subia et al., 2014) silk stocks.

The pore volumes and surface areas of the nanoparticles were determined using nitrogen adsorption. The single-point Brunauer-Emmett-Teller (BET) analysis showed that *B. mori* and Tasar silk nanoparticles had pore volumes of 0.023 and 0.094 cm^3/g, respectively. This pore volume determination may indicate a particle aggregation (Vittoni et al., 2019) because transmission electron microscopy studies have demonstrated that silk nanoparticles are solid (Matthew et al., 2020). The surface areas of the *B. mori* and Tasar silk nanoparticles were determined as 5.02 and 33.65 m^2/g, respectively (Figure 3.2B).

The silica nanoparticles were classified by a type II isotherm, indicating that they were nonporous, as would be expected for Stober silica nanoparticles (Vittoni et al., 2019) The presence of a hysteresis loop classified the material as an H1 type, indicative of nanoparticle aggregation (rather than porosity). Both the single-point Brunauer-Emmett-Teller and Barrett-Joyner-Halenda measurements revealed that the silica nanoparticles had an average surface area of 62.77 cm^3/g and a pore volume of 0.350 cm^3/g (Figure 3.2B). These types of values are typical for Stober silica nanoparticles, as reported in the reference literature (Vittoni et al., 2019).

Overall, based on IUPAC guidelines (Thommes et al., 2015), the silica, *B. mori* and Tasar silk nanoparticles were non-porous and classified as type II materials because their isotherm graphs showed monolayer adsorption up to high P/Po. I then assessed the morphology of the nanoparticles by scanning electron microscopy. Both *B. mori* and Tasar silk nanoparticles had spherical shapes with sizes similar to those determined by dynamic light scattering (Figure 3.2C). These results correlated well with previous reports (e.g. (Matthew et al., 2022, Matthew et al., 2020, Seib et al., 2013)). The Stober silica nanoparticles also had a spherical shape and an average size similar to

that determined by dynamic light scattering, again in agreement with previous reports (e.g. (Greasley et al., 2016, Khanna et al., 2018a)).

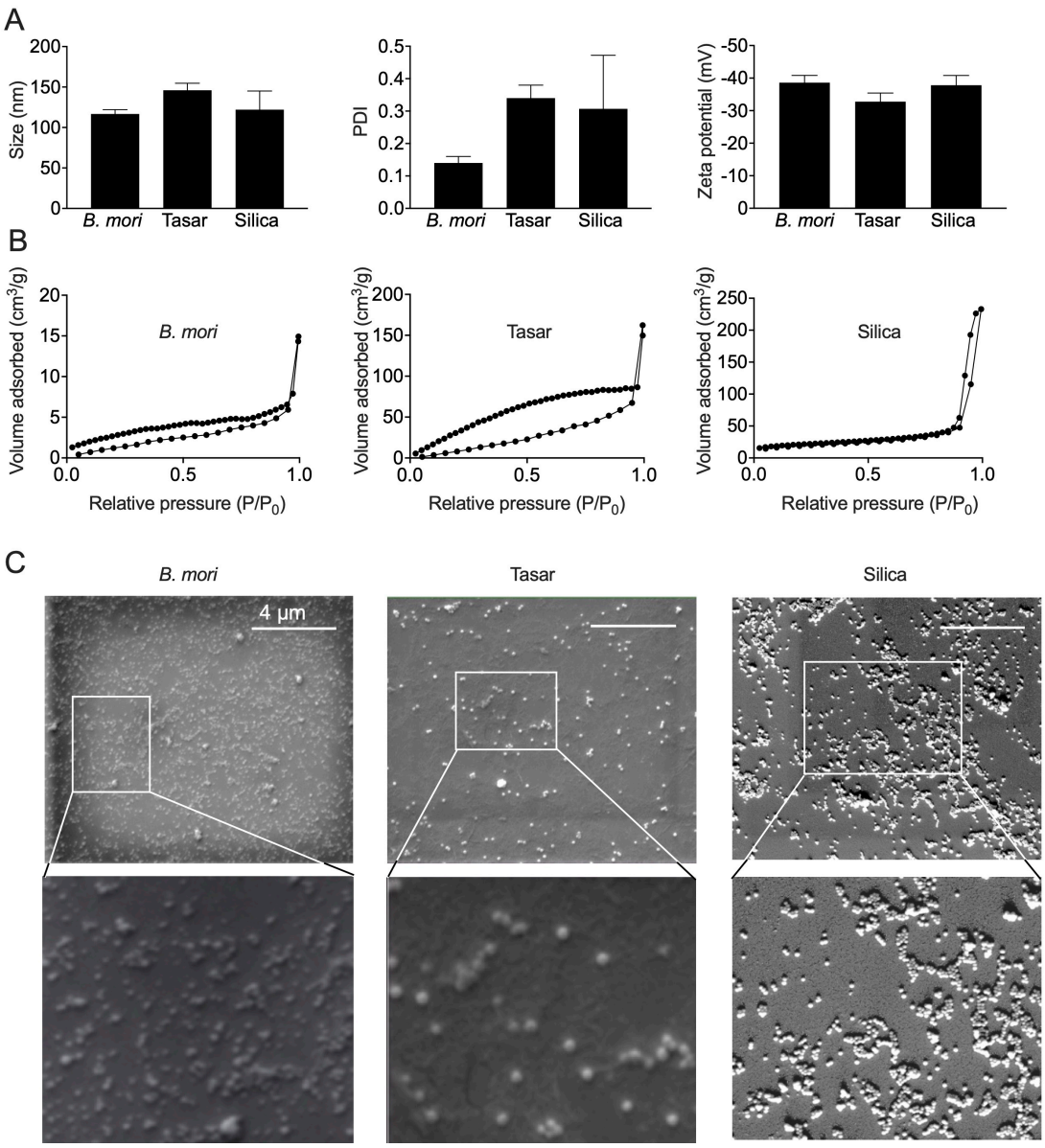

Figure 3.2 Nanoparticle characterisation of silica, *B. mori* silk, and *A. mylitta* (Tasar) silk nanoparticles. (A) Particle diameter (measured by dynamic light scattering [DLS]), polydispersity (PDI) and zeta potential values. Data are presented as mean ± SD, n=6 independent measurements, (B) surface area and pore volume measurements using nitrogen adsorption. n=1 from 6 pooled batches, and (C) morphology of nanoparticles by scanning electron microscopy (scale bar, 4 µm; zoom, 2 µm).

FTIR spectroscopy was used to determine the silk secondary structure and the different functional groups present in the silica nanoparticles (Figure 3.3C). The Stober silica nanoparticles showed a typical absorption peak of Si-O-Si (797.45 cm^{-1} and 1062.79 cm^{-1}) and Si-OH asymmetric stretching vibration (945.81 cm^{-1}) (Figure 3.3C), in agreement with previous reports (Launer and Arkles, 2013). The secondary structure of the silk nanoparticles and hydrogels indicated extensive β-sheets in our self-assembled silk hydrogels and particles (Figure 3A and B), consistent with other literature (e.g. (Matthew et al., 2020, Egan et al., 2022)). The FTIR results showed an amide I absorption peak at 1600–1700 cm^{-1} for all silk samples (Figure 3.3A). Comparison of the spectra from *B. mori* and Tasar silk nanoparticles and hydrogel composite nanoparticles to the spectra from air-dried silk films (negative control) and silk films treated with 70% v/v ethanol/distilled water (positive control) revealed the highest β-sheet content in the positive control silk films (Figure 3.3B). The β-sheet contents of *B. mori* and Tasar silk nanoparticles were 62% and 58%, respectively, whereas the β-sheet content of the silk hydrogels and air-dried silk films (negative control) were 32% and 23%, respectively (Figure 3.3B). Overall, these data correlated well with our own studies (Matthew et al., 2020) and previous studies by others (Subia et al., 2014, Lammel et al., 2010).

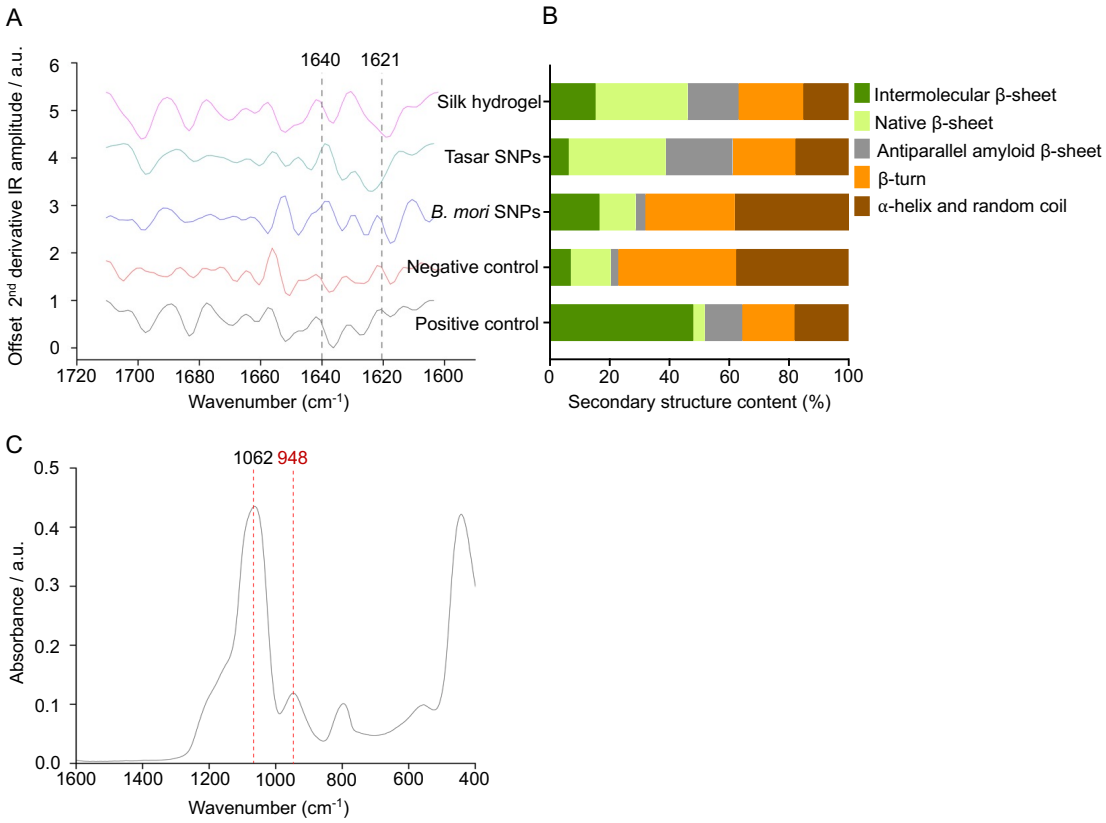

Figure 3.3 Fourier-transform infrared (FTIR) spectra and peak assignments. (A) FTIR spectra of *B. mori* and Tasar silk nanoparticles, silk hydrogels, air-dried silk film (negative control), and 70% ethanol-treated silk film (positive control). (B) Analysed secondary structure. (C) FTIR spectra of non-porous silica nanoparticles.

I also assessed the impact of the incorporation of homo- and heterotypic nanoparticles on hydrogel mechanics. I speculated that the formation of these composites would result in different mechanics than those observed in the pristine silk hydrogels. This speculation was based on the ability of nanoparticles to orchestrate hydrogel interactions, including the formation of dynamic nanoparticle–hydrogel structures or hydrogels with adhesive surface properties. These systems typically exploit polymer–nanoparticle interactions that impact the overall bulk properties mediated by surface adsorption, such as those occurring between silica nanoparticles and polyethylene glycol (PEG) (Pek et al., 2008), between hydrophobically modified cellulose

derivatives and PEGylated polylactide nanoparticles (Appel et al., 2015) or between TM50 silica and polyacrylamide hydrogels (Rose et al., 2014).

Nanoparticle shape also affects the hydrogel performance (Arno et al., 2020). Previous work has shown that silk reinforcement with silica increased bulk stiffness(Cheng et al., 2021). However, studies on silk hydrogels containing nanoparticles are lacking, so little is known regarding their mechanics or cellular responses. In the present study, the flow behaviour of silk hydrogels in the presence of nanoparticles is reported by comparing the stiffness of a 3% w/v silk hydrogel with similar silk hydrogels containing *B. mori* silk, Tasar silk and non-porous silica nanoparticles (Figure 3.4A and Table 3.1). However, the initial elastic moduli did not differ for any of the tested hydrogels. For example, the stiffness was 1.23 kPa for the hydrogel containing 0.05% w/v *B. mori* silk (this was the highest measured value) and 1.10 kPa for the hydrogel containing 0.05% w/v Tasar silk nanoparticles. By contrast, the stress relaxation and the half stress-relaxation time showed some particle dependence, as silk hydrogels containing 0.5% w/v *B. mori* nanoparticles had the lowest value (97 s) (Figure 3.4B), while pure silk hydrogel had the highest value (312 s). These values were 163 s for silk hydrogels containing 0.05% (w/v) Stober silica nanoparticles s and 146 s for silk hydrogels containing 0.5% w/v *B. mori* silk nanoparticles (Figure 3.4B). Overall, these trends indicated that the interactions between the nanoparticles and the silk hydrogel did not drastically alter their behaviours. Possibly, the formation of physical crosslinks between the silk molecules that are responsible for the formation of the silk hydrogel was only slightly influenced by the nanoparticle doping. Perhaps the use of sequence-coded nanoparticles will provide better control over beta-sheet bulk assembly.

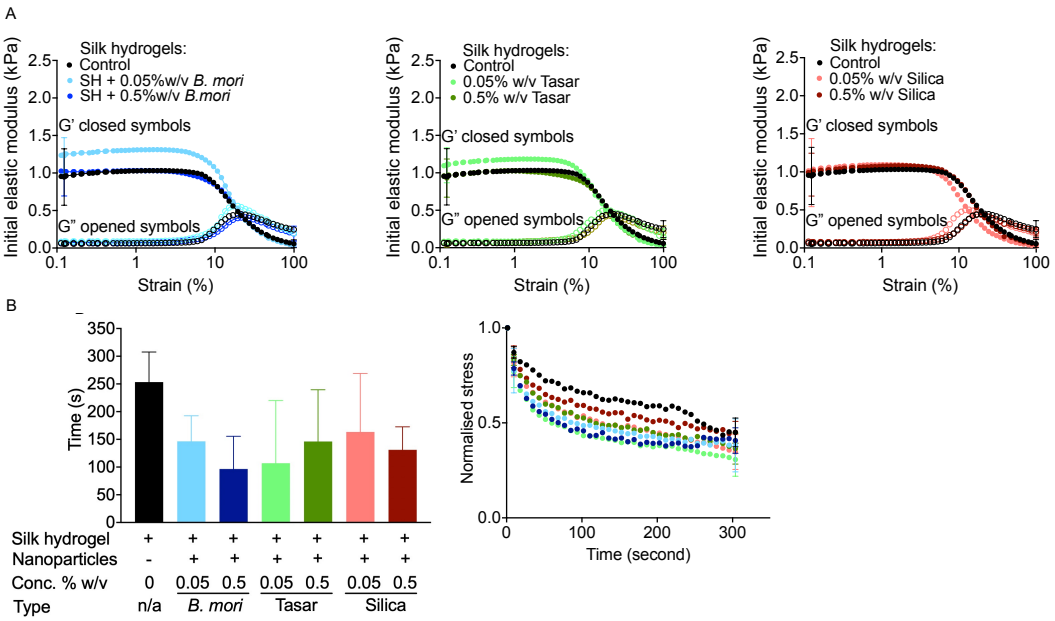

Figure 3.4 Impact of the nanoparticle concentration and type on silk hydrogel rheological properties. (A) Rheological behaviour of 3% w/v silk hydrogels doped with nanoparticles, (B) stress relaxation time and normalised stress relaxation time. Control refers to an undoped silk hydrogel. Data are presented as mean ± SD, n=3 independent experiments. E Closed symbols G' and open symbols G''.

Table 3.1 Impact of the nanoparticle concentration and type on silk hydrogel rheological properties including initial elastic modulus (stiffness) and half-stress relaxation time. Data are presented as mean ± SD, n = 3 independent experiments.

Samples	Initial elastic modulus (kPa)	Half-stress relaxation time (second)
Silk hydrogel (control)	0.95 ± 0.38	253.40 ± 54.20
Silk hydrogel + 0.05% w/v *B. mori* nanoparticles	1.23 ± 0.24	146.38 ± 46.24
Silk hydrogel + 0.5% w/v *B. mori* nanoparticles	0.98 ± 0.28	96.50 ± 59.03
Silk hydrogel + 0.05% w/v Tasar silk nanoparticles	1.10 ± 0.23	107.00 ± 113.12
Silk hydrogel + 0.5% w/v Tasar silk nanoparticles	0.93 ± 0.26	146.23 ± 93.21
Silk hydrogel + 0.05% w/v Silica nanoparticles	0.99 ± 0.45	163.46 ± 105.44
Silk hydrogel + 0.5% w/v Silica nanoparticles	0.96 ± 0.28	131.10 ± 41.58

The preliminary biological responses of the nanoparticle-doped silk hydrogels were also assessed. Prior work showed that embedding silica nanoparticles within silk fibroin hydrogels enhanced the bulk mechanical properties of the hydrogel while promoting mesenchymal stem cell adhesion, proliferation, and osteogenic differentiation (Cheng et al., 2021). In the present study, the addition of nanoparticles typically improved DU-145 cell attachment and proliferation when compared to unmodified silk hydrogels (Figure 3.5). However, the largest increase in DU145 cell numbers within 24 h was observed using tissue culture–treated polystyrene, which outcompeted all the silk substrates. This trend continued into days 6 and 9 of culture (Figure 3.5 A). Therefore, the Tasar nanoparticles used here apparently had little impact

on cell attachment. This was surprising because the presence of the RGD motif in this silk had been expected to improve cell–material interaction via integrin engagement. This lack of improvement in cell attachment could have several reasons, including restricted accessibility of the Tasar nanoparticles for integrin receptor engagement. Focal adhesion organisation shows a high sensitivity to ligand spacing, with a nanoscale average RGD spacing of 44 nm needed to form lipid raft domains at focal adhesion sites (Le Saux et al., 2011). This spacing mimics the RGD spacing found in the fibronectin (Bellis, 2011). Therefore, further work is needed to improve the nanoparticle placement and spacing in our silk hydrogels.

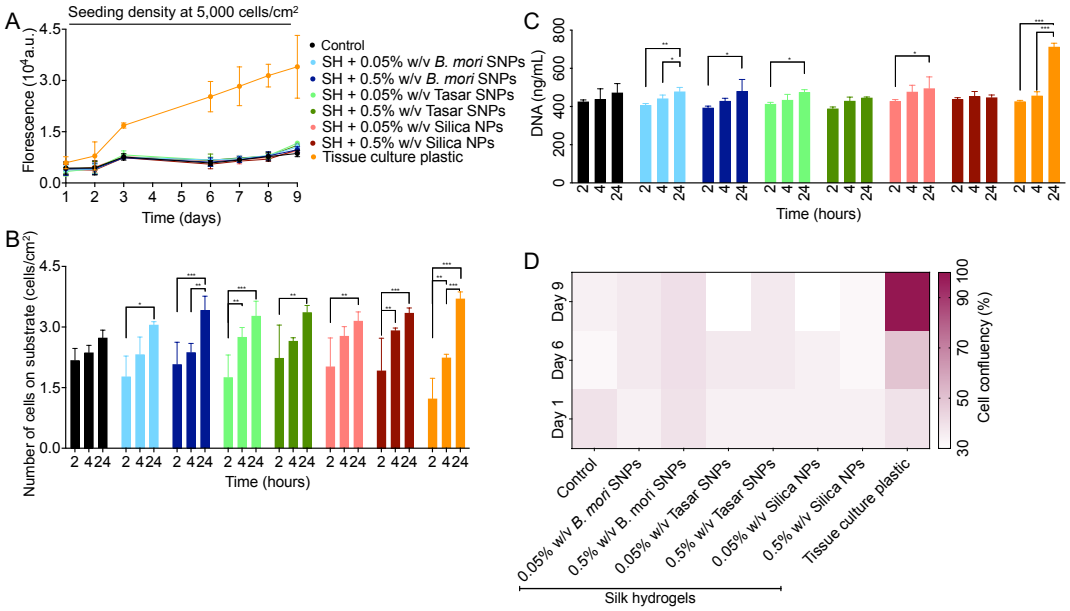

Figure 3.5 Silk hydrogels used for cell culture studies. (A) cell viability measurement using resazurin assay, (B) and (C) Cell attachment on silk hydrogels**.** Monitoring DU-145 cell attachment using PicoGreen and MTT assay at 2, 4, and 24 h. Control: DU-145 cells seeded on tissue culture-treated polystyrene. Data are presented mean **±** SD, n=3 independent biological experiments. One-way analysis of variance (ANOVA) followed by Tukey's multiple comparison test. Control versus silk hydrogels, (D) confluency at 1, 6, and 9.

3.5 Conclusions

Overall, this study explored the effects of adding various nanoparticle types on the material mechanics and biological interactions of composite self-assembling silk hydrogels. Silica, *B. mori* silk and Tasar silk nanoparticles were used to alter the stress relaxation of silk hydrogels to improve initial cell proliferation. However, more work is needed to fine-tune the cell material interactions for further improvement of the biological response. The present findings demonstrated the creation and application of homo- and heterotypic silk hydrogel composites.

Chapter 4

Functionalizing Silk Hydrogels with silk microfibres

Chapter summary:

This chapter details the mechanical properties of low (2% w/v) and high (10% w/v) *B. mori* and Tasar silk microfibre reinforced silk hydrogels. Next, the impact of these hydrogel composits on human induced pluripotent stem cell-derived MSCs (iPSC-MSCs) was assessed. Silk hydrogels functionalised with silk microfibres showed potential to promote short-term adhesion and proliferation of iPSC-MSCs.

This chapter has been submitted for publication. I designed, collected, analysed and interpreted the data and generated the manuscript draft. Napaporn Roamcharern assisted in cell staining and image analyses (Figure 4.8).

4.1 Abstract

Silk hydrogels have shown potential for tissue engineering applications, but several gaps and challenges, such as a restricted ability to form hydrogels with tuned mechanics and structural features, still limit their utilisation. Here, *B. mori* and *A. mylitta* (Tasar) silk microfibres were embedded within self-assembling silk hydrogels to modify the bulk hydrogel mechanical properties. First, *B. mori* and Tasar microfibres were prepared with lengths between 250 and 500 μm. Secondary structure analyses showed high beta-sheet contents of 61.12% and 63.13% for *B. mori* and Tasar microfibres, respectively. Mixing either microfibre type, at either 2% or 10% (w/v) concentrations, into 3% (w/v) silk solutions during the solution-gel transition increased the initial stiffness of the resulting silk hydrogels, with the 10% (w/v) addition giving a greater increase. Microfibre addition also altered stress relaxation, with the fastest stress relaxation observed with a rank order of 2% (w/v) > 10% (w/v) > unmodified hydrogels for either fibre type, although *B. mori* fibres showed a greater effect. Assessment of the biological responses by monitoring cell

attachment on these two-dimensional hydrogel substrates revealed greater numbers of human induced pluripotent stem cell-derived mesenchymal stem cells (iPSC-MSCs) attached to hydrogels containing 10% (w/v) *B. mori* microfibres as well as 2% (w/v) and 10% (w/v) Tasar microfibres at 24 h after seeding. Cytoskeleton staining revealed a more elongated and stretched morphology for cells growing on hydrogels containing Tasar microfibres. Overall, these findings illustrate that hydrogel stiffness, stress relaxation and iPSC-MSC responses towards silk hydrogels can be tuned with microfibres.

4.2 Introduction

Tissue engineering has emerged as a pivotal field in regenerative medicine, seeking innovative strategies to repair and replace damaged or lost tissues (Caddeo et al., 2017, Al-Ghadban et al., 2022). Its success depends on biomaterials that can facilitate tissue regeneration, for example, by providing supportive hydrogels for cell attachment (Chen et al., 2018b, Tian et al., 2019), proliferation (Yu et al., 2022), and differentiation (Kim et al., 2021, Yoon et al., 2018). Silk fibroin, derived from *B. mori* silkworms, has garnered significant interest for tissue engineering applications, in part due to its biocompatibility, biodegradation and resemblance to the natural extracellular matrix (ECM) (Kapoor and Kundu, 2016, Lyu et al., 2023). For example, silk hydrogels are able to mimic the viscoelastic properties of tissues (Phuagkhaopong et al., 2021), thereby offering an interesting platform for further exploration of their use in cell attachment and growth, as well as in scaffold fabrication required for more advanced tissue engineering applications. Tuning material mechanics is an integral part to tissue engineering.

Although silk fibre reinforcement was first pioneered for fabricating silk scaffolds for use in the tissue engineering (Mandal et al., 2012), it has since been used in hydrogels to enhance their mechanical strength (Yodmuang et al., 2015, Liu et al., 2019, Xiao et al., 2018, Kim, 2021). For example, reinforcement of silk hydrogels with 2% (w/v) *B. mori* fibres 500 μm in length

nearly doubled the hydrogel mechanical strength (Yodmuang et al., 2015). However, the incorporated microfibres do more than just enhance mechanical support; they also enhance cellular behaviour (Yodmuang et al., 2015). This phenomenon has also been observed with other hydrogel systems reinforced with *B. mori* fibres (Kim, 2021, Liu et al., 2019, Xiao et al., 2018).

To date, *B. mori* silk has been the material of choice for silk-mediated tissue engineering for several reasons. This is due, at least in part, to the robust supply chain of *B. mori* raw materials, the ease by which the fibre can be reverse-engineered into liquid silk and the clinical approval and use of *B. mori* silk in humans, both as its native spun fibre and its processed formats (Holland et al., 2019, Lyu et al., 2023). However, many different silks exist in Nature; indeed, silk has arisen at least 23 times via independent evolutionary events (Sutherland et al., 2010). This diversity guarantees that silk will continue to amaze. Even among Lepidoptera, the silks produced by different species provide a rich library with sequence variations that can be tapped into. For example, the silk produced by *A. mylitta* (the Tasar silkworm) shares many similarities with *B. mori* silk, but it differs in subtle but important ways in its primary protein sequence. For example, in contrast to *B. mori* silk fibroin, Tasar silk fibroin contains (i) a higher amount of alanine residues (Acharya et al., 2008a) and (ii) per molecule, 7 arginyl-glycyl-aspartic acid (RGD) sequences, which promote cell adhesion via integrin receptor engagement (Kapoor and Kundu, 2016, Naskar et al., 2021) *B. mori* silk lacks this RGD sequence, making Tasar silk an important contender in the “silk toolbox” (Kapoor and Kundu, 2016). Indeed, Tasar silk films and scaffolds have been shown to significantly improve primary cardiomyocyte performance, including cell attachment and proliferation (Patra et al., 2012) (reviewed in (Naskar et al., 2021)). The availability of integrin engagement for cell adhesion provided by Tasar silk is also relevant for other cell types, including pluripotent stem cells (iPSCs). The iPSCs are particularly promising for emerging tissue engineering therapies because they provide the unique opportunity of culturing limitless patient-specific stem and progenitor cells (reviewed in

(Santoro et al., 2019)), as well as iPSC-derived mesenchymal stem cells (MSCs).

Human iPSC-derived MSCs (iPSC-MSCs) are particularly promising in tissue engineering due to their potential for multilineage differentiation (Ozay et al., 2019, Chang et al., 2020) and for their immunomodulatory properties (Saetersmoen et al., 2019). The ability of iPSC-MSCs to differentiate into various cell lineages (Chang et al., 2020) can greatly aid tissue repair (Chang et al., 2020), regulating immune responses (Saetersmoen et al., 2019), and mitigating inflammation (Yang et al., 2019). This combination of regenerative and immunomodulatory potentials offers a comprehensive strategy for fabricating tissue engineering constructs with enhanced regenerative outcomes. Ultimately, iPSC-MSCs will benefit from novel delivery platforms that will maximise their therapeutic potential (Seib, 2018).

In the present study, I created silk hydrogels reinforced with either *B. mori* or Tasar silk microfibres and I characterised the hydrogel mechanics and assessed their cell culture performance using iPSC-MSCs. As part of this study, I also established a novel protocol for reverse engineering Tasar silk. Both silk microfibre types were characterised and each was embedded in a physically crosslinked silk hydrogel for assessment of their impact on hydrogel mechanics (Figure 4.1). The modified hydrogels were also used to assess iPSC-MSC cell attachment and viability (Figure 4.1).

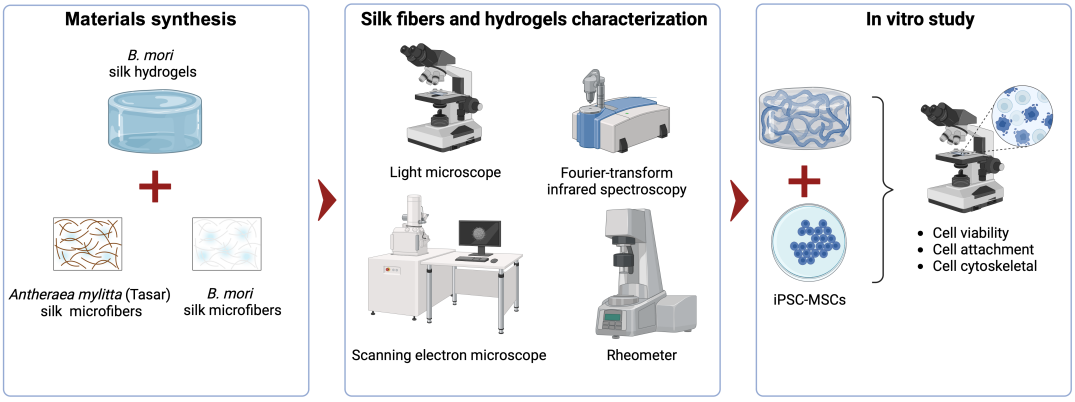

Figure 4.1 Diagram of overview process including silk hydrogels and silk microfibres synthesis, characterisation, and *in vitro* study.

4.3 Materials and Methods

4.3.1 *B. mori* and *A. mylitta* silk extraction

4.3.1.1 Silk fibroin solution from *B. mori* cocoons.

The *B. mori* silk solution was prepared as previously reported in Chapter 2.

4.3.1.2 *A. mylitta* (Tasar) silk fibres degumming.

The process of degumming Tasar silk cocoons was prepared as previously reported in Chapter 3.

4.3.2 *B. mori* and Tasar silk microfibre synthesis

B. mori or Tasar silk microfibre synthesis were based on the technique reported previously (Mandal et al., 2012) (Figure 4.2). Briefly, 1 g of dried, degummed silk fibres were submerged in 15 mL of 17.5 M NaOH solution for 20 min for *B. mori* silk fibres and for 5 h for Tasar silk fibres (Figure 1). The fibres were stirred using a spatula for 12 min. Next, 150 mL of deionised water was added, followed by centrifugation at 48,384 × g for 20 min. The supernatant was discarded, and the pellet was resuspended in 50 mL of deionised water, stirred, and centrifuged again. This step was repeated 5 times. After resuspension of the pellet in DI water, the pH was measured and adjusted to 7.0 by dropwise addition of HCl. The neutralised silk fibre solution was centrifuged again for 20 min and the final silk fibre pellet was resuspended in 2 mL of DI water. The silk fibres were filtered through a 500 µm strainer to create a major size in the range between 250 and 500 µm. Samples (100 µL) of each silk fibre were lyophilised for concentration measurements. Sample images were captured using light microscopy and analysed using ImageJ for Windows 1.8.0 (National Institutes of Health, Bethesda, USA).

4.3.3 Hydrogels manufacture

The 3% w/v self-assembling silk hydrogels were prepared as previously reported in Chapter 2.

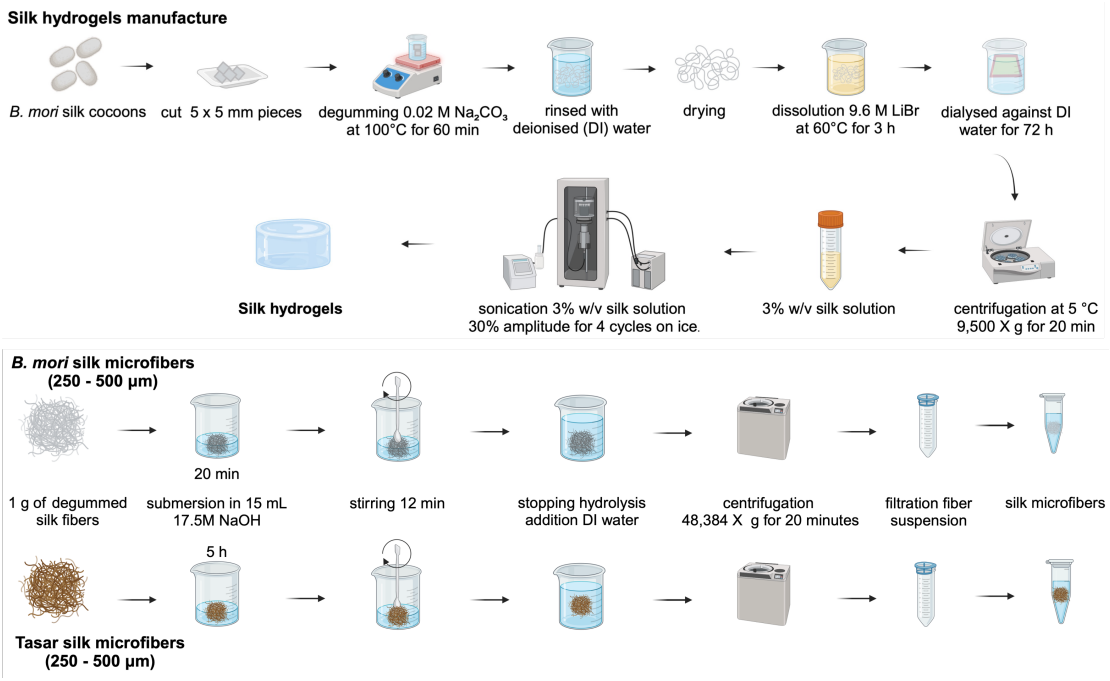

Figure 4.2 Manufacture of *B. mori* and *A. mylitta* (Tasar) silk microfibres and hydrogels.

4.3.4 Scanning electron microscopy (SEM) of *B. mori* and Tasar silk microfibres

B. mori and Tasar silk microfibre suspensions were adjusted to a concentration of 10 mg/mL. A 20 µL suspension of microfibres was pipetted onto a silicon wafer and lyophilised for 24 h at −10 °C and 0.14 mbar. The dried samples were sputter-coated with 15 nm of gold using an ACE200 low-vacuum sputter-coated (Leica Microsystems, Wetzlar, Germany). The fibre samples were imaged by field emission scanning electron microscopy (FE-SEM; SU6600 instrument; Hitachi High Technologies, Krefeld, Germany) with a 5 kV accelerating voltage. The hydrogel samples were imaged with a Quanta FEG-ESEM (FEI company, Hillsboro, OR, USA; now part of Thermo

Fisher Scientific Inc., Waltham, MA, USA). The images were processed using ImageJ for Windows 1.8.0 (National Institutes of Health, Bethesda, USA).

4.3.5 RGD-epitope identification

The RGD sequence on silk microfibres surface was detected using an integrin mimicking RGD-binding peptide (CWDDGWLC)-NH-$(CH_2)_6$-NH-Biotin (Peptide Protein Research Limited, Hampshire, UK) (Yang et al., 2015). 1 mg of air-dried, and alkaline-treated *B. mori* and Tasar silk microfibres were blocked for 1 h with buffer (pH=8.6, containing 0.1 mol/L $NaHCO_3$, 0.02% w/v NaN_3, and 5% w/v of bovine serum albumin). Each silk microfibres were washed 5 times in wash buffer (pH=7.5, containing 50 mmol/L Tris-HCl, 150 mmol/L NaCl, 0.1% w/v Tween-20). Next, silk microfibres were incubated with the integrin-mimicking RGD-binding peptide (0.1 mg/mL in wash buffer) for 30 minutes. Silk microfibres were washed 5 times in wash buffer to remove unbound peptides. Next, silk microfibres were treated with Streptavidin-colloidal gold (Sigma Aldrich) (1 mg/mL in wash buffer) for 45 minutes and rinsed in wash buffer. Then, silk microfibres were enhanced by a silver enhancing kit (Sigma Aldrich) for 20 minutes. Finally, all silk microfibres were washed 5 times and rinsed with deionised water. Silk microfibres in deionised water were imaged with a light microscope.

4.3.6 Silk secondary conformation analysis by Fourier-transform infrared spectroscopy (FTIR)

Silk secondary conformation measurements were performed as detailed in Chapter 3.

4.3.7 Rheology of silk hydrogels with and without silk microfibres.

Rheology measurements were performed as detailed in Chapter 2. For rheology measurement, equilibrate 3% (w/v) silk hydrogel microfibre systems overnight in DMEM containing 1g/L D-glucose.

4.3.8 Cell culture experiment

Human iPSC derived MSCs were purchased from the American Type Culture Collection (Manassas, VA, USA). Briefly, the iPSC-MSCs were cultured as monolayers in tissue culture flasks and on a 3% (w/v) silk hydrogel composite containing 2% or 10% (w/v) of silk microfibres in complete culture medium. Unless otherwise indicated, the cells were seeded at 5,000 cells/cm^2. Cells were cultured at 37°C in 95% relative humidity and 5% CO_2. The iPSC-MSCs were used for up to three passages.

4.3.9.1 iPSC derived MSC viability

Cell viability was measured at 24 h after seeding using the resazurin assay as described in Chapter 3.

4.3.9.2 iPSC derived MSC attachment on hydrogel

DNA quantification using PicoGreen assay measurement was performed as detailed in Chapter 3.

4.3.9.3 The actin filament visualisation of iPSC-MSC treated on silk hydrogel.

The iPSC-MSCs were cultured for 24 h on silk hydrogel substrates in glass bottom microwell dishes. The hydrogels were then fixed with 4% v/v methanol-free formaldehyde, permeabilised in 0.1% v/v Triton-X 100 for 15 min and blocked in 1% (w/v) bovine serum albumin (BSA; Sigma-Aldrich) for 1 h at room temperature. For actin filament visualisation, cells were stained for 1 h with 0.165 µM phalloidin-Alexa488, according to the manufacturer's instructions (Thermo Fisher Scientific Inc.) and imaging (Nikon Eclipse E600 upright epifluorescence microscope). Exposure time and other image settings for each respective channel were held constant during imaging. All images were equally adjusted, processed and analysed in ImageJ 1.8.0 (National Institutes of Health, Bethesda, USA). The images were analysed as detailed previously (Phuagkhaopong et al., 2021).

4.3.9.4 Image Analyses

Assessment of cytoskeletal organisation of the cells, single cells were manually traced from fluorescent actin images. Area, perimeter, fit ellipse, and shape descriptors were quantified by ImageJ. Cell area, circularity ((4 × π × area)/(perimeter^2)), roundness ((4 × area)/(π × major axis length^2)), and aspect ratio (major axis length/minor axis length).

Data and Statistical analyses

Data was analysed using GraphPad Prism 10.0.2 (171)@ (GraphPad Software, La Jolla, CA). One-way analysis of variance (ANOVA) followed by Tukey's multiple comparison test was used to analyse the iPSC-MSC viability, attachment, and staining measurement of silk hydrogels composite silk microfibres with control substrate cultures. Statistical significance was indicated by asterisks in each figure legend and assigned as follows; **p ≤ 0.05, ***p ≤ 0.005, and ****p ≤ 0.0001. All data were plotted as mean ± standard deviation (SD). The number of experiment repeats (n) is described in each figure legend.

4.4 Results

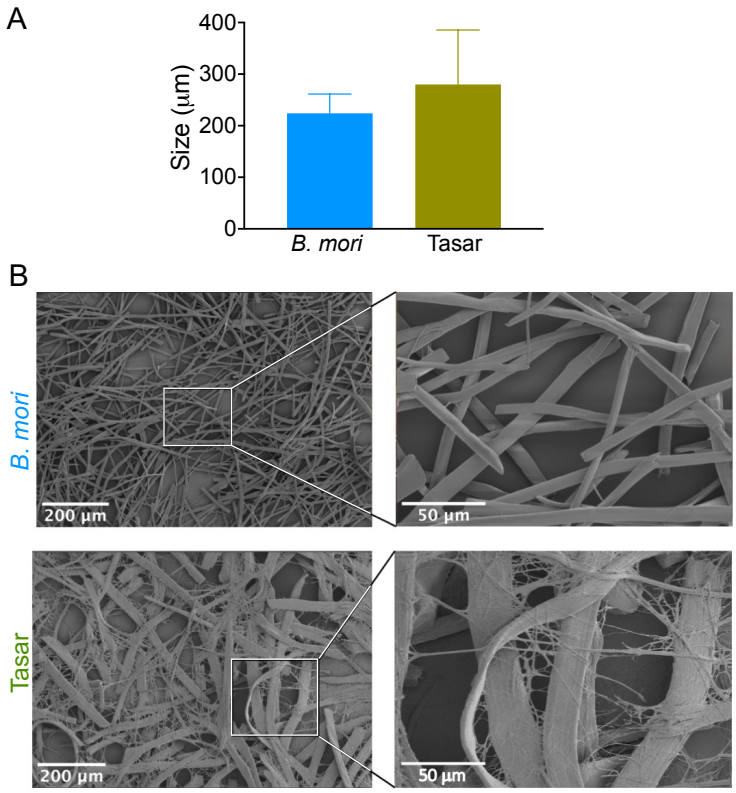

Figure 4.3 Morphology of silk microfibres. *B. mori* and *A. mylitta* (Tasar) silk microfibre characterisation using (A) size measurements and (B) morphological assessment of silk microfibres by scanning electron microscopy (scale bar, 200 µm; zoom, 50 µm).

The average lengths of *B. mori* and Tasar silk fibres were 223 ± 97 µm and 279.83 ± 105.67 respectively, although the differences were not statistically significant (Figure 4.2A). Qualitative surface morphology assessment indicated that microfibre types had a similar cylindrical shape, although the diameter of the Tasar silk fibre was approximately twice that of the *B. mori* fibre. The surface of the *B. mori* silk microfibres was generally smooth and glossy, whereas the microfibrils of the Tasar silk microfibres had a loose appearance (Figure 4.3B).

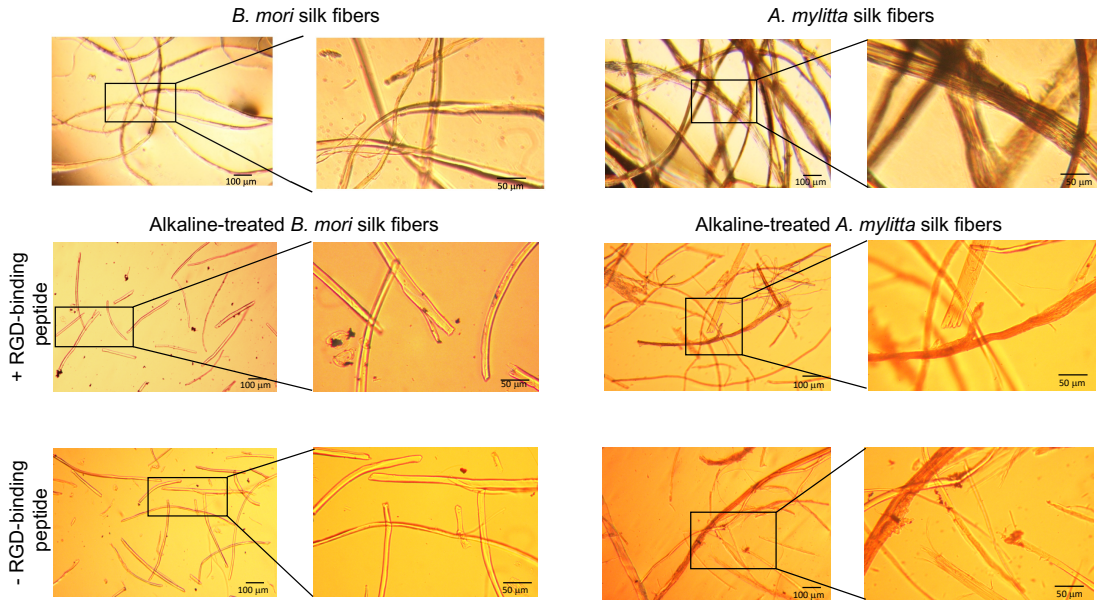

Figure 4.4 The RGD-sequencing peptide represented on silk microfibres surface area was observed using an inverted light microscope. The existence of RGD-sequencing peptide visualised as black spots by binding with (CWDDGWLC)-NH-$(CH_2)_6$-NH-Bio-biotin-streptavidin-gold nanoparticles enhanced with silver on the surface of *B. mori* and Tasar silk microfibres (Scale bar =100 and 50 µm). Air-dried silk microfibres are used as control.

RGD-sequences are absent in *B. mori* silk fibres but can be found in Tasar silk fibres. Therefore, it is important to confirm the existence of RGD sequences on Tasar silk fibres surface. The RGD binding sites can be observed under the light microscope (Figure 4.4). The RGD binding site was presented as black spots on the silk microfibre surface area. However, the black spots were not seen on the surface area of all treatment groups of silk microfibres (Figure 4.4).

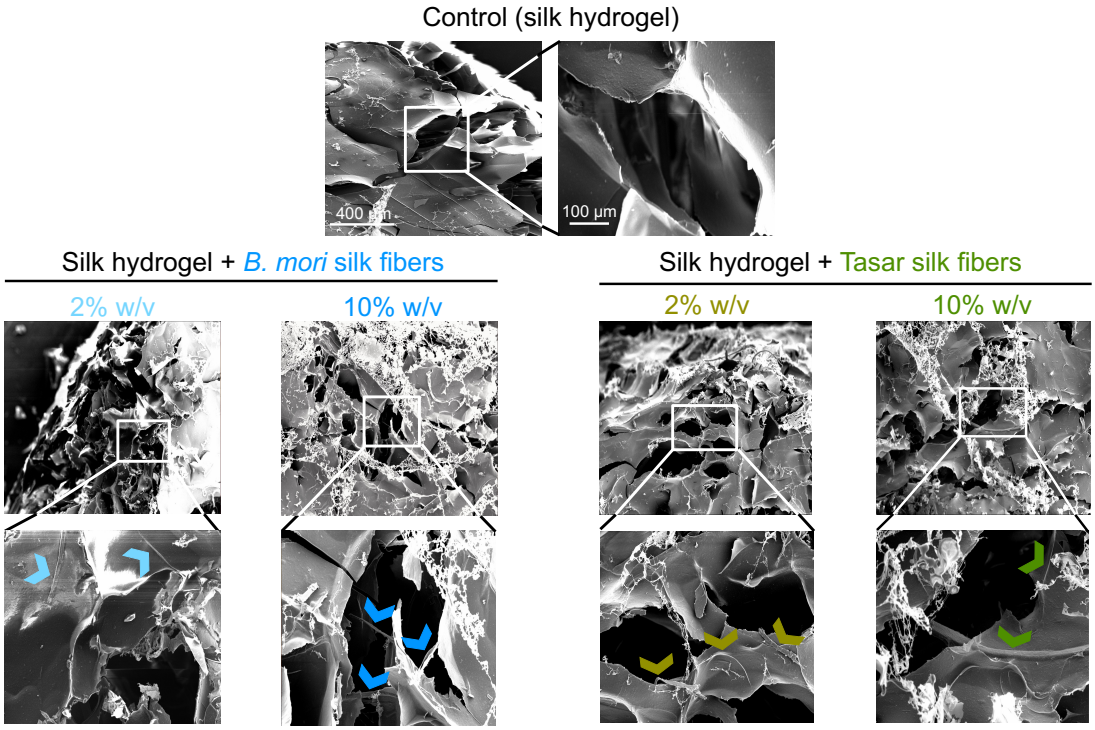

Figure 4.5 Silk hydrogel composites containing 2% and 10% (w/v) *B. mori* and *A. mylitta* (Tasar) silk microfibres. The hydrogel morphology was assessed using scanning electron microscopy (SEM) (scale bar, 400 µm; zoom, 100 µm). Silk hydrogels without microfibres were used as controls. Silk microfibres are indicated by arrows.

The morphology of self-assembled silk hydrogels spiked with 2% and 10% (w/v) silk microfibres was observed by SEM (Figure 4.5). Control silk hydrogels showed a uniform pore structure (typically 250–450 µm in diameter) and high porosity, while the fibre-reinforced hydrogels typically had uniform but smaller pores (approximately 222.05 ± 36.97 µm in diameter) (Figure 4.5). Both *B. mori* and Tasar silk microfibres were embedded within the silk hydrogel matrix. Increasing the silk microfibre content further reduced the internal porosity of the hydrogels, but the uniform structure was maintained (Figure 4.5).

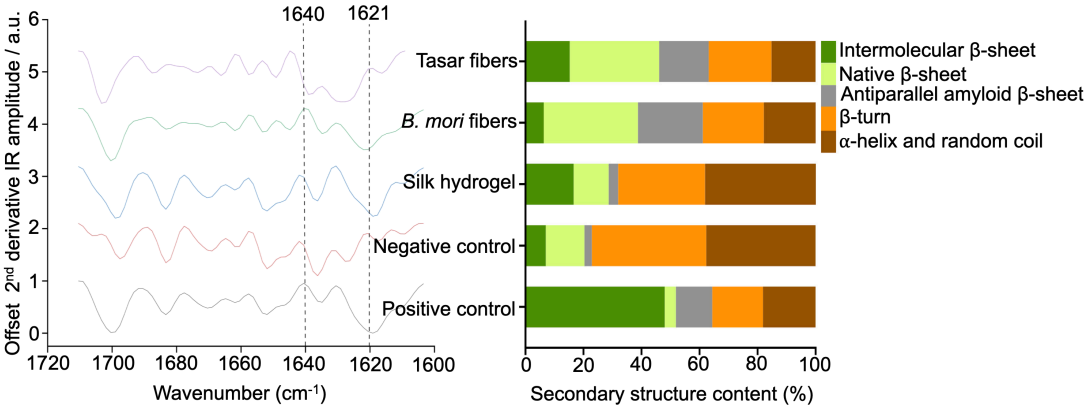

Figure 4.6 Secondary structure of silk samples. Fourier transform infrared (FTIR) spectra and peak assignment. (A) FTIR spectra of *B. mori* and *A. mylitta* (Tasar) silk microfibres, silk hydrogels, an air-dried film (negative control) and a 70% ethanol-treated silk film (positive control). Dashed lines indicate the β-sheet peak (1621 cm^{-1}) and the α-helix peak (1640 cm^{-1}), and (B) analysed secondary structure.

Assessment of the secondary structure of both microfibres and hydrogels using FTIR revealed the typical amide I absorption peak at 1600-1700 cm^{-1} in all silk samples (Figure 4.6). The spectra of silk films that had been air-dried only (negative control; amorphous) had the lowest β-sheet content (22.86%), while those treated with 70% v/v ethanol/distilled water (positive control; crystalline) had the highest β-sheet content (64.39%) (Figure 4.6). The β-sheet contents of Tasar and *B. mori* silk microfibres were 63.13% and 61.12%, respectively (Figure 4.6). The β-sheet content of the unmodified silk hydrogel was 31.92%.

Next, the mechanics of the 3% (w/v) silk hydrogel were compared with those of silk hydrogels containing *B. mori* and Tasar silk microfibres (Figure 4.7A and Table 4.1). The silk hydrogels without microfibres showed the lowest stiffness (1.47 kPa) (Figure 4.7A), and the hydrogel stiffness increased as the silk microfibre content increased (Figure 4.7A). Silk hydrogels containing 10% (w/v) Tasar silk microfibres had the highest stiffness (4.07 kPa), followed by silk hydrogels containing 10% (w/v) *B. mori* silk microfibres (3.03 kPa), 2%

(w/v) Tasar (2.62 kPa) and then 2% (w/v) *B. mori* (1.93 kPa) silk microfibres (Figure 5A). Determination of the stress relaxation (Figure 4.7B) and the stress relaxation half-time (Figure 4.7B) revealed that the control silk hydrogel with no fibres had the longest stress-relaxation time (144 s). However, independent of the fibre type, the fastest stress relaxation was observed with a rank order of 2% (w/v) > 10% (w/v) > unmodified hydrogels, and this effect was greatest for *B. mori* fibres (Figure 4.7B).

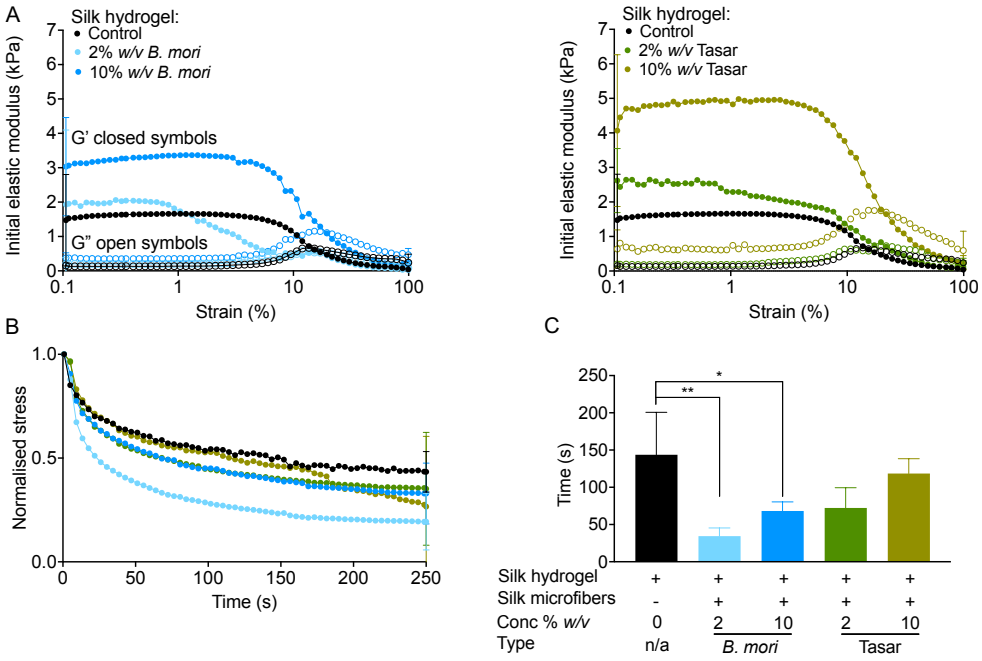

Figure 4.7 Impact of the microfibre amount and type on silk hydrogel mechanical properties. (A) Stiffness, (B) normalised stress relaxation time and (C) stress relaxation time profiles for 3% (w/v) self-assembled silk hydrogels (control) with and without microfibres. Silk hydrogels are denoted as SH. Data are presented as mean ± SD, n = 3 independent experiments.

Table 4.1 Impact of the microfibre amount and type on silk hydrogel mechanical properties including initial elastic modulus (stiffness) and half-stress relaxation time. Data are presented as mean ± SD, n = 3 independent experiments.

Samples	**Initial elastic modulus (kPa)**	**Half-stress relaxation time (second)**
Silk hydrogel (control)	1.47 ± 1.33	143.70 ± 57.00
Silk hydrogel + 2% w/v *B. mori* fibers	1.93 ± 2.17	34.44 ± 10.92
Silk hydrogel + 10% w/v *B. mori* fibers	3.03 ± 1.43	68.06 ± 12.20
Silk hydrogel + 2% w/v Tasar silk fibers	2.62 ± 0.93	72.26 ± 27.20
Silk hydrogel + 10% w/v Tasar silk fibers	4.07 ± 2.20	118.50 ± 19.90

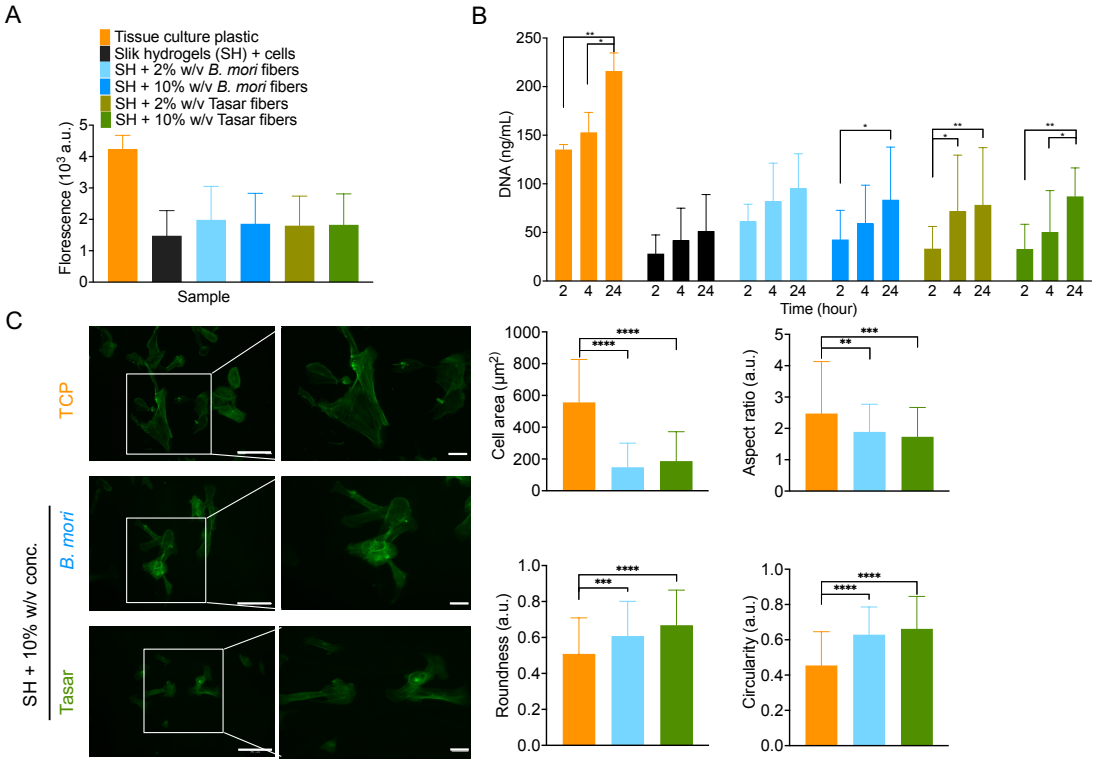

Figure 4.8 Response of stem cells (iPSC-MSCs) towards silk hydrogel culture substrates in two dimensions. (A) Cell viability at 24 h after seeding on silk hydrogels. (B) Quantification of iPSC-MSC cell attachment. Control: iPSC-MSC cells seeded on tissue culture–treated polystyrene. Data are presented as mean ± SD, n = 3 independent biological experiments. (C) Impact of substrate mechanics on iPSC-MSC cytoskeletal organisation. The iPSC-MSC spread after 24 h, focusing on cytoskeletal morphology. The images show F-actin cytoskeleton staining. Scale bars = 20 and 40 μm. Quantification of the morphological characteristics of iPSC-MSCs (106 cells in n = 21 images from three pooled experiments). One-way analysis of variance (ANOVA), followed by Tukey's multiple comparison test. For **p ≤ 0.05, ***p ≤ 0.005, and ****p ≤ 0.0001 comparison of silk hydrogels composite silk microfibres with control substrate cultures.

Next, the responses of iPSC-MSC cells towards these hydrogel substrates were measured to determine cell attachment and metabolic activity (Figure 4.8A and B, respectively). Assessment of metabolic activity showed that there

were no statistically significant differences between iPSC-MSCs cultured on 2D silk hydrogels containing *B. mori* and Tasar silk microfibres. However, the metabolic activity of cells grown on tissue culture–treated polystyrene (TCP) was twice the values observed for hydrogel substrates (Figure 4.8A).

Here, the DNA content was used to quantify the number of cell attachments. All hydrogel substrates showed a time-dependent increase in cell attachment. iPSC-MSCs grown on 2% (w/v) *B. mori* microfibre hydrogels showed substantial increases in cell numbers at 2 h after seeding. Compared to silk hydrogel without fibres, cell adhesion increased almost twice in all reinforced silk hydrogel substrates at 24 h. Surprisingly, there were no statistically significant cell adhesion differences in silk hydrogels containing *B. mori* and Tasar silk microfibres (Figure 4.8B).

Assessment of the cell morphology at 24 h culture time point revealed that the iPSC-MSC positive controls cultured on tissue culture–treated polystyrene showed greater stretched and elongated morphology when compared to that of cells grown on silk hydrogels containing either 2 or 10% (w/v) *B. mori* or Tasar silk microfibres (Figure 4.8C). The iPSC-MSCs cultured on tissue culture–treated polystyrene showed signs of membrane protrusion, with local actin polymerisation, whereas these features were infrequently observed in the iPSC-MSCs cultured on silk hydrogels or their respective silk microfibre hydrogels (Figure 4.8C). Quantifications of the cell area, aspect ratio, roundness and circularity revealed that the iPSC-MSCs cultured on reinforced silk hydrogels had a greater roundness and circularity when compared to those cells grown on tissue culture plastic.

4.5 Discussion

Reinforcing hydrogels with silk microfibres broadens their use in biomedical and engineering applications. For example, fibre-reinforced hydrogels have increased mechanical strength making them useful for hard tissue engineering applications (Yodmuang et al., 2015, Liu et al., 2019, Kim, 2021). This tunability of mechanical properties is critical, as it enables matching of the

construct to a wider set of target tissues (which can have a broad spectrum of mechanics). This, in turn, is important because mechanical matching promotes better integration and, ultimately, functional restoration. Substrate stress relaxation is also important and has known effects on cell biology, including the functioning of stem cells (Chaudhuri et al., 2020). However, stress relaxation, in the context of silk, is only now being studied (Phuagkhaopong et al., 2021) and I still do not know how added fibres may impact stress relaxation. The added microfibres also introduce topographical cues that can guide cell adhesion, alignment, and migration (Yodmuang et al., 2015, Liu et al., 2019, Kim, 2021). To the best of my knowledge, the present study is the first to develop Tasar fibre reinforced *B. mori* silk hydrogels and to examine their substrate mechanics, including viscoelasticity. Tasar silk fibres are particularly attractive in tissue engineering because their primary structure contains, per silk molecule, seven RGD sequences that can be exploited for guiding cell attachment (Naskar et al., 2021).

Due to the weak mechanical properties of sonication-induced silk hydrogels, I included silk microfibres to improve the mechanical properties of these hydrogels. Here, I tested both *B. mori* and Tasar silk microfibres as silk hydrogel reinforcements and compared the resulting hydrogels to a control silk hydrogel without microfibres. I first used the protocol described by Mandal and co-workers to generate silk microfibres (Mandal et al., 2012). The aim was to generate microfibres that were 200 to 400 μm in length because this length has previously shown the best performance in silk scaffolds (Mandal et al., 2012) and hydrogels (Yodmuang et al., 2015). I used light microscopy to assess the fibre lengths, and the *B. mori* data are comparable to those reported in previous studies (Yodmuang et al., 2015, Mandal et al., 2012) (Figure 4.3). I then used the same parameter space for Tasar silk, but I extended the incubation time to 5 h to yield microfibres of comparable length to the *B. mori* fibres. Electron microscopy examination of the fine surface structure of the fibres revealed that the Tasar silk microfibres were approximately twice as wide as *B. mori* fibres (Figure 4.3). This difference arises due to the different spinning geometries inherent to *B. mori* and Tasar silkworm physiology. The

processed *B. mori* silk microfibre had a smooth surface appearance, whereas the Tasar silk microfibres showed some microfibrils, as reported previously (Darshan et al., 2017). Tasar silk cocoons are tightly woven to provide maximum protection during the four-month pupal diapause (Darshan et al., 2017). By contrast, the fully domesticated *B. mori* cocoon is readily reeled and the pupa immediately starts metamorphosis.

I also determined the fibre secondary structure by FTIR spectroscopy. One factor that impacts the structure of silk microfibre is the beta-sheet content, which forms via hydrogen-bonding interactions between the silk chains. These hydrogen bonds create a highly ordered and rigid crystalline structure (Johari et al., 2020). The presence of beta-sheets imparts greater stiffness and strength to the silk material (Johari et al., 2020) because the hydrogen bonds in the beta-sheet structure resist deformation and provide mechanical support (Johari et al., 2020). The secondary structures of Tasar and *B. mori* microfibres, as well as of the 3% w/v of silk hydrogels, were analysed and deconvoluted between wavenumbers 1600 and 1710 cm^{-1} (amide I band) (Figure 4.6). The findings showed that the beta-sheet contents of the microfibres of both Tasar and *B. mori* silks were significantly higher than the beta-sheet content of the silk hydrogels or the air-dried silk films (negative control) (Figure 4.6). These results were expected and are comparable to data reported previously (Egan et al., 2022, Phuagkhaopong et al., 2021).

Silk hydrogels, especially at those >3% (w/v), are prone to cracking under low-stress conditions due to a lack of energy dissipation mechanisms (Zheng and Zuo, 2021). The addition of silk microfibres to a brittle hydrogel matrix increases its stiffness, resulting in improved mechanical properties (Yodmuang et al., 2015, Liu et al., 2019, Kim, 2021). Fibre-reinforced hydrogels have been investigated for tissue engineering by incorporating *B. mori* fibres within a spectrum of hydrogel matrices (Yodmuang et al., 2015, Liu et al., 2019, Kim, 2021). For example, adding 2% (w/v) *B. mori* silk microfibres to an 8% (w/v) silk hydrogel was able to mimic the mechanical properties of native cartilage *in vitro* (Yodmuang et al., 2015). In the present study, silk hydrogels were

reinforced with silk microfibres using the same (i.e. 2% [w/v]) and higher (i.e. 10% [w/v]) concentration of fibres to assess the impact of silk microfibres on the mechanical properties of a silk hydrogel. Increasing the concentration of silk fibres led to an increased initial modulus (stiffness) (Figure 4.7), which is consistent with previous findings (Yodmuang et al., 2015, Liu et al., 2019). The Seib Lab previously showed that 4% (w/v) silk hydrogels show stress relaxation; however, the impact of fibre reinforcement is unknown.

Microfibre reinforcement increases the mechanical strength of hydrogels. However, in the present study, I now provide the first demonstration that fibre addition also increases the speed of stress relaxation, thereby enabling greater material plasticity.

I speculate that the presence of microfibres provided 'flow points' within our hydrogels. Therefore, the application of stress eases the material flow, resulting in shorter material relaxation times. The flow points are better when provided by the smooth *B. mori* microfibres than by the coarse Tasar microfibres. However, the experimental data also showed that the increased speed of stress relaxation was inversely correlated with the fibre content. This observation may seem counterintuitive but might be explained by changes in the hydrogel morphology. The morphological analyses revealed that the structural uniformity was maintained in the microfibre-reinforced hydrogels, but the silk microfibre content reduced the internal porosity in a manner that correlated with the fibre content (Figure 4.5). Therefore, I speculate that the balance of 'flow points' and internal porosity governs the stress relaxation times (Figure 4.7B).

I also assessed the impact of silk hydrogel reinforcement with *B. mori* and Tasar silk microfibres on iPSC-MSC biology by monitoring cell attachment over the first 24 h after seeding (Figure 4.8). All hydrogels strengthened with *B. mori* and Tasar silk microfibres showed improved iPSC-MSC attachment. Hydrogels reinforced with Tasar silk microfibres at either 2% or 10% (w/v) concentrations exhibited significant increases in cell attachment compared to

B. mori fibre-reinforced or control hydrogels (Figure 4.8). Improvement in cell attachment in response to Tasar silk is therefore in line with previous findings using films and three-dimensional scaffolds (e.g., (Patra et al., 2012)). Assessment of cell metabolic activity at 24 h post-seeding revealed values that were approximately 50% lower in cells cultured on reinforced hydrogels than in control cells cultured on tissue-culture polystyrene (which essentially enables 100% cell attachment). Therefore, the data not only corroborate the cell attachment data, but they also highlight that further work is needed to maximise cell–substrate engagement.

Finally, morphological quantification of iPSC-MSCs growing on silk hydrogels reinforced with 10% w/v microfibres revealed that the iPSC-MSCs were able to stretch and elongate on these substrates. However, the iPSC-MSCs grown on tissue-culture plastic substrates had the largest surface area (i.e. spreading), as is typical and expected for these rigid substrates (e.g. (Seib et al., 2009a, Seib et al., 2009b)

4.6 Conclusion

I have examined the impact of silk hydrogel reinforcement on substrate mechanics and biology. Here, *B. mori* and Tasar silk microfibres were successfully manufactured and embedded in *B. mori* hydrogels, with a resulting improvement in mechanical strength and faster stress relaxation. When compared to a tissue-culture polystyrene substrate, silk hydrogels functionalised with silk microfibres promoted short-term iPSC-MSC adhesion and enhanced metabolic activity, despite a lack of quantitative cell attachment. Overall, the findings of this study demonstrated that the reinforcement of silk hydrogels with different concentrations of silk microfibres alters the mechanical properties and impacts iPSC-MSC cell biology when cultured in two dimensions.

Chapter 5
Thesis conclusion and future work

Chapter summary:

This chapter provides a summary of the outcomes of this thesis and suggestions for future work. The research outputs of the thesis included: (i) the impact of nanoparticles and silk microfibres on the mechanical properties of viscoelastic *B. mori* silk hydrogel (submitted manuscript) and (ii) the impact of nanoparticles and silk microfibres on cell adhesion (submitted manuscript). I have also contributed to additional publications as a co-author (see Appendix). For future work, based on this thesis's main findings, more work is needed to fine-tune the cell material interactions for further improvement of the biological response.

5.1 Thesis conclusions

Silk has been used for sutures for millenia (Holland et al., 2019). Due to silk's excellent mechanical properties, biocompatibility, biodegradability, and non-toxicity, it has been used as a biomaterial for tissue engineering (Holland et al., 2019). Silk has been processed into various forms such as scaffolds, films, and hydrogels (Holland et al., 2019). These materials are used as structural supports for tissue regeneration in applications such as bone, cartilage, skin, and nerve tissue engineering. During my PhD, I have come across various research studies that concentrate on *B. mori* silk hydrogel. These studies have explored its potential to support cell growth in long-term conditions (Abbott et al., 2016), tissue engineering (Osama et al., 2018), and drug development (Wongpinyochit et al., 2016, Seib, 2018). However, there is still a significant gap in understanding the development of composite silk hydrogels that contain biomaterials, including nanoparticles and microfibres, and their impact on material properties and biological behaviour. The silk fibroin extracted from *B. mori* silk cocoons lacks the RGD-sequencing peptide that selectively promotes integrin-mediated cell adhesion (Holland et al., 2019). Alternative options include the material that contains RGD-sequencing peptide into *B. mori* silk

hydrogel. So, in this study, the *A. mylitta* (Tasar) silk in nanoparticles and fibres formats which have RGD-sequencing peptide in their structure were introduced to *B. mori* silk hydrogel to tune the mechanical properties and improve the cell adhesion. Since the start of this PhD, a few studies have used biomaterial including nanoparticles and microfibres to alter the mechanical properties of silk hydrogel (Kim, 2021, Liu et al., 2019, Haghighattalab et al., 2022, Yodmuang et al., 2015). Overall, my thesis explored the effects of adding various nanoparticle types on the material mechanics and biological interactions of composite self-assembling silk hydrogels. The nanoparticles were embedded into silk hydrogel to tune the mechanical properties of silk hydrogel.

The first part of this thesis examined the impact of porous and non-porous silica nanoparticles on the mechanical properties of 3% w/v *B. mori* silk hydrogel. Non-porous and porous (commercial SBA-15) silica nanoparticles in the size range between 100-400 nm were embedded into 3% w/v of *B. mori* silk hydrogel at low (0.10% w/v) and high (5% w/v) of silica nanoparticles. The result concluded that silk hydrogel loaded with a high (5% w/v) concentration of silica nanoparticles promoted a higher stiffness of 2.11 kPa than a lower concentration of 0.10% w/v 1.48 kPa.

In the second part of this thesis, the effects of low (0.05% w/v) and high (0.5% w/v) of homotypic (*B. mori* and *A. mylitta* (Tasar)) and heterotypic (non-porous) silica nanoparticles on the mechanical properties of silk hydrogel was investigated. Another objective was to evaluate the efficacy of these systems in promoting DU-145 cell adhesion, with the goal of controlling the interface between cells and materials. The addition of nanoparticles improved DU-145 cell attachment and proliferation compared to unmodified silk hydrogels. However, tissue culture-treated polystyrene outcompeted all silk substrates, resulting in the largest increase in cell numbers within 24 h. The Tasar nanoparticles used in this study had minimal effect on cell attachment, which was unexpected. I anticipated that the RGD motif present in the silk would enhance cell-material interaction through integrin engagement. The lack of

improvement in cell attachment could be attributed to various factors, such as the limited accessibility of the Tasar nanoparticles for integrin receptor engagement.

The final part of the thesis evaluated the impact of low (2% w/v) and high (10% w/v) *B. mori* and Tasar silk microfibres on silk hydrogel and on Human induced pluripotent stem cell-derived MSCs (iPSC-MSCs) attachment. Silk hydrogel reinforced with *B. mori* and Tasar silk microfibres not only supported iPSC-MSCs proliferation and attachment but also enhanced cell stretching and elongation at 24 h after seeding. The Tasar silk microfibres promoted cell proliferation at both low and high concentrations, but tissue culture-treated polystyrene exhibited superior cell adhesion. In summary, the study found that the mechanical properties of silk hydrogels, which were reinforced with varying concentrations of silk microfibres, affect the behaviour of iPSC-MSCs cells in two dimensional. Hence, silk hydrogels enhanced with silk microfibres can encourage the short-term adhesion and growth of iPSC-MSCs.

5.2 Alternative materials for hydrogel synthesis.

Table 5.1 The alternative materials used to generate hydrogels: material, source, properties, drawback, application, and reference.

Materials	Source	Properties	Drawback	Application	Reference
Alginate (anionic polymers)	Brown seaweed	-Biocompatible -Low toxicity -Biodegradable -Ability to cross-link -Less immunogenicity	-Limited mechanical strength -prolonged stability issues arise due to ion exchange	Functionalised alginate hydrogels enhanced the mechanical strength of encapsulated islet function.	(Enck et al., 2021)
Collagen	Rat tail, Bovine tendon,	-Biocompatible -Biodegradable	-High variability in properties depends on	-Three-dimensional collagen hydrogel for	(Zhang et al., 2021d)

	Jelly fish, etc.	-Low viscosity -Low cytotoxicity	various manufacturing factors -Short degradation	functionalized nerve conduits -Collagen hydrogel incorporated with fibril-supported matrix mechanism properties of breast cancer cell line	(Sapudom et al., 2019)
Gelatin	Fish, Cattle, Bone, Skin	-Biocompatible -Biodegradable -Low viscosity -Low cytotoxicity -Fully absorbable -High solubility in aqueous systems	-Poor mechanical properties -Short degradation times -Temperature sensitivity -Limit in long-term stability	-Gelatin methacrylate (GelMA) injectable enhanced cartilage formation capacity. -Gelatin methacrylate cross-linked with tetrazine and norbornene had potential for compartment-talised coculture systems.	(Xu et al., 2022) (Contessi Negrini et al., 2021)
Hyaluronic acid	Human and bacterial fermenta-tion	-Biocompatible -Non-adhesive -Immunoneutral	-Limited mechanical strength -Rapid enzymatic degradation in vivo	Hyaluronic acid hydrogels show potential as a matrix that mimics the extracellular matrix (ECM) for the in vitro development	(Suo et al., 2019)

				of breast cancer.	
Matrigel™	a gelatinous protein mixture derived from Engelbreth -Holm-Swarm (EHS) mouse sarcoma cells.	-Enrich in laminin, collagen type IV, perlecan, and entactin -Closely resembles the natural ECM found in tissues -Support the formation of new blood vessels (angiogenesis)	-Batch-to-batch variability and potential transmission of animal pathogens -Lack of Defined Composition - Limited Shelf Life -Ethical Concerns	Matrigel was used to mimic extracellular matrix and cancer research models.	(Benton et al., 2014)

Hydrogels utilized in tissue engineering offer a supportive and biocompatible milieu for cell growth, tissue regeneration, and wound healing (Brovold et al., 2018). Silk hydrogels share common properties, including biocompatibility and biodegradability, with other hydrogels (refer to Table 6) (Brovold et al., 2018). Notably, silk hydrogels exhibit superior mechanical strength, making them more resilient in load-bearing applications (Brovold et al., 2018). In contrast, alginate hydrogels may exhibit limited stability under extreme pH conditions, restricting their use in specific environments (Brovold et al., 2018, Lee and Mooney, 2012). Silk hydrogels demonstrate lower immunogenicity compared to collagen and gelatin hydrogels, coupled with slower degradation rates than collagen, gelatin, and hyaluronic acid, enhancing their longevity in certain applications (Brovold et al., 2018, Lee and Mooney, 2001). Chitin/chitosan hydrogels, however, present more complex preparation processes. Matrigel™ is a well-established and widely used (Benton et al., 2014). It is important to consider the animal origin, batch variability, and potential immunogenicity (Benton et al., 2014).

Silk hydrogels surpass other hydrogels in tissue engineering owing to their outstanding biocompatibility, biodegradability, and mechanical strength (Seib, 2018, Zheng and Zuo, 2021). The natural protein composition minimizes adverse reactions, rendering silk hydrogels suitable for medical applications. Their gradual degradation aligns with tissue regeneration needs, offering temporary support without long-term complications. Noteworthy mechanical properties, characterized by remarkable strength and flexibility, facilitate effective mimicry of native tissues (Seib, 2018, Zheng and Zuo, 2021). Customization of these properties enables their application across diverse tissues, ensuring an optimal match for specific mechanical requirements. In this study, Tasar silk nanoparticles and microfibers were incorporated into B. mori silk hydrogel to enhance cell-cell interaction, leveraging the RGD-sequences in Tasar silk crucial for cell attachment. Silk hydrogels excel in facilitating cell attachment and proliferation, crucial for tissue engineering success.

5.3 Future directions

The results of this thesis suggest new research directions for others to explore. Some of these potential directions are summarised below.

5.3.1 Impact of stress relaxation on cellular response in 3D culture.

The findings of this thesis confirm that the inclusion of nanoparticles and microfibres typically improved DU145 and iPSC-MSCs cell attachment and proliferation when compared to unmodified silk hydrogels. However, the cell proliferation and cell adhesion were still less than the tissue culture plate (Chapters 3 and 4). However, the use of a flat two-dimensional cell culture cannot fully mimic the physiologically relevant microenvironment of cells in tissues. Under physiologically normal conditions, cells typically experience a three-dimensional substrate interface; this architecture is also relevant in the context of the delivery of cells to lesioned areas. Moreover, the exposure area of the Tasar nanoparticles and microfibres for integrin receptor engagement of DU-145 cells and iPSC-MSCs was restricted in two-dimensional cell culture.

Therefore, the accessible RGD-sequencing peptide for integrin receptor will be higher in three-dimensional cell cultures and it will be to confirm the validity of data obtained using oversimplified two-dimensional models and unrepresentative physiological conditions.

5.3.2 Improve the nanoparticle placement and spacing in our silk hydrogels.

This thesis confirmed that silk hydrogel composite with biomaterials supported cell growth rather than unmodified silk hydrogel (Chapters 3 and 4). However, the hypothesis of this research aims to see more impact on cell attachment in silk hydrogel composite Tasar silk nanoparticles and microfibres because Tasar silk contains RGD-sequencing peptide which can promote cell adhesion (Holland et al., 2019). The lack of improvement in cell attachment when cultured on Tasar nanoparticles, compared to tissue culture plates, may be due to limited accessibility for integrin receptor engagement. Focal adhesion organisation is susceptible to ligand spacing, with an average RGD spacing of 44 nm required to form lipid raft domains at focal adhesion sites, which mimics the RGD spacing found in fibronectin (Bellis, 2011, Le Saux et al., 2011). In previous studies, Tasar silk fibres were collected from the *A. mylitta* silk gland using the degumming process (Kundu et al., 2010, Subia et al., 2014). However, in this study, the Tasar silk fibroin was prepared using 1 N NaOH at a silk-to-NaOH ratio of 1 g to 25 mL. Unfortunately, the silk fibroin produced from this method had a low yield (3-7% w/v). Consequently, alternative methods for dissolving Tasar silk fibre should be explored in future studies. In order to increase the production yield of silk fibre with RGD-derived active peptides is necessary required. According to Parekh et al., the cryo-milling process was reported as the novel silk preparation method (Parekh et al., 2022). Degummed Tasar silk fibre was chopped and grinded to obtain a silk powder using cryo-mill equipment with stainless steel grinding ball. Silk powder was dissolved in Trifluoroacetic acid (TFA) to yield a high solubility of 20% w/v silk fibroin solution (Parekh et al., 2022). Hence, this could possibly contribute the diverse active peptide pool containing the RGD motif. Peptidomics or

relevant analyses might be beneficial in RGD-containing peptide screening before nanoparticle manufacture and silk fibre bio-conjugation.

REFERENCES

ABBOTT, R. D., KIMMERLING, E. P., CAIRNS, D. M. & KAPLAN, D. L. 2016. Silk as a Biomaterial to Support Long-Term Three-Dimensional Tissue Cultures. *ACS Applied Materials and Interfaces,* 8**,** 21861-8.

ACHARYA, C., GHOSH, S. & KUNDU, S. 2008a. Silk fibroin film from non-mulberry tropical tasar silkworms: A novel substrate for in vitro fibroblast culture. *Acta biomaterialia,* 5**,** 429-37.

ACHARYA, C., GHOSH, S. K. & KUNDU, S. C. 2008b. Silk fibroin protein from mulberry and non-mulberry silkworms: cytotoxicity, biocompatibility and kinetics of L929 murine fibroblast adhesion. *Journal of Materials Science: Materials in Medicine,* 19**,** 2827-36.

AL-GHADBAN, S., ARTILES, M. & BUNNELL, B. A. 2022. Adipose Stem Cells in Regenerative Medicine: Looking Forward. *Frontiers in Bioengineering and Biotechnology,* 9.

ALTMAN, G. H., HORAN, R. L., LU, H. H., MOREAU, J., MARTIN, I., RICHMOND, J. C. & KAPLAN, D. L. 2002. Silk matrix for tissue engineered anterior cruciate ligaments. *Biomaterials,* 23**,** 4131-4141.

ANAND, P., PANDEY, J. P. & PANDEY, D. M. 2021. Study on cocoonase, sericin, and degumming of silk cocoon: computational and experimental. *Journal of Genetic Engineering and Biotechnology,* 19**,** 32.

APPEL, E. A., TIBBITT, M. W., WEBBER, M. J., MATTIX, B. A., VEISEH, O. & LANGER, R. 2015. Self-assembled hydrogels utilizing polymer-nanoparticle interactions. *Nat Commun,* 6**,** 6295.

ARAI, T., FREDDI, G., INNOCENTI, R. & TSUKADA, M. 2004. Biodegradation of Bombyx mori silk fibroin fibers and films. *Journal of Applied Polymer Science,* 91**,** 2383-2390.

ARNO, M. C., INAM, M., WEEMS, A. C., LI, Z., BINCH, A. L. A., PLATT, C. I., RICHARDSON, S. M., HOYLAND, J. A., DOVE, A. P. & O'REILLY, R. K. 2020. Exploiting the role of nanoparticle shape in enhancing hydrogel adhesive and mechanical properties. *Nat Commun,* 11**,** 1420.

ASAKURA, T., OKUSHITA, K. & WILLIAMSON, M. P. 2015. Analysis of the Structure of Bombyx mori Silk Fibroin by NMR. *Macromolecules,* 48**,** 2345-2357.

BABU, K. M. 2019. 1 - Introduction to silk and sericulture. *In:* BABU, K. M. (ed.) *Silk (Second Edition).* Woodhead Publishing.

BANDYOPADHYAY, A., CHOWDHURY, S. K., DEY, S., MOSES, J. C. & MANDAL, B. B. 2019. Silk: A Promising Biomaterial Opening New Vistas Towards Affordable Healthcare Solutions. *Journal of the Indian Institute of Science,* 99**,** 445-487.

BARRETT, E. P., JOYNER, L. G. & HALENDA, P. P. 1951. The Determination of Pore Volume and Area Distributions in Porous Substances. I. Computations from Nitrogen Isotherms. *Journal of the American Chemical Society,* 73**,** 373-380.

BARROSO, I. A., MAN, K., HALL, T. J., ROBINSON, T. E., LOUTH, S. E. T., COX, S. C. & GHAG, A. K. 2022. Photocurable antimicrobial silk-based hydrogels for corneal repair. *Journal of Biomedical Materials Research Part A,* 110**,** 1401-1415.

BARUAH, R. R., CHANDRA KALITA, M. & DEVI, D. 2020. Novel non-mulberry silk fibroin nanoparticles with enhanced activity as potential candidate in nanocarrier mediated delivery system. *Royal Society of Chemistry Advances,* 10**,** 9070-9078.

BELDA MARIN, C., EGLES, C., HUMBLOT, V., LALATONNE, Y., MOTTE, L., LANDOULSI, J. & GUENIN, E. 2021. Gold, Silver, and Iron Oxide Nanoparticle Incorporation into Silk Hydrogels for Biomedical Applications: Elaboration, Structure, and Properties. *ACS Biomater Sci Eng,* 7**,** 2358-2371.

BELLIS, S. L. 2011. Advantages of RGD peptides for directing cell association with biomaterials. *Biomaterials,* 32**,** 4205-10.

BENTON, G., ARNAOUTOVA, I., GEORGE, J., KLEINMAN, H. K. & KOBLINSKI, J. 2014. Matrigel: From discovery and ECM mimicry to assays and models for cancer research. *Advanced Drug Delivery Reviews,* 79-80**,** 3-18.

BERTSCH, P., DIBA, M., MOONEY, D. J. & LEEUWENBURGH, S. C. G. 2023. Self-Healing Injectable Hydrogels for Tissue Regeneration. *Chemical Reviews,* 123**,** 834-873.

BITAR, A., AHMAD, N. M., FESSI, H. & ELAISSARI, A. 2012. Silica-based nanoparticles for biomedical applications. *Drug Discov Today,* 17**,** 1147-54.

BITAR, K. N. & ZAKHEM, E. 2014. Design strategies of biodegradable scaffolds for tissue regeneration. *Biomedical Engineering and Computational Biology,* 6**,** 13-20.

BITTENCOURT, D. M. C., OLIVEIRA, P., MICHALCZECHEN-LACERDA, V. A., ROSINHA, G. M. S., JONES, J. A. & RECH, E. L. 2022. Bioengineering of spider silks for the production of biomedical materials. *Frontiers in Bioengineering and Biotechnology,* 10**,** 958486.

BLATCHLEY, M. R. & ANSETH, K. S. 2023. Middle-out methods for spatiotemporal tissue engineering of organoids. *Nat Rev Bioeng,* 1**,** 329-345.

BOSO, D., MAGHIN, E., CARRARO, E., GIAGANTE, M., PAVAN, P. & PICCOLI, M. 2020. Extracellular Matrix-Derived Hydrogels as Biomaterial for Different Skeletal Muscle Tissue Replacements. *Materials,* 13**,** 2483.

BRAY, F., FERLAY, J., SOERJOMATARAM, I., SIEGEL, R. L., TORRE, L. A. & JEMAL, A. 2018. Global cancer statistics 2018: GLOBOCAN estimates of incidence and mortality worldwide for 36 cancers in 185 countries. *CA Cancer J Clin,* 68**,** 394-424.

BROVOLD, M., ALMEIDA, J. I., PLA-PALACÍN, I., SAINZ-ARNAL, P., SÁNCHEZ-ROMERO, N., RIVAS, J. J., ALMEIDA, H., DACHARY, P. R., SERRANO-AULLÓ, T., SOKER, S. & BAPTISTA, P. M. 2018. Naturally-Derived Biomaterials for Tissue Engineering Applications. *Adv Exp Med Biol,* 1077**,** 421-449.

BRUDER, S. P., JAISWAL, N. & HAYNESWORTH, S. E. 1997. Growth kinetics, self-renewal, and the osteogenic potential of purified human mesenchymal stem cells during extensive subcultivation and following cryopreservation. *Journal of Cellular Biochemistry,* 64**,** 278-94.

BUCCIARELLI, A. & MOTTA, A. 2022. Use of Bombyx mori silk fibroin in tissue engineering: From cocoons to medical devices, challenges, and future perspectives. *Biomater Adv,* 139**,** 212982.

CADDEO, S., BOFFITO, M. & SARTORI, S. 2017. Tissue Engineering Approaches in the Design of Healthy and Pathological In Vitro Tissue Models. *Frontiers in Bioengineering and Biotechnology,* 5.

CAI, J., LIU, S., FENG, J., KIMURA, S., WADA, M., KUGA, S. & ZHANG, L. 2012. Cellulose–Silica Nanocomposite Aerogels by In Situ Formation of Silica in Cellulose Gel. *Angewandte Chemie International Edition,* 51**,** 2076-2079.

CAO, Y. & WANG, B. 2009. Biodegradation of silk biomaterials. *International Journal of Molecular Sciences,* 10**,** 1514-1524.

CARVALHO, M. R., MAIA, F. R., VIEIRA, S., REIS, R. L. & OLIVEIRA, J. M. 2018. Tuning Enzymatically Crosslinked Silk Fibroin Hydrogel Properties for the Development of a Colorectal Cancer Extravasation 3D Model on a Chip. *Glob Chall,* 2**,** 1700100.

CATTO, V., FARÈ, S., CATTANEO, I., FIGLIUZZI, M., ALESSANDRINO, A., FREDDI, G., REMUZZI, A. & TANZI, M. C. 2015. Small diameter electrospun silk fibroin vascular grafts: Mechanical properties, in vitro biodegradability, and in vivo biocompatibility. *Materials Science and Engineering: C,* 54**,** 101-111.

CHANG, Y.-H., WU, K.-C. & DING, D.-C. 2020. Induced Pluripotent Stem Cell-Differentiated Chondrocytes Repair Cartilage Defect in a Rabbit Osteoarthritis Model. *Stem Cells International,* 2020**,** 8867349.

CHAO, P. H., YODMUANG, S., WANG, X., SUN, L., KAPLAN, D. L. & VUNJAK-NOVAKOVIC, G. 2010. Silk hydrogel for cartilage tissue engineering. *Journal of Biomedical Materials Research Part B: Applied Biomaterials,* 95**,** 84-90.

CHAUDHURI, O., COOPER-WHITE, J., JANMEY, P. A., MOONEY, D. J. & SHENOY, V. B. 2020. Effects of extracellular matrix viscoelasticity on cellular behaviour. *Nature,* 584**,** 535-546.

CHAUDHURI, O., GU, L., KLUMPERS, D., DARNELL, M., BENCHERIF, S. A., WEAVER, J. C., HUEBSCH, N., LEE, H.-P., LIPPENS, E., DUDA, G. N. & MOONEY, D. J. 2016. Hydrogels with tunable stress relaxation regulate stem cell fate and activity. *Nature Materials,* 15**,** 326-334.

CHEN, B.-Q., KANKALA, R. K., HE, G.-Y., YANG, D.-Y., LI, G.-P., WANG, P., WANG, S.-B., ZHANG, Y. S. & CHEN, A.-Z. 2018a. Supercritical fluid-assisted fabrication of indocyanine green-encapsulated silk fibroin nanoparticles for dual-triggered cancer therapy. *ACS Biomaterials Science & Engineering,* 4**,** 3487-3497.

CHEN, S., GUO, Y., LIU, R., WU, S., FANG, J., HUANG, B., LI, Z., CHEN, Z. & CHEN, Z. 2018b. Tuning surface properties of bone biomaterials to manipulate osteoblastic cell adhesion and the signaling pathways for

the enhancement of early osseointegration. *Colloids and Surfaces B: Biointerfaces,* 164**,** 58-69.
CHEN, Z., HAN, X., OUYANG, X., FANG, J., HUANG, X. & WEI, H. 2019. Transplantation of induced pluripotent stem cell-derived mesenchymal stem cells improved erectile dysfunction induced by cavernous nerve injury. *Theranostics,* 9**,** 6354-6368.
CHENG, Y., CHENG, G., XIE, C., YIN, C., DONG, X., LI, Z., ZHOU, X., WANG, Q., DENG, H. & LI, Z. 2021. Biomimetic Silk Fibroin Hydrogels Strengthened by Silica Nanoparticles Distributed Nanofibers Facilitate Bone Repair. *Advanced healthcare materials,* 10**,** e2001646.
CHUNG, H., KIM, T. Y. & LEE, S. Y. 2012. Recent advances in production of recombinant spider silk proteins. *Current Opinion in Biotechnology,* 23**,** 957-964.
CONTESSI NEGRINI, N., ANGELOVA VOLPONI, A., SHARPE, P. T. & CELIZ, A. D. 2021. Tunable Cross-Linking and Adhesion of Gelatin Hydrogels via Bioorthogonal Click Chemistry. *ACS Biomaterials Science & Engineering,* 7**,** 4330-4346.
COSTA, E., CLIMENT, E., GAWLITZA, K., WAN, W., WELLER, M. G. & RURACK, K. 2020. Optimization of analytical assay performance of antibody-gated indicator-releasing mesoporous silica particles. *Journal of Materials Chemistry B,* 8**,** 4950-4961.
COSTA, L. A., EIRO, N., FRAILE, M., GONZALEZ, L. O., SAÁ, J., GARCIA-PORTABELLA, P., VEGA, B., SCHNEIDER, J. & VIZOSO, F. J. 2021. Functional heterogeneity of mesenchymal stem cells from natural niches to culture conditions: implications for further clinical uses. *Cellular and Molecular Life Sciences,* 78**,** 447-467.
DANHIER, F., LE BRETON, A. & PRÉAT, V. 2012. RGD-Based Strategies To Target Alpha(v) Beta(3) Integrin in Cancer Therapy and Diagnosis. *Molecular Pharmaceutics,* 9**,** 2961-2973.
DANNERT, C., STOKKE, B. T. & DIAS, R. S. 2019. Nanoparticle-hydrogel composites: from molecular interactions to macroscopic behavior. *Polymers,* 11**,** 275.
DARSHAN, G. H., KONG, D., GAUTROT, J. & VOOTLA, S. 2017. Physico-chemical characterization of Antheraea mylitta silk mats for wound healing applications. *Scientific Reports,* 7**,** 10344.
DAS, D., YANG, Y., O'BRIEN, J. S., BREZNAN, D., NIMESH, S., BERNATCHEZ, S., HILL, M., SAYARI, A., VINCENT, R. & KUMARATHASAN, P. 2014. Synthesis and Physicochemical Characterization of Mesoporous Nanoparticles. *Journal of Nanomaterials,* 2014**,** 176015.
DASH, R., GHOSH, S. K., KAPLAN, D. L. & KUNDU, S. C. 2007. Purification and biochemical characterization of a 70 kDa sericin from tropical tasar silkworm, Antheraea mylitta. *Comparative Biochemistry and Physiology Part B: Biochemistry & Molecular Biology,* 147**,** 129-34.
DATTA, A., GHOSH, A. K. & KUNDU, S. C. 2001. Differential expression of the fibroin gene in developmental stages of silkworm, Antheraea mylitta (Saturniidae). *Comparative Biochemistry and Physiology Part B: Biochemistry & Molecular Biology* 129**,** 197-204.

DEORAY, N. & KANDASUBRAMANIAN, B. 2018. Review on Three-Dimensionally Emulated Fiber-Embedded Lactic Acid Polymer Composites: Opportunities in Engineering Sector. *Polymer-Plastics Technology and Engineering,* 57**,** 860-874.

DONG, C. & LV, Y. 2016. Application of Collagen Scaffold in Tissue Engineering: Recent Advances and New Perspectives. *Polymers (Basel),* 8.

ĐORĐEVIĆ, S., GONZALEZ, M. M., CONEJOS-SÁNCHEZ, I., CARREIRA, B., POZZI, S., ACÚRCIO, R. C., SATCHI-FAINARO, R., FLORINDO, H. F. & VICENT, M. J. 2022. Current hurdles to the translation of nanomedicines from bench to the clinic. *Drug Delivery and Translational Research,* 12**,** 500-525.

EGAN, G., PHUAGKHAOPONG, S., MATTHEW, S. A. L., CONNOLLY, P. & SEIB, F. P. 2022. Impact of silk hydrogel secondary structure on hydrogel formation, silk leaching and in vitro response. *Scientific reports,* 12**,** 3729.

ENCK, K., TAMBURRINI, R., DEBORAH, C., GAZIA, C., JOST, A., KHALIL, F., ALWAN, A., ORLANDO, G. & OPARA, E. C. 2021. Effect of alginate matrix engineered to mimic the pancreatic microenvironment on encapsulated islet function. *Biotechnology and Bioengineering,* 118**,** 1177-1185.

ENOMOTO, S., SUMI, M., KAJIMOTO, K., NAKAZAWA, Y., TAKAHASHI, R., TAKABAYASHI, C., ASAKURA, T. & SATA, M. 2010. Long-term patency of small-diameter vascular graft made from fibroin, a silk-based biodegradable material. *Journal of Vascular Surgery,* 51**,** 155-164.

FAZAL, N. & LATIEF, N. 2018. Bombyx mori derived scaffolds and their use in cartilage regeneration: a systematic review. *Osteoarthritis Cartilage,* 26**,** 1583-1594.

FEIFEL, S. C. & LISDAT, F. 2011. Silica nanoparticles for the layer-by-layer assembly of fully electro-active cytochrome c multilayers. *Journal of Nanobiotechnology,* 9**,** 59.

FERNÁNDEZ-GARCÍA, L., MARÍ-BUYÉ, N., BARIOS, J. A., MADURGA, R., ELICES, M., PÉREZ-RIGUEIRO, J., RAMOS, M., GUINEA, G. V. & GONZÁLEZ-NIETO, D. 2016. Safety and tolerability of silk fibroin hydrogels implanted into the mouse brain. *Acta Biomaterialia,* 45**,** 262-275.

FORNASARI, B. E., CARTA, G., GAMBAROTTA, G. & RAIMONDO, S. 2020. Natural-Based Biomaterials for Peripheral Nerve Injury Repair. *Frontiers in Bioengineering and Biotechnology,* 8.

FREDDI, G., GOTOH, Y., MORI, T., TSUTSUI, I. & TSUKADA, M. 1994. Chemical structure and physical properties of antheraea assama silk. *Journal of Applied Polymer Science,* 52**,** 775-781.

FROBEL, J., HEMEDA, H., LENZ, M., ABAGNALE, G., JOUSSEN, S., DENECKE, B., SARIĆ, T., ZENKE, M. & WAGNER, W. 2014. Epigenetic rejuvenation of mesenchymal stromal cells derived from induced pluripotent stem cells. *Stem Cell Reports,* 3**,** 414-22.

GATTAZZO, F., URCIUOLO, A. & BONALDO, P. 2014. Extracellular matrix: a dynamic microenvironment for stem cell niche. *Biochimica et biophysica acta,* 1840**,** 2506-2519.
GORENKOVA, N., OSAMA, I., SEIB, F. P. & CARSWELL, H. V. O. 2019. In Vivo Evaluation of Engineered Self-Assembling Silk Fibroin Hydrogels after Intracerebral Injection in a Rat Stroke Model. *ACS Biomaterials Science & Engineering,* 5**,** 859-869.
GREASLEY, S. L., PAGE, S. J., SIROVICA, S., CHEN, S., MARTIN, R. A., RIVEIRO, A., HANNA, J. V., PORTER, A. E. & JONES, J. R. 2016. Controlling particle size in the Stober process and incorporation of calcium. *J Colloid Interface Sci,* 469**,** 213-223.
GU, Y., YU, L., MOU, J., WU, D., ZHOU, P. & XU, M. 2020. Mechanical properties and application analysis of spider silk bionic material. *e-Polymers,* 20**,** 443-457.
GUIDETTI, G., D'AMONE, L., KIM, T., MATZEU, G., MOGAS-SOLDEVILA, L., NAPIER, B., OSTROVSKY-SNIDER, N., ROSHKO, J., RUGGERI, E. & OMENETTO, F. G. 2022. Silk materials at the convergence of science, sustainability, healthcare, and technology. *Applied Physics Reviews,* 9.
HĂBEANU, M., GHEORGHE, A. & MIHALCEA, T. 2023. Silkworm Bombyx mori—Sustainability and Economic Opportunity, Particularly for Romania. *Agriculture,* 13**,** 1209.
HAGHIGHATTALAB, M., KAJBAFZADEH, A., BAGHANI, M., GHAREHNAZIFAM, Z., JOBANI, B. M. & BANIASSADI, M. 2022. Silk Fibroin Hydrogel Reinforced With Magnetic Nanoparticles as an Intelligent Drug Delivery System for Sustained Drug Release. *Frontiers in Bioengineering and Biotechnology,* 10.
HAZRA, S., NANDI, S., NASKAR, D., GUHA, R., CHOWDHURY, S., PRADHAN, N., KUNDU, S. C. & KONAR, A. 2016. Non-mulberry Silk Fibroin Biomaterial for Corneal Regeneration. *Scientific Reports,* 6**,** 21840.
HOLLAND, C., NUMATA, K., RNJAK-KOVACINA, J. & SEIB, F. P. 2019. The Biomedical Use of Silk: Past, Present, Future. *Advanced Healthcare Materials,* 8**,** 1800465.
HUANG, W., LING, S., LI, C., OMENETTO, F. G. & KAPLAN, D. L. 2018. Silkworm silk-based materials and devices generated using bio-nanotechnology. *Chemical Society Reviews,* 47**,** 6486-6504.
HUANG, Y., BAILEY, K., WANG, S. & FENG, X. 2017. Silk fibroin films for potential applications in controlled release. *Reactive and Functional Polymers,* 116.
HUBBELL, J. A. 1995. Biomaterials in Tissue Engineering. *Bio/Technology,* 13**,** 565-576.
HYNES, K., MENICANIN, D., HAN, J., MARINO, V., MROZIK, K., GRONTHOS, S. & BARTOLD, P. M. 2013. Mesenchymal stem cells from iPS cells facilitate periodontal regeneration. *Journal of Dental Research,* 92**,** 833-9.
JAEGER, A. A., DAS, C. K., MORGAN, N. Y., PURSLEY, R. H., MCQUEEN, P. G., HALL, M. D., POHIDA, T. J. & GOTTESMAN, M. M. 2013.

Microfabricated polymeric vessel mimetics for 3-D cancer cell culture. *Biomaterials,* 34**,** 8301-8313.
JAFARI, S., DERAKHSHANKHAH, H., ALAEI, L., FATTAHI, A., VARNAMKHASTI, B. S. & SABOURY, A. A. 2019. Mesoporous silica nanoparticles for therapeutic/diagnostic applications. *Biomed Pharmacother,* 109**,** 1100-1111.
JARONIEC, M., JARONIEC, C. P., KRUK, M. & RYOO, R. 1999. Adsorption and thermogravimetric methods for monitoring surface and structural changes in ordered mesoporous silicas induced by their chemical modification. *Adsorption,* 5**,** 313-317.
JOHARI, N., MORONI, L. & SAMADIKUCHAKSARAEI, A. 2020. Tuning the conformation and mechanical properties of silk fibroin hydrogels. *European Polymer Journal,* 134**,** 109842.
KAIGHN, M., NARAYAN, K. S., OHNUKI, Y., LECHNER, J. F. & JONES, L. 1979. Establishment and characterization of a human prostatic carcinoma cell line (PC-3). *Investigative urology,* 17**,** 16-23.
KAPOOR, S. & KUNDU, S. C. 2016. Silk protein-based hydrogels: Promising advanced materials for biomedical applications. *Acta Biomaterialia,* 31**,** 17-32.
KAR, S., TALUKDAR, S., PAL, S., NAYAK, S., PARANJAPE, P. & KUNDU, S. C. 2013. Silk gland fibroin from indian muga silkworm Antheraea assama as potential biomaterial. *Tissue Engineering and Regenerative Medicine,* 10**,** 200-210.
KAZEMIMOSTAGHIM, M., RAJKHOWA, R., TSUZUKI, T. & WANG, X. 2013. Production of submicron silk particles by milling. *Powder technology,* 241**,** 230-235.
KHANNA, L., LAI, Y. & DASOG, M. 2018a. Systematic evaluation of inorganic salts as a heat sink for the magnesiothermic reduction of silica. *Canadian Journal of Chemistry,* 96**,** 965-968.
KHANNA, S., UTSAV, MARATHEY, P., CHALIYAWALA, H., RAJARAM, N., ROY, D., BANERJEE, R. & MUKHOPADHYAY, I. 2018b. Fabrication of long-ranged close-packed monolayer of silica nanospheres by spin coating. *Colloids and Surfaces A: Physicochemical and Engineering Aspects,* 553**,** 520-527.
KHARLAMPIEVA, E., KOZLOVSKAYA, V., WALLET, B., SHEVCHENKO, V. V., NAIK, R. R., VAIA, R., KAPLAN, D. L. & TSUKRUK, V. V. 2010. Co-cross-linking Silk Matrices with Silica Nanostructures for Robust Ultrathin Nanocomposites. *ACS Nano,* 4**,** 7053-7063.
KHOO, A. S., VALENTIN, T. M., LEGGETT, S. E., BHASKAR, D., BYE, E. M., BENMELECH, S., IP, B. C. & WONG, I. Y. 2019. Breast Cancer Cells Transition from Mesenchymal to Amoeboid Migration in Tunable Three-Dimensional Silk-Collagen Hydrogels. *ACS Biomater Sci Eng,* 5**,** 4341-4354.
KIM, H., KUMBAR, S. G. & NUKAVARAPU, S. P. 2021. Biomaterial-directed cell behavior for tissue engineering. *Curr Opin Biomed Eng,* 17.
KIM, J. H., KIM, H., CHOI, Y., LEE, D. S., KIM, J. & YI, G. R. 2017. Colloidal Mesoporous Silica Nanoparticles as Strong Adhesives for Hydrogels and Biological Tissues. *ACS Appl Mater Interfaces,* 9**,** 31469-31477.

KIM, W., CHOI, J. H., KIM, P., YOUN, J., SONG, J. E., MOTTA, A., MIGLIARESI, C., & KHANG, G. 2021. Preparation and evaluation of gellan gum hydrogel reinforced with silk fibers with enhanced mechanical and biological properties for cartilage tissue engineering. *Journal of Tissue Engineering and Regenerative Medicine,* 15**,** 936-947.

KIRILLOVA, A., YEAZEL, T. R., ASHEGHALI, D., PETERSEN, S. R., DORT, S., GALL, K. & BECKER, M. L. 2021. Fabrication of Biomedical Scaffolds Using Biodegradable Polymers. *Chem Rev,* 121**,** 11238-11304.

KIRITANI, S., KANEKO, J., ITO, D., MORITO, M., ISHIZAWA, T., AKAMATSU, N., TANAKA, M., IIDA, T., TANAKA, T., TANAKA, R., ASAKURA, T., ARITA, J. & HASEGAWA, K. 2020. Silk fibroin vascular graft: a promising tissue-engineered scaffold material for abdominal venous system replacement. *Scientific Reports,* 10**,** 21041.

KUMAR, V. B., TIWARI, O. S., FINKELSTEIN-ZUTA, G., RENCUS-LAZAR, S. & GAZIT, E. 2023. Design of Functional RGD Peptide-Based Biomaterials for Tissue Engineering. *Pharmaceutics* [Online], 15.

KUNDU, J., CHUNG, Y. I., KIM, Y. H., TAE, G. & KUNDU, S. C. 2010. Silk fibroin nanoparticles for cellular uptake and control release. *International Journal of Pharmaceutics,* 388**,** 242-50.

KUNDU, S. C., KUNDU, B., TALUKDAR, S., BANO, S., NAYAK, S., KUNDU, J., MANDAL, B. B., BHARDWAJ, N., BOTLAGUNTA, M., DASH, B. C., ACHARYA, C. & GHOSH, A. K. 2012. Nonmulberry silk biopolymers. *Biopolymers,* 97**,** 455-467.

LAMMEL, A. S., HU, X., PARK, S. H., KAPLAN, D. L. & SCHEIBEL, T. R. 2010. Controlling silk fibroin particle features for drug delivery. *Biomaterials,* 31**,** 4583-91.

LANGER, R. & VACANTI, J. P. 1993. Tissue engineering. *Science,* 260**,** 920-6.

LANZA, R., LANGER, R., VACANTI, J. P. & ATALA, A. 2020. *Principles of tissue engineering*, Academic press.

LARSON, B. L., YLOSTALO, J., LEE, R. H., GREGORY, C. & PROCKOP, D. J. 2010. Sox11 is expressed in early progenitor human multipotent stromal cells and decreases with extensive expansion of the cells. *Tissue Engineering Part A,* 16**,** 3385-94.

LAU, S., FEI, J., LIU, H., CHEN, W. & LIU, R. 2017. Multilayered pyramidal dissolving microneedle patches with flexible pedestals for improving effective drug delivery. *Journal of Controlled Release,* 265**,** 113-119.

LAUNER, P. J. & ARKLES, B. 2013. Infrared analysis of organosilicon compounds: spectra-structure correlations. *In:* LAUNER, P. J. & ARKLES, B. (eds.) *Silicon Compounds: Silanes & Silicones.* Morrisville, PA, USA: Gelest Inc.

LE SAUX, G., MAGENAU, A., GUNARATNAM, K., KILIAN, KRISTOPHER A., BÖCKING, T., GOODING, J. J. & GAUS, K. 2011. Spacing of Integrin Ligands Influences Signal Transduction in Endothelial Cells. *Biophysical Journal,* 101**,** 764-773.

LEE, E. J., KASPER, F. K. & MIKOS, A. G. 2014. Biomaterials for tissue engineering. *Annals of Biomedical Engineering* 42**,** 323-37.
LEE, H. R., KIM, S., SHIN, S., JEONG, S. Y., LEE, D. W., LIM, S. U., KANG, J. Y., SON, M. Y., LEE, C., YU, K. R., KIM, M. & OH, I. H. 2023. iPSC-Derived MSCs Are a Distinct Entity of MSCs with Higher Therapeutic Potential than Their Donor-Matched Parental MSCs. *International Journal of Molecular Sciences,* 24.
LEE, K. Y. & MOONEY, D. J. 2001. Hydrogels for Tissue Engineering. *Chemical Reviews,* 101**,** 1869-1880.
LEE, K. Y. & MOONEY, D. J. 2012. Alginate: properties and biomedical applications. *Prog Polym Sci,* 37**,** 106-126.
LÉRIDA-VISO, A., ESTEPA-FERNÁNDEZ, A., GARCÍA-FERNÁNDEZ, A., MARTÍ-CENTELLES, V. & MARTÍNEZ-MÁÑEZ, R. 2023. Biosafety of mesoporous silica nanoparticles; towards clinical translation. *Advanced Drug Delivery Reviews,* 201**,** 115049.
LI, J., ZHENG, L., ZENG, L., ZHANG, Y., JIANG, L. & SONG, J. 2016. RGD Peptide-Grafted Graphene Oxide as a New Biomimetic Nanointerface for Impedance-Monitoring Cell Behaviors. *Journal of Nanomaterials,* 2016**,** 2828512.
LI, Y., XIAO, Y. & LIU, C. 2017. The Horizon of Materiobiology: A Perspective on Material-Guided Cell Behaviors and Tissue Engineering. *Chem Rev,* 117**,** 4376-4421.
LIN, L., BOLUND, L. & LUO, Y. 2016. Towards Personalized Regenerative Cell Therapy: Mesenchymal Stem Cells Derived from Human Induced Pluripotent Stem Cells. *Current Stem Cell Research & Therapy* 11**,** 122-30.
LIU, J., DING, Z., LU, G., WANG, J., WANG, L. & LU, Q. 2019. Amorphous Silk Fibroin Nanofiber Hydrogels with Enhanced Mechanical Properties. *Macromolecular Bioscience,* 19**,** 1900326.
LIU, J., GE, X., LIU, L., XU, W. & SHAO, R. 2022. Challenges and opportunities of silk protein hydrogels in biomedical applications. *Materials Advances,* 3**,** 2291-2308.
LUJERDEAN, C., BACI, G. M., CUCU, A. A. & DEZMIREAN, D. S. 2022. The Contribution of Silk Fibroin in Biomedical Engineering. *Insects,* 13.
LYNCH, C. R., KONDIAH, P. P. D. & CHOONARA, Y. E. 2021. Advanced Strategies for Tissue Engineering in Regenerative Medicine: A Biofabrication and Biopolymer Perspective. *Molecules,* 26.
LYU, Y., LIU, Y., HE, H. & WANG, H. 2023. Application of Silk-Fibroin-Based Hydrogels in Tissue Engineering. *Gels,* 9.
MACHNOWSKI, W., GUTAROWSKA, B., PERKOWSKI, J. & WRZOSEK, H. 2013. Effects of gamma radiation on the mechanical properties of and susceptibility to biodegradation of natural fibers. *Textile Research Journal,* 83**,** 44-55.
MADDEN, P. W., KLYUBIN, I. & AHEARNE, M. J. 2020. Silk fibroin safety in the eye: a review that highlights a concern. *BMJ Open Ophthalmology,* 5**,** e000510.
MAITZ, M. F., SPERLING, C., WONGPINYOCHIT, T., HERKLOTZ, M., WERNER, C. & SEIB, F. P. 2017. Biocompatibility assessment of silk

nanoparticles: hemocompatibility and internalization by human blood cells. *Nanomedicine: Nanotechnology, Biology and Medicine,* 13**,** 2633-2642.
MAKATSORI, M., SCADDING, G. W., SKYPALA, I. & DURHAM, S. R. 2014. Silk contact anaphylaxis. *Contact Dermatitis,* 71**,** 314-315.
MALAY, A. D., SATO, R., YAZAWA, K., WATANABE, H., IFUKU, N., MASUNAGA, H., HIKIMA, T., GUAN, J., MANDAL, B. B., DAMRONGSAKKUL, S. & NUMATA, K. 2016. Relationships between physical properties and sequence in silkworm silks. *Sci Rep,* 6**,** 27573.
MAMAEVA, V., SAHLGREN, C. & LINDÉN, M. 2013. Mesoporous silica nanoparticles in medicine—Recent advances. *Advanced Drug Delivery Reviews,* 65**,** 689-702.
MANDAL, B. B., GRINBERG, A., SEOK GIL, E., PANILAITIS, B. & KAPLAN, D. L. 2012. High-strength silk protein scaffolds for bone repair. *Proceedings of the National Academy of Sciences,* 109**,** 7699-7704.
MANDAL, B. B. & KUNDU, S. C. 2008. Non-bioengineered silk gland fibroin protein: characterization and evaluation of matrices for potential tissue engineering applications. *Biotechnology and Bioengineering,* 100**,** 1237-50.
MATHUR, A. B. & GUPTA, V. 2010. Silk fibroin-derived nanoparticles for biomedical applications. *Nanomedicine,* 5**,** 807-820.
MATTHEW, S. A. L., REZWAN, R., KAEWCHUCHUEN, J., PERRIE, Y. & SEIB, F. P. 2022. Correction: Mixing and flow-induced nanoprecipitation for morphology control of silk fibroin self-assembly. *The Royal Society of Chemistry Advances,* 12**,** 25006-25009.
MATTHEW, S. A. L. & SEIB, F. P. 2023. Silk Bioconjugates: From Chemistry and Concept to Application. *ACS Biomater Sci Eng*.
MATTHEW, S. A. L., TOTTEN, J. D., PHUAGKHAOPONG, S., EGAN, G., WITTE, K., PERRIE, Y. & SEIB, F. P. 2020. Silk Nanoparticle Manufacture in Semi-Batch Format. *ACS Biomaterials Science & Engineering,* 6**,** 6748-6759.
MCKINNON, D. D., BROWN, T. E., KYBURZ, K. A., KIYOTAKE, E. & ANSETH, K. S. 2014. Design and characterization of a synthetically accessible, photodegradable hydrogel for user-directed formation of neural networks. *Biomacromolecules,* 15**,** 2808-2816.
MICKEY, D. D., STONE, K. R., WUNDERLI, H., MICKEY, G. H., VOLLMER, R. T. & PAULSON, D. F. 1977. Heterotransplantation of a human prostatic adenocarcinoma cell line in nude mice. *Cancer research,* 37**,** 4049-4058.
MIESZAWSKA, A. J., FOURLIGAS, N., GEORGAKOUDI, I., OUHIB, N. M., BELTON, D. J., PERRY, C. C. & KAPLAN, D. L. 2010. Osteoinductive silk-silica composite biomaterials for bone regeneration. *Biomaterials,* 31**,** 8902-10.
MITROPOULOS, A. N., BURPO, F. J., NGUYEN, C. K., NAGELLI, E. A., RYU, M. Y., WANG, J., SIMS, R. K., WORONOWICZ, K. & WICKISER, J. K. 2019. Noble Metal Composite Porous Silk Fibroin Aerogel Fibers. *Materials (Basel),* 12.

MÖLLER, K. & BEIN, T. 2017. Talented Mesoporous Silica Nanoparticles. *Chemistry of Materials,* 29**,** 371-388.
MÖLLER, K., KOBLER, J. & BEIN, T. 2007. Colloidal suspensions of mercapto-functionalized nanosized mesoporous silica. *Journal of Materials Chemistry,* 17**,** 624-631.
MOSLEM, M., EBERLE, I., WEBER, I., HENSCHLER, R. & CANTZ, T. 2015. Mesenchymal Stem/Stromal Cells Derived from Induced Pluripotent Stem Cells Support CD34(pos) Hematopoietic Stem Cell Propagation and Suppress Inflammatory Reaction. *Stem Cells International,* 2015**,** 843058.
NAM, S., HU, K. H., BUTTE, M. J. & CHAUDHURI, O. 2016. Strain-enhanced stress relaxation impacts nonlinear elasticity in collagen gels. *Proceedings of the National Academy of Sciences,* 113**,** 5492-7.
NAMEKAWA, T., IKEDA, K., HORIE-INOUE, K. & INOUE, S. 2019. Application of Prostate Cancer Models for Preclinical Study: Advantages and Limitations of Cell Lines, Patient-Derived Xenografts, and Three-Dimensional Culture of Patient-Derived Cells. *Cells,* 8**,** 74.
NARAYAN, R., NAYAK, U. Y., RAICHUR, A. M. & GARG, S. 2018. Mesoporous Silica Nanoparticles: A Comprehensive Review on Synthesis and Recent Advances. *Pharmaceutics,* 10.
NASKAR, D., SAPRU, S., GHOSH, A. K., REIS, R. L., DEY, T. & KUNDU, S. C. 2021. Nonmulberry silk proteins: multipurpose ingredient in bio-functional assembly. *Biomed Mater,* 16.
NUMATA, K. & KAPLAN, D. L. 2010. Silk-based delivery systems of bioactive molecules. *Advanced Drug Delivery Reviews,* 62**,** 1497-508.
NUMATA, K., YAMAZAKI, S. & NAGA, N. 2012. Biocompatible and Biodegradable Dual-Drug Release System Based on Silk Hydrogel Containing Silk Nanoparticles. *Biomacromolecules,* 13**,** 1383-1389.
ONDER, O. C., BATOOL, S. R. & NAZEER, M. A. 2022. Self-assembled silk fibroin hydrogels: from preparation to biomedical applications. *Materials Advances,* 3**,** 6920-6949.
OSAMA, I., GORENKOVA, N., MCKITTRICK, C. M., WONGPINYOCHIT, T., GOUDIE, A., SEIB, F. P. & CARSWELL, H. V. O. 2018. In vitro studies on space-conforming self-assembling silk hydrogels as a mesenchymal stem cell-support matrix suitable for minimally invasive brain application. *Scientific Reports,* 8**,** 13655.
OZAY, E. I., VIJAYARAGHAVAN, J., GONZALEZ-PEREZ, G., SHANTHALINGAM, S., SHERMAN, H. L., GARRIGAN, D. T., JR., CHANDIRAN, K., TORRES, J. A., OSBORNE, B. A., TEW, G. N., SLUKVIN, II, MACDONALD, R. A., KELLY, K. & MINTER, L. M. 2019. Cymerus™ iPSC-MSCs significantly prolong survival in a pre-clinical, humanized mouse model of Graft-vs-host disease. *Stem Cell Res,* 35**,** 101401.
PAL, S., KUNDU, J., TALUKDAR, S., THOMAS, T. & KUNDU, S. C. 2013. An emerging functional natural silk biomaterial from the only domesticated non-mulberry silkworm Samia ricini. *Macromolecular Bioscience,* 13**,** 1020-35.

PAREKH, N., C.K, B., KANE, K., PANICKER, A., NISAL, A., WANGIKAR, P. & AGAWANE, S. 2022. Superior processability of Antheraea mylitta silk with cryo-milling: Performance in bone tissue regeneration. *International Journal of Biological Macromolecules,* 213**,** 155-165.
PATIL, P. P., REAGAN, M. R. & BOHARA, R. A. 2020. Silk fibroin and silk-based biomaterial derivatives for ideal wound dressings. *International Journal of Biological Macromolecules,* 164**,** 4613-4627.
PATRA, C., TALUKDAR, S., NOVOYATLEVA, T., VELAGALA, S. R., MÜHLFELD, C., KUNDU, B., KUNDU, S. C. & ENGEL, F. B. 2012. Silk protein fibroin from Antheraea mylitta for cardiac tissue engineering. *Biomaterials,* 33**,** 2673-2680.
PEK, Y. S., WAN, A. C., SHEKARAN, A., ZHUO, L. & YING, J. Y. 2008. A thixotropic nanocomposite gel for three-dimensional cell culture. *Nat Nanotechnol,* 3**,** 671-5.
PHAM, D. T., SAELIM, N. & TIYABOONCHAI, W. 2019. Alpha mangostin loaded crosslinked silk fibroin-based nanoparticles for cancer chemotherapy. *Colloids and Surfaces B: Biointerfaces* 181**,** 705-713.
PHUAGKHAOPONG, S., MENDES, L., MÜLLER, K., WOBUS, M., BORNHÄUSER, M., CARSWELL, H. V. O., DUARTE, I. F. & SEIB, F. P. 2021. Silk Hydrogel Substrate Stress Relaxation Primes Mesenchymal Stem Cell Behavior in 2D. *ACS Applied Materials & Interfaces,* 13**,** 30420-30433.
PIERANTONI, L., RIBEIRO, V. P., COSTA, L., PINA, S., DA SILVA MORAIS, A., SILVA-CORREIA, J., KUNDU, S. C., MOTTA, A., REIS, R. L. & OLIVEIRA, J. M. 2021. Horseradish Peroxidase-Crosslinked Calcium-Containing Silk Fibroin Hydrogels as Artificial Matrices for Bone Cancer Research. *Macromolecular Bioscience,* 21**,** 2000425.
PIŞKIN, E. 1995. Biodegradable polymers as biomaterials. *Journal of Biomaterials Science, Polymer Edition,* 6**,** 775-95.
PRABHAKAR, C. 2014. Ericulture practices in India and prospects of ericulture in Cambodia. *International Journal of Wild Silkmoth and Silk,* 18**,** 23-31.
QI, Y., WANG, H., WEI, K., YANG, Y., ZHENG, R. Y., KIM, I. S. & ZHANG, K. Q. 2017. A Review of Structure Construction of Silk Fibroin Biomaterials from Single Structures to Multi-Level Structures. *Int J Mol Sci,* 18.
QIAN, K.-Y., SONG, Y., YAN, X., DONG, L., XUE, J., XU, Y., WANG, B., CAO, B., HOU, Q., PENG, W., HU, J., JIANG, K., CHEN, S., WANG, H. & LU, Y. 2020. Injectable ferrimagnetic silk fibroin hydrogel for magnetic hyperthermia ablation of deep tumor. *Biomaterials,* 259**,** 120299.
RAJKHOWA, R., WANG, L. & WANG, X. 2008. Ultra-fine silk powder preparation through rotary and ball milling. *Powder technology,* 185**,** 87-95.
REZAEI, F. S., SHARIFIANJAZI, F., ESMAEILKHANIAN, A. & SALEHI, E. 2021. Chitosan films and scaffolds for regenerative medicine applications: A review. *Carbohydr Polym,* 273**,** 118631.

RIBEIRO, M., FERRAZ, M. P., MONTEIRO, F. J., FERNANDES, M. H., BEPPU, M. M., MANTIONE, D. & SARDON, H. 2017. Antibacterial silk fibroin/nanohydroxyapatite hydrogels with silver and gold nanoparticles for bone regeneration. *Nanomedicine,* 13**,** 231-239.
RIBEIRO, V. P., SILVA-CORREIA, J., GONÇALVES, C., PINA, S., RADHOUANI, H., MONTONEN, T., HYTTINEN, J., ROY, A., OLIVEIRA, A. L., REIS, R. L. & OLIVEIRA, J. M. 2018. Rapidly responsive silk fibroin hydrogels as an artificial matrix for the programmed tumor cells death. *PLoS One,* 13**,** e0194441.
ROCKWOOD, D. N., PREDA, R. C., YÜCEL, T., WANG, X., LOVETT, M. L. & KAPLAN, D. L. 2011. Materials fabrication from Bombyx mori silk fibroin. *Nature Protocols,* 6**,** 1612-31.
ROOHANIESFAHANI, I., WANG, J., NO, Y. J., DE CANDIA, C., MIAO, X., LU, Z., SHI, J., KAPLAN, D. L., JIANG, X. & ZREIQAT, H. 2019. Modulatory effect of simultaneously released magnesium, strontium, and silicon ions on injectable silk hydrogels for bone regeneration. *Materials Science and Engineering: C,* 94**,** 976-987.
ROSE, S., PREVOTEAU, A., ELZIERE, P., HOURDET, D., MARCELLAN, A. & LEIBLER, L. 2014. Nanoparticle solutions as adhesives for gels and biological tissues. *Nature,* 505**,** 382-5.
SAETERSMOEN, M. L., HAMMER, Q., VALAMEHR, B., KAUFMAN, D. S. & MALMBERG, K.-J. 2019. Off-the-shelf cell therapy with induced pluripotent stem cell-derived natural killer cells. *Seminars in Immunopathology,* 41**,** 59-68.
SAKABE, H., ITO, H., MIYAMOTO, T., NOISHIKI, Y. & HA, W. S. 1989. In vivo blood compatibility of regenerated silk fibroin. *Sen'i Gakkaishi,* 45**,** 487-490.
SANCHEZ-RUBIO, A., JAYAWARNA, V., MAXWELL, E., DALBY, M. J. & SALMERON-SANCHEZ, M. 2023. Keeping It Organized: Multicompartment Constructs to Mimic Tissue Heterogeneity. *Adv Healthc Mater,* 12**,** e2202110.
SANTIN, M., MOTTA, A., FREDDI, G. & CANNAS, M. 1999. In vitro evaluation of the inflammatory potential of the silk fibroin. *Journal of Biomedical Materials Research,* 46**,** 382-9.
SANTORO, R., PERRUCCI, G. L., GOWRAN, A. & POMPILIO, G. 2019. Unchain My Heart: Integrins at the Basis of iPSC Cardiomyocyte Differentiation. *Stem Cells International,* 2019**,** 8203950.
SAPUDOM, J., KALBITZER, L., WU, X., MARTIN, S., KROY, K. & POMPE, T. 2019. Fibril bending stiffness of 3D collagen matrices instructs spreading and clustering of invasive and non-invasive breast cancer cells. *Biomaterials,* 193**,** 47-57.
SAXENA, U. & GOSWAMI, P. 2010. Silk Mat as Bio-matrix for the Immobilization of Cholesterol Oxidase. *Applied biochemistry and biotechnology,* 162**,** 1122-31.
SEIB, F. P. 2018. Reverse-engineered silk hydrogels for cell and drug delivery. *Therapeutic Delivery,* 9**,** 469-487.
SEIB, F. P. 2021. Emerging Silk Material Trends: Repurposing, Phase Separation and Solution-Based Designs. *Materials (Basel),* 14.

SEIB, F. P., MÜLLER, K., FRANKE, M., GRIMMER, M., BORNHÄUSER, M. & WERNER, C. 2009a. Engineered Extracellular Matrices Modulate the Expression Profile and Feeder Properties of Bone Marrow-Derived Human Multipotent Mesenchymal Stromal Cells. *Tissue Engineering Part A,* 15**,** 3161-3171.

SEIB, F. P., PREWITZ, M., WERNER, C. & BORNHÄUSER, M. 2009b. Matrix elasticity regulates the secretory profile of human bone marrow-derived multipotent mesenchymal stromal cells (MSCs). *Biochemical and Biophysical Research Communications,* 389**,** 663-667.

SEIB, F. P., PRITCHARD, M. & KAPLAN, L. 2013. Self-assembling doxorubicin silk hydrogels for the focal treatment of primary breast cancer. *Advanced Functional Materials,* 23**,** 58-65.

SELVAN, S. T. 2010. Silica-coated quantum dots and magnetic nanoparticles for bioimaging applications (Mini-Review). *Biointerphases,* 5**,** Fa110-5.

SELVARAJAN, V., OBUOBI, S. & EE, P. L. R. 2020. Silica Nanoparticles—A Versatile Tool for the Treatment of Bacterial Infections. *Frontiers in Chemistry,* 8.

SEMMLER, L., NAGHILOU, A., MILLESI, F., WOLF, S., MANN, A., STADLMAYR, S., MERO, S., PLOSZCZANSKI, L., GREUTTER, L., WOEHRER, A., PLACHETA-GYÖRI, E., VOLLRATH, F., WEISS, T. & RADTKE, C. 2023. Silk-in-Silk Nerve Guidance Conduits Enhance Regeneration in a Rat Sciatic Nerve Injury Model. *Advanced Healthcare Materials,* 12**,** e2203237.

SEN, S., GHOSH, S., DE, S., BASAK, P., MAURYE, P., JANA, N. K. & MANDAL, T. K. 2021. Immunomodulatory and antimicrobial non-mulberry Antheraea mylitta silk fibroin accelerates in vitro fibroblast repair and regeneration by protecting oxidative stress. *Royal Society of Chemistry Advances,* 11**,** 19265-19282.

SHACHAR, M., TSUR-GANG, O., DVIR, T., LEOR, J. & COHEN, S. 2011. The effect of immobilized RGD peptide in alginate scaffolds on cardiac tissue engineering. *Acta Biomaterialia,* 7**,** 152-162.

SHEN, D., YANG, J., LI, X., ZHOU, L., ZHANG, R., LI, W., CHEN, L., WANG, R., ZHANG, F. & ZHAO, D. 2014. Biphase Stratification Approach to Three-Dimensional Dendritic Biodegradable Mesoporous Silica Nanospheres. *Nano Letters,* 14**,** 923-932.

SHEYN, D., BEN-DAVID, S., SHAPIRO, G., DE MEL, S., BEZ, M., ORNELAS, L., SAHABIAN, A., SAREEN, D., DA, X., PELLED, G., TAWACKOLI, W., LIU, Z., GAZIT, D. & GAZIT, Z. 2016. Human Induced Pluripotent Stem Cells Differentiate Into Functional Mesenchymal Stem Cells and Repair Bone Defects. *Stem Cells Translational Medicine,* 5**,** 1447-1460.

SHI, L., WANG, F., ZHU, W., XU, Z., FUCHS, S., HILBORN, J., ZHU, L., MA, Q., WANG, Y., WENG, X. & OSSIPOV, D. A. 2017. Self-Healing Silk Fibroin-Based Hydrogel for Bone Regeneration: Dynamic Metal-Ligand Self-Assembly Approach. *Advanced Functional Materials,* 27**,** 1700591.

SILVA, S. S., OLIVEIRA, N. M., OLIVEIRA, M. B., DA COSTA, D. P. S., NASKAR, D., MANO, J. F., KUNDU, S. C. & REIS, R. L. 2016.

Fabrication and characterization of Eri silk fibers-based sponges for biomedical application. *Acta Biomater,* 32**,** 178-189.
SINGH, G. P., BAIG, M. M. & BAJPAYI, C. M. 2021. Chapter 8 - Recent trends in tasar silkworm Antheraea mylitta Drury disease management. *In:* GURTLER, V. & SUBRAHMANYAM, G. (eds.) *Methods in Microbiology.* Academic Press.
SONDERMEIJER, H. P., WITKOWSKI, P., SEKI, T., VAN DER LAARSE, A., ITESCU, S. & HARDY, M. A. 2017. RGDfK-Peptide Modified Alginate Scaffold for Cell Transplantation and Cardiac Neovascularization. *Tissue Engineering Part A,* 24**,** 740-751.
SOOD, D., CAIRNS, D. M., DABBI, J. M., RAMAKRISHNAN, C., DEISSEROTH, K., BLACK III, L. D., SANTANIELLO, S. & KAPLAN, D. L. 2019. Functional maturation of human neural stem cells in a 3D bioengineered brain model enriched with fetal brain-derived matrix. *Scientific reports,* 9**,** 17874.
STONE, K. R., MICKEY, D. D., WUNDERLI, H., MICKEY, G. H. & PAULSON, D. F. 1978. Isolation of a human prostate carcinoma cell line (DU 145). *International Journal of Cancer,* 21**,** 274-81.
SU, X., WEI, L., XU, Z., QIN, L., YANG, J., ZOU, Y., ZHAO, C., CHEN, L. & HU, N. 2023. Evaluation and Application of Silk Fibroin Based Biomaterials to Promote Cartilage Regeneration in Osteoarthritis Therapy. *Biomedicines,* 11**,** 2244.
SUBIA, B., CHANDRA, S., TALUKDAR, S. & KUNDU, S. C. 2014. Folate conjugated silk fibroin nanocarriers for targeted drug delivery. *Integrative Biology,* 6**,** 203-14.
SUN, W., GREGORY, D. A., TOMEH, M. A. & ZHAO, X. 2021. Silk Fibroin as a Functional Biomaterial for Tissue Engineering. *International Journal of Molecular Sciences,* 22.
SUO, A., XU, W., WANG, Y., SUN, T., JI, L. & QIAN, J. 2019. Dual-degradable and injectable hyaluronic acid hydrogel mimicking extracellular matrix for 3D culture of breast cancer MCF-7 cells. *Carbohydrate Polymers,* 211**,** 336-348.
SUTHERLAND, T. D., YOUNG, J. H., WEISMAN, S., HAYASHI, C. Y. & MERRITT, D. J. 2010. Insect Silk: One Name, Many Materials. *Annual Review of Entomology,* 55**,** 171-188.
TAE, J. H. & CHANG, I. H. 2023. Animal models of bone metastatic prostate cancer. *Investigative and Clinical Urology,* 64**,** 219-228.
TANAKA, T., UEMURA, A., TANAKA, R., TASEI, Y. & ASAKURA, T. 2018. Comparison of the knitted silk vascular grafts coated with fibroin sponges prepared using glycerin, poly(ethylene glycol diglycidyl ether) and poly(ethylene glycol) as porogens. *Journal of Biomaterials Applications,* 32**,** 1239-1252.
TANDON, S., KANDASUBRAMANIAN, B. & YAKOUT, S. 2020. Silk-Based Composite Scaffolds for Tissue Engineering Applications. *Industrial & Engineering Chemistry Research,* XXXX.
TANG, F., LI, L. & CHEN, D. 2012. Mesoporous Silica Nanoparticles: Synthesis, Biocompatibility and Drug Delivery. *Advanced Materials,* 24**,** 1504-1534.

TANG, X., DING, F., YANG, Y., HU, N., WU, H. & GU, X. 2009. Evaluation on in vitro biocompatibility of silk fibroin-based biomaterials with primarily cultured hippocampal neurons. *Journal of Biomedical Materials Research,* 91**,** 166-74.
TERAMOTO, H., AMANO, Y., IRAHA, F., KOJIMA, K., ITO, T. & SAKAMOTO, K. 2018. Genetic Code Expansion of the Silkworm Bombyx mori to Functionalize Silk Fiber. *ACS Synthetic Biology,* 7**,** 801-806.
THOMMES, M., KANEKO, K., NEIMARK, A. V., OLIVIER, J. P., RODRIGUEZ-REINOSO, F., ROUQUEROL, J. & SING, K. S. W. 2015. Physisorption of gases, with special reference to the evaluation of surface area and pore size distribution (IUPAC Technical Report). *Pure and Applied Chemistry,* 87**,** 1051-1069.
THU-HIEN, L., THANH-TRUC, N., TOI, V. V., KHON, H. C., BAO, B. C., NIEM, V. V. T., NGOC TUAN ANH, M., HAI, N. D., CHUONG, P. D. & HIEP, N. T. 2018. Evaluation of the Morphology and Biocompatibility of Natural Silk Fibers/Agar Blend Scaffolds for Tissue Regeneration. *International Journal of Polymer Science,* 2018**,** 5049728.
THURBER, A. E., OMENETTO, F. G. & KAPLAN, D. L. 2015. In vivo bioresponses to silk proteins. *Biomaterials,* 71**,** 145-157.
TIAN, Y., LIU, H., SHELDON, B. W., WEBSTER, T. J., YANG, S., YANG, H. & YANG, L. 2019. Surface energy-mediated fibronectin adsorption and osteoblast responses on nanostructured diamond. *Journal of Materials Science & Technology,* 35**,** 817-823.
TOMEH, M. A., HADIANAMREI, R. & ZHAO, X. 2019. Silk Fibroin as a Functional Biomaterial for Drug and Gene Delivery. *Pharmaceutics,* 11**,** 494.
TONSOMBOON, K., BUTCHER, A. L. & OYEN, M. L. 2017. Strong and tough nanofibrous hydrogel composites based on biomimetic principles. *Materials Science and Engineering: C,* 72**,** 220-227.
TOTTEN, J. D., WONGPINYOCHIT, T. & SEIB, F. P. 2017. Silk nanoparticles: proof of lysosomotropic anticancer drug delivery at single-cell resolution. *J Drug Target,* 25**,** 865-872.
TREWYN, B. G., SLOWING, I. I., GIRI, S., CHEN, H.-T. & LIN, V. S. Y. 2007. Synthesis and Functionalization of a Mesoporous Silica Nanoparticle Based on the Sol–Gel Process and Applications in Controlled Release. *Accounts of Chemical Research,* 40**,** 846-853.
ULLAH, M., KURODA, Y., BARTOSH, T. J., LIU, F., ZHAO, Q., GREGORY, C., REGER, R., XU, J., LEE, R. H. & PROCKOP, D. J. 2017. iPS-derived MSCs from an expandable bank to deliver a prodrug-converting enzyme that limits growth and metastases of human breast cancers. *Cell Death Discovery,* 3**,** 16064.
UMUHOZA, D., YANG, F., LONG, D., HAO, Z., DAI, J. & ZHAO, A. 2020. Strategies for Tuning the Biodegradation of Silk Fibroin-Based Materials for Tissue Engineering Applications. *ACS Biomaterials Science & Engineering,* 6**,** 1290-1310.
VISWANATHAN, S., KEATING, A., DEANS, R., HEMATTI, P., PROCKOP, D., STRONCEK, D. F., STACEY, G., WEISS, D. J., MASON, C. &

RAO, M. S. 2014. Soliciting strategies for developing cell-based reference materials to advance mesenchymal stromal cell research and clinical translation. *Stem Cells and Development,* 23**,** 1157-67.
VITTONI, C., GATTI, G., PAUL, G., MANGANO, E., BRANDANI, S., BISIO, C. & MARCHESE, L. 2019. Non-Porous versus Mesoporous Siliceous Materials for CO2 Capture. *ChemistryOpen,* 8**,** 719-727.
WAGNER, W., BORK, S., HORN, P., KRUNIC, D., WALENDA, T., DIEHLMANN, A., BENES, V., BLAKE, J., HUBER, F. X., ECKSTEIN, V., BOUKAMP, P. & HO, A. D. 2009. Aging and replicative senescence have related effects on human stem and progenitor cells. *PLoS One,* 4**,** e5846.
WAGNER, W., HORN, P., CASTOLDI, M., DIEHLMANN, A., BORK, S., SAFFRICH, R., BENES, V., BLAKE, J., PFISTER, S., ECKSTEIN, V. & HO, A. D. 2008. Replicative Senescence of Mesenchymal Stem Cells: A Continuous and Organized Process. *PLOS ONE,* 3**,** e2213.
WANG, F., GUO, C., YANG, Q., LI, C., ZHAO, P., XIA, Q. & KAPLAN, D. L. 2021. Protein composites from silkworm cocoons as versatile biomaterials. *Acta Biomaterialia,* 121**,** 180-192.
WANG, W., MEI, L., WANG, F., PEI, B. & LI, X. 2017. The Potential Matrix and Reinforcement Materials for the Preparation of the Scaffolds Reinforced by Fibers or Tubes for Tissue Repair. *In:* LI, X. (ed.) *Tissue Repair : Reinforced Scaffolds.* Singapore: Springer Singapore.
WANG, X., KLUGE, J. A., LEISK, G. G. & KAPLAN, D. L. 2008. Sonication-induced gelation of silk fibroin for cell encapsulation. *Biomaterials,* 29**,** 1054-1064.
WONGPINYOCHIT, T., JOHNSTON, B. F. & SEIB, F. P. 2016. Manufacture and Drug Delivery Applications of Silk Nanoparticles. *Journal of Visualized Experiments*.
WU, P., LIU, Q., WANG, Q., QIAN, H., YU, L., LIU, B. & LI, R. 2018. Novel silk fibroin nanoparticles incorporated silk fibroin hydrogel for inhibition of cancer stem cells and tumor growth. *Int J Nanomedicine,* 13**,** 5405-5418.
XIAO, W., TAN, Y., LI, J., GU, C., LI, H., LI, B. & LIAO, X. 2018. Fabrication and characterization of silk microfiber-reinforced methacrylated gelatin hydrogel with tunable properties. *Journal of Biomaterials Science, Polymer Edition,* 29**,** 2068-2082.
XIAO, Z., ZHAO, S., ZHANG, X., WEI, G. & SU, Z. 2022. Recent Advances in Peptide Engineering of PEG Hydrogels: Strategies, Functional Regulation, and Biomedical Applications. *Macromol. Mater. Eng.,* 307**,** 2200385.
XIN, Y., WANG, Y.-M., ZHANG, H., LI, J., WANG, W., WEI, Y.-J. & HU, S.-S. 2010. Aging Adversely Impacts Biological Properties of Human Bone Marrow-derived Mesenchymal Stem Cells: Implications for Tissue Engineering Heart Valve Construction. *Artificial Organs,* 34**,** 215-222.
XING, H., LEE, H., LUO, L. & KYRIAKIDES, T. R. 2020. Extracellular matrix-derived biomaterials in engineering cell function. *Biotechnology advances,* 42**,** 107421.

XU, W., WANG, T., WANG, Y., WU, X., CHEN, Y., SONG, D., CI, Z., CAO, Y., HUA, Y., ZHOU, G. & LIU, Y. 2022. An Injectable Platform of Engineered Cartilage Gel and Gelatin Methacrylate to Promote Cartilage Regeneration. *Front Bioeng Biotechnol,* 10**,** 884036.

YAMADA, H., IGARASHI, Y., TAKASU, Y., SAITO, H. & TSUBOUCHI, K. 2004. Identification of fibroin-derived peptides enhancing the proliferation of cultured human skin fibroblasts. *Biomaterials,* 25**,** 467-72.

YAN, Y., YAO, R., ZHAO, J., CHEN, K., DUAN, L., WANG, T., ZHANG, S., GUAN, J., ZHENG, Z., WANG, X., LIU, Z., LI, Y. & LI, G. 2022. Implantable nerve guidance conduits: Material combinations, multi-functional strategies and advanced engineering innovations. *Bioactive Materials* 11**,** 57-76.

YANG, H., FENG, R., FU, Q., XU, S., HAO, X., QIU, Y., FENG, T., ZENG, Z., CHEN, M. & ZHANG, S. 2019. Human induced pluripotent stem cell-derived mesenchymal stem cells promote healing via TNF-α-stimulated gene-6 in inflammatory bowel disease models. *Cell Death & Disease,* 10**,** 718.

YANG, L., YASEEN, M., ZHAO, X., COFFEY, P., PAN, F., WANG, Y., XU, H., WEBSTER, J. & LU, J. R. 2015. Gelatin modified ultrathin silk fibroin films for enhanced proliferation of cells. *Biomed Mater,* 10**,** 025003.

YANG, P., GAI, S. & LIN, J. 2012. Functionalized mesoporous silica materials for controlled drug delivery. *Chemical Society Reviews,* 41**,** 3679-3698.

YANG, Y., CHEN, X., DING, F., ZHANG, P., LIU, J. & GU, X. 2007. Biocompatibility evaluation of silk fibroin with peripheral nerve tissues and cells in vitro. *Biomaterials,* 28**,** 1643-52.

YIN, L., LI, X., WANG, R., ZENG, Y., ZENG, Z. & XIE, T. 2023. Recent Research Progress of RGD Peptide–Modified Nanodrug Delivery Systems in Tumor Therapy. *International Journal of Peptide Research and Therapeutics,* 29**,** 53.

YODMUANG, S., MCNAMARA, S. L., NOVER, A. B., MANDAL, B. B., AGARWAL, M., KELLY, T.-A. N., CHAO, P.-H. G., HUNG, C., KAPLAN, D. L. & VUNJAK-NOVAKOVIC, G. 2015. Silk microfiber-reinforced silk hydrogel composites for functional cartilage tissue repair. *Acta Biomaterialia,* 11**,** 27-36.

YOON, J.-K., KANG, M.-L., PARK, J. H., LEE, K.-M., SHIN, Y. M., LEE, J. W., KIM, H. O. & SUNG, H.-J. 2018. Direct Control of Stem Cell Behavior Using Biomaterials and Genetic Factors. *Stem Cells International,* 2018**,** 8642989.

YU, T., ZHANG, L., DOU, X., BAI, R., WANG, H., DENG, J., ZHANG, Y., SUN, Q., LI, Q., WANG, X. & HAN, B. 2022. Mechanically Robust Hydrogels Facilitating Bone Regeneration through Epigenetic Modulation. *Advanced Science,* 9**,** 2203734.

ZHANG, J., CHEN, M., LIAO, J., CHANG, C., LIU, Y., PADHIAR, A. A., ZHOU, Y. & ZHOU, G. 2021a. Induced Pluripotent Stem Cell-Derived Mesenchymal Stem Cells Hold Lower Heterogeneity and Great

Promise in Biological Research and Clinical Applications. *Frontiers in Cell and Developmental Biology,* 9**,** 716907.
ZHANG, L., ZHANG, W., HU, Y., FEI, Y., LIU, H., HUANG, Z., WANG, C., RUAN, D., HENG, B. C., CHEN, W. & SHEN, W. 2021b. Systematic Review of Silk Scaffolds in Musculoskeletal Tissue Engineering Applications in the Recent Decade. *ACS Biomater Sci Eng,* 7**,** 817-840.
ZHANG, Q., LI, M., HU, W., WANG, X. & HU, J. 2021c. Spidroin-Based Biomaterials in Tissue Engineering: General Approaches and Potential Stem Cell Therapies. *Stem Cells International,* 2021**,** 7141550.
ZHANG, Q., NGUYEN, P., BURRELL, J. C., ZENG, J., SHI, S., SHANTI, R. M., KULISCHAK, G., CULLEN, D. K. & LE, A. D. 2021d. Harnessing 3D collagen hydrogel-directed conversion of human GMSCs into SCP-like cells to generate functionalized nerve conduits. *npj Regenerative Medicine,* 6**,** 59.
ZHANG, Q., YAN, S. & LI, M. 2009. Silk Fibroin Based Porous Materials. *Materials,* 2**,** 2276-2295.
ZHANG, W., CAO, G., WU, F., WANG, Y., LIU, Z., HU, H. & XU, K. 2023. Global Burden of Prostate Cancer and Association with Socioeconomic Status, 1990–2019: A Systematic Analysis from the Global Burden of Disease Study. *Journal of Epidemiology and Global Health,* 13**,** 407-421.
ZHANG, W., WANG, X., WANG, S., ZHAO, J., XU, L., ZHU, C., ZENG, D., CHEN, J., ZHANG, Z., KAPLAN, D. L. & JIANG, X. 2011. The use of injectable sonication-induced silk hydrogel for VEGF165 and BMP-2 delivery for elevation of the maxillary sinus floor. *Biomaterials,* 32**,** 9415-9424.
ZHANG, Y.-Q., SHEN, W.-D., XIANG, R.-L., ZHUGE, L.-J., GAO, W.-J. & WANG, W.-B. 2007. Formation of silk fibroin nanoparticles in water-miscible organic solvent and their characterization. *Journal of Nanoparticle Research,* 9**,** 885-900.
ZHAO, X., HUEBSCH, N., MOONEY, D. J. & SUO, Z. 2010. Stress-relaxation behavior in gels with ionic and covalent crosslinks. *Journal of Applied Physics,* 107**,** 63509.
ZHAO, Z., LI, Y. & XIE, M. B. 2015. Silk fibroin-based nanoparticles for drug delivery. *International journal of molecular sciences,* 16**,** 4880-903.
ZHENG, H. & ZUO, B. 2021. Functional silk fibroin hydrogels: preparation, properties and applications. *Journal of Materials Chemistry B,* 9**,** 1238-1258.
ZHOU, B. & WANG, H. 2020. Structure and Functions of Cocoons Constructed by Eri Silkworm. *Polymers (Basel),* 12.
ZHOU, C. Z., CONFALONIERI, F., JACQUET, M., PERASSO, R., LI, Z. G. & JANIN, J. 2001. Silk fibroin: structural implications of a remarkable amino acid sequence. *Proteins,* 44**,** 119-22.